On the aeroelasticity of an extreme scale wind turbine

Using an FSI framework in NLR's inhouse code ENSOLV

R. Rietema

Delft University of Technology

TU Delft Delft University of Technology

Challenge the future

The work in this thesis was conducted and carried out in cooperation with,
Royal NLR.

On the aeroelasticity of an extreme scale wind turbine

Using an FSI framework in NLR's inhouse code ENSOLV

by

R. Rietema

For the degree of Master of Science in Aerospace Engineering at Delft University of Technology

December 11, 2019

DELFT UNIVERSITY OF TECHNOLOGY
DEPARTMENT OF
AERODYNAMICS, WIND ENERGY,FLIGHT PERFORMANCE AND PROPULSION
(AWEP)

THE UNDERSIGNED HEREBY CERTIFY THAT THEY HAVE READ AND RECOMMEND TO THE FACULTY OF AEROSPACE ENGINEERING (AE) FOR ACCEPTANCE A THESIS ENTITLED

On the aeroelasticity of
an extreme scale wind turbine

by

R. Rietema

in partial fulfillment of the requirements for the degree of

MASTER OF SCIENCE AEROSPACE ENGINEERING (AE)
AERODYNAMICS

at the Delft University of Technology

Dated: December 11, 2019

Thesis committee:

Chairman:
Dr. ir. B.W. van Oudheusden
Delft University of Technology
Aerodynamics

Dr. ir. A.H van Zuijlen
Delft University of Technology
Aerodynamics
Aerodynamics

Ir. J. van Muijden
Royal NLR
Aerospace Vehicles and Flight Performance

Ir. W.A. Timmer
Delft University of Technology
Wind energy

ABSTRACT

Recent decades, an ongoing trend has emerged in the upscaling of wind turbines in order to compete with traditional energy resources. For conventional wind turbines, aside from improving safety, the driving factors for new designs have always been increased efficiency and performance. This has led to novel wind turbine designs comprising thin-walled structures and light-weight composite materials that produce more power per unit. The current cost of wind energy is strongly dominated by operational and maintenance costs throughout the full lifetime of a wind turbine. Most wind turbines do not reach their design lifetime due to various reasons, from which fatigue failure is the most prominent one. The events responsible for gearbox or blade failure are caused by complex interactions between aerodynamics and structural responses that are inherently of unsteady nature. Aeroelasticity has become increasingly important for a safe and cost-effective design. Additionally, longer and lighter wind turbine blades undergo extremely large, low-strain deformations. A more accurate understanding of the aeroelastic behavior demands nonlinear analysis methods.

Most aeroelastic solvers in aerospace industry rely on linear structural models. This thesis work has modified the existing semi-nonlinear aeroelastic analysis method of the in-house developed CFD code at NLR by using `Nastran`'s nonlinear structural module. Both analysis methods were utilized to obtain a converged static aeroelastic solution for two different operational conditions of the design curve. Subsequently, mode shapes of the deformed state of the structure were determined, to be used in the flutter analysis.

A 108-meters theoretically designed blade, provided by the Dutch blade design company *We4Ce*, was analysed using both methods. The results of static aeroelastic analysis and flutter analysis were compared to assess the effect of structural nonlinearities on the aeroelastic behavior. It is concluded that linear analysis overestimates the structural deformations and that pre-stressing due to nonlinear deformations and follower-forces alter the dynamic properties of the wind turbine blade. For the test case considered, the inclusion of geometrical nonlinearities resulted in a change of behavior of various modes. Naturally-low damped modes were affected negatively, eventually leading to dynamically diverging behavior. This thesis has successfully provided the first steps in the implementation of a nonlinear aeroelastic analysis for extreme scale wind turbines, including the capability of performing stability analysis.

SUMMARY

Recent improvements in the energy yield and efficiency of wind turbines have led to increasingly large wind turbine designs. As continuous upscaling of wind turbines is expected, the demand for high-accuracy simulation methods that are capable of dealing with the accessory numerical challenges rises. Reynolds-Averaged Navier-Stokes (RANS)-based models are known to be superior in analysing the turbulent and unsteady flow around a wind turbine. But scale amplification also demands revision of the utilized structural models. Aeroelastic models that are required to predict certain failure mechanisms must cope with a complex set of structural and aerodynamic phenomena. It is believed that NS-based flow solvers combined with nonlinear structural solution methods are best capable of capturing the aeroelastic behavior of a wind turbine.
Aeroelasticity problems in aerospace industry are often based on linear FEM models to compute structural response. Likewise, the in-house developed CFD solver at NLR comprises linear structural modelling for both static and dynamic aeroelastic analysis. With the arrival of increasingly large blade designs, it is of paramount importance to investigate the effect of structural nonlinearities on the aeroelastic behavior of wind turbines. In this work, the existing aeroelastic framework is modified by the implementation of a nonlinear structural solver. Static aeroelastic solutions are obtained from the existing and modified aeroelastic solution method. Pre-stressed mode shapes are determined using both the linear stiffness matrix and the nonlinear stiffness matrix. The computed mode shapes are used to obtain a parametric description of the structure. Interpolation of the "linear" and "nonlinear" mode shapes onto the statically deformed aerodynamic grid allows performance of unsteady CFD simulations, while exciting the mode shapes in a sinusoidal motion. Flutter analysis is performed to assess the effect of an altered structural description on the stability results.
The methodology is performed on a 108-meters long, theoretically designed blade, provided by a Dutch blade design company called *We4Ce*. No validation data is available for this 15 MW-rated wind turbine, except for computational results from `Focus`. It was encountered that the acquired data depends on a variety of uncertainties, so it was chosen not to compare the results with these data. The structural and aerodynamic model were partly validated and the conclusions are based on a comparative study of both solution methods. The RANS-based CFD solver was validated two-fold. Firstly, two-dimensional computations were performed, after which the pressures were compared to wind tunnel experiments. Secondly, cross-sectional pressures from the full-rotor CFD simulation were compared to `Rfoil` and `Xfoil` results. For attached and two-dimensional flow, the CFD results were in reasonable agreement. No validation was feasible for the three-dimensional flow regions. Future DES or X-LES (i.e. NLR's variant of DES) computations can be performed to validate and verify the current method.
From the nonlinear aeroelastic approach, it is shown that the wind turbine blade is unstable for rated operating conditions. Local buckling effects occur at 90% span at the suction side of the blade. At mild operating conditions, linear structural modelling overestimates the static deformations comprising a difference of 0.27° of tip torsion. Although the differences are clearly visible, it does not influence the loads significantly yet. It can be expected that for heavier operational conditions, the effect amplifies, affecting the static aerodynamic loads. Furthermore, several mode shapes change due to the geometrically pre-stressed state of the blade. As a consequence, the aeroealastic behavior of various modes changes. The stability of naturally poor-damped modes can be affected negatively. On the contrary, it seems that the pure torsional mode disappears, which reduces the proclivity to flutter.

PREFACE

The work presented in this thesis could not have reached its current state without the help of some people in particular. First, I would like to thank Jaap van Muijden, who was my supervisor at NLR. Apart from giving me daily advice, you guided me though the entire process. Without your help, I was not able to finalize this project successfully. I would like to thank Sander van Zuijlen for the energy you gave me after each meeting we had. I always walked out the room with novel ideas and insights to implement the next steps in my research. Additionally, I would like to thank my colleagues from the AVFP department of NLR. They were always helpful and attentive. It was a pleasure to work in such a bright and social group. I want to express my gratitude to Mario verhagen in particular as he helped me extensively setting up the flutter analyses. I do not know how this research had ended without your help.
Last but not least, I would like to express my sincerest gratitude to my parents and girlfriend, who were there for me in good times and in bad times. They provided me the emotional support I sometimes needed to remain motivated and focused.

Amsterdam, The Netherlands
11-12-2019

Roald Rietema B.Sc.

Contents

List of Figures

List of Tables

NOMENCLATURE

Symbol	Description	Units
γ	rate-of-decay	[-]
λ	Buckling load factor	[-]
ϕ_i	Eigenvector of the i-th mode	[-]
ρ	Density	$[kg/m^3]$
ω	Circular frequency	$[rad/s]$
ω	Relaxation factor	[-]
Ω	Rotational velocity	$[RPM]$

Table 1: Greek symbols.

Symbol	Description	Units
Δt	Time step	$[s]$
a	Amplitude of excitation	[-]
c	Reference length	$[m]$
f	Frequency	$[Hz]$
g	structural damping	[-]
$\mathbf{g}$	Gravitational acceleration vector	$[m^2/s]$
$\mathbf{h}$	Displacement vector	$[m]$
$\mathbf{n}$	Normal vector	$[m]$
p	Complex roots	[-]
k	Reduced frequency	[-]
q_i	Generalized coordinate of i-th mode	[-]
q_∞	Dynamic pressure	$[Pa]$
t	time	$[s]$
$\mathbf{u_h}$	Modal displacements and velocities	[-]
x,y,z	Cartesian coordinates	$[m]$
$\mathbf{x}$	Displacement vector	$[m]$
$\dot{\mathbf{x}}$	Velocity vector	$[m/s]$
$\ddot{\mathbf{x}}$	Acceleration vector	$[m^2/s]$
A(p)	Unsteady aerodynamic force matrix	[-]
A^I	Imaginary part of aerodynamic force coefficient	[-]
A^R	Real part of aerodynamic force coefficient	[-]
B	Motion induced damping matrix	[-]
$\mathbf{B}$	Body force vector	$[N]$
C	Damping matrix	[-]
C_p	Pressure coefficient	[-]
$\mathbf{C_A}$	Aerodynamic force coefficient	[-]
C_{Q_i}	Generalized aerodynamic force in i-th mode	[-]
$\mathbf{F}$	External applied force vector	$[N]$
G	Interpolation matrix	[-]
K	Stiffness matrix	[-]
M	Mass matrix	[-]
R	Rotor radius	$[m]$
S	Reference area	$[m^2]$
T	Transformation matrix	[-]
$V^\star$	Speed index	[-]
U_∞	Inflow velocity	$[m/s]$

Table 2: Latin symbols.

Abbreviation	Full expression
ABL	Atmospheric Boundary Layer
AEP	Annual Energy Production
BEM	Blade-Element Momentum
CAD	Computer-Aided Design
CFD	Computational Fluid Dynamics
CoE	Cost of Energy
DDES	Delayed Detached-Eddy Simulation
DES	Detached-Eddy Simulation
DFT	Discrete Fourier Transorm
DOF	Degree-Of-Freedom
EARSM	Explicit-Algebraic Reynolds-Stress Model
EOM	Equations Of Motion
FFT	Fast Fourier Transform
FSI	Fluid-Structure Interaction
GAF	Generalized Aerodynamic Force
MAC	Modal Assurance Criterion
MW	MegaWatt
MSD	Model-Stress Depletion
RANS	Reynolds-Averaged Navier-Stokes
RBE	Rigid Bar Element
RMS	Root Mean Square
TFI	Transfinite Interpolation
SNL	Sandia National Laboratories
S-A	Spalart-Allmaras
SGS	Sub-Grid Scale
SPC	Single-Point Constraint
VSI	Volume-Spline Interpolation
X-LES	Extra-Large Eddy Simulation

Table 3: Abbreviations.

1

INTRODUCTION

1.1. MOTIVATION

In 2015 the Paris Agreement was adopted (UNFCCC, 2015). The aim of the Paris Agreement is to accelerate and intensify the actions to be undertaken to sustain a low carbon society in the future. The agreement aims on responding to climate change by keeping the global temperature rise below two degrees Celsius and to pursue efforts to keep it below 1.5 degrees Celsius. In contrast to electrical energy gained from fossil fuels, wind power is a promising renewable energy technology and could therefore play an important role in achieving the defined goals.

In order for wind turbines to compete with traditional energy resources, the Cost of Energy (CoE) must go down. For that reason, the design process of wind turbines is currently based on optimization of efficiency and power performance, leading to a continuous increase in overall size and rotor diameter. As a result, wind turbine designs shifted towards thin-walled, composite structures to keep their weight within limits. Consequently, aeroelastic effects can become more dominant in the dynamic behavior of wind turbines, which could lead to detrimental instabilities (Hansen et al., 2006). (Lobitz, 2004) even stated that the design process of wind turbines will be stability-driven in the future.

An aeroelastic model combines an aerodynamic model that determines aerodynamic loads and a structural model that calculates the dynamic response of the structure. The currently used aeroelastic models in industrial practices most commonly employ BEM models for the aerodynamics and use a series of one-dimensional beam elements to model the blade's structure. However, as explained by (Bazilevs et al., 2011a), an aeroelastic framework must contain models that can cope with time-dependent flow phenomena, like gusts and other unsteady flow effects. Furthermore, the models must accurately predict the deformations and dynamic response of the blade taking into account complex geometries and material compostions. This motivated *Bazilevs et al.* to propose a so-called "paradigm shift" in wind turbine aeroelastic modelling by developing a complex Fluid-Structure Interaction (FSI) modelling framework using Navier-Stokes (NS) equations. This "paradigm shift" has led to publication of more studies on aeroelastic modelling of extreme scale wind turbines, using CFD-based methods (Corson et al., 2012; Yu and Kwon, 2013; Guo et al., 2013). However, most studies were based on wind turbines with blades smaller than 100 meters. Hence, the knowledge on the performance of existing models in aeroelastic analysis of extreme scale wind turbines remains limited.

(van Garrel et al., 2018) pointed out that the challenges aerospace industry has faced in the past correspond to the challenges the wind turbine industry encounters nowadays. Therefore, they propose a more extensive collaboration between these sectors regarding research topics of mutual interest, such as aeroelasticity. As such, a collaboration was set up with We4Ce, a Dutch company that specializes in the design process of wind turbines. We4Ce has provided the design of a 108-meter long wind turbine blade to be used in this study.

An earlier study performed by a former graduate student has already validated the in-house CFD code of NLR for the MEXICO wind turbine experiment (Ten Pas, 2016), which comprised of aerodynamic analysis of a rigid wind turbine model. The results were very promising. Applying the multi-block, compressible flow solver to

the MEXICO test case has shown that high-accuracy predictions can be obtained for realistic and practical wind turbine flow problems.
For aerospace aeroelasticity, generally linear finite element models are used to describe the structure (van Garrel et al., 2018). Nonlinear effects between loads and deformations are often ignored. However, as wind turbine blades increase in size resulting in larger structural deformations, these effects may not be disregarded.

It is therefore of paramount importance to carefully investigate the influence of structural nonlinearities on the aeroelastic behavior of extreme scale wind turbines. This thesis studies these effects in order to obtain a better understanding of the working capacity of existing aerospace aeroelastic solvers on wind turbine related problems.

1.2. RESEARCH OBJECTIVE

The main aim of this research is to develop a validated aeroelastic approach for static and dynamic aeroelastic analysis of extreme scale wind turbines using the in-house CFD code `ENSOLV`. Furthermore, this project aims to improve and contribute to the understanding of the aerodynamic and structural phenomena that are essential in the aeroelastic behavior of these machines.
From the initial research proposal, it became clear that a number of numerical challenges had to be overcome in order to develop an aeroelastic simulation framework that could simulate a full wind turbine. Due to the limited scope of this study, this research focuses on the aeroelastic modelling of a wind turbine rotor subject to non-turbulent, uniform inflow at normal operating conditions. The effect of structural nonlinearities on the static and dynamic aeroelastic behavior of the blade was investigated.
The objective of this research was realized utilizing the existing aeroelastic framework of `ENSOLV` and integrating a nonlinear structural solver into the existing framework. A comparative study of both simulation methodologies can provide more knowledge about the requirement of nonlinear solving strategies in the structural modelling of wind turbines. Subsequently, future implementation of this method can be useful to verify aeroelastic results of lower-fidelity methods commonly used in industrial practices.

1.3. RESEARCH QUESTIONS

Following the motivation and research objective, the central research question can be formulated as follows:

What is the influence of structural nonlinearities on the stability assessment of an extreme scale wind turbine?

Several sub questions are formulated in order to guide the process to answer the main question:

- What are the key structural nonlinearities in the aeroelastic behavior of an extreme scale wind turbine blade?
- What effect do structural nonlinearities have on the static aeroelastic equilibrium of an extreme scale wind turbine blade?
- Compared to semi-linear aeroelastic analysis, to what extent does the inclusion of structural nonlinearities alter the dynamic properties of the blade? And what effect does this have on the aeroelastic response?

1.4. THESIS OUTLINE

An introduction is given to the aeroelasticity problem that has to be modelled in the literature review given inchapter 2. Afterwards, tye current state-of-the-art in aeroelastic modelling of wind turbines is discussed. NS-based aeroelastic modelling has not been extensively applied to extreme scale wind turbines. Therefore, the literature review gives an overview of existing models and discusses their strengths and weaknesses to obtain a better understanding for applying such models correctly. The exact methodology of this work is presented in chapter 3. This chapter is decomposed in two parts that comprise all simulations: static aeroelastic analysis and flutter analysis. Chapter 4 discusses each sub model and partly validates the RANS-based CFD solver by comparing computational results with experimental data and alternative flow solver results. Once the aeroelastic framework is explained, the CFD simulations are performed and the results are discussed in chapter 5. In chapter 6, the conclusions, limitations and recommendations for future work are elaborately discussed.

2

LITERATURE REVIEW

The aim of this chapter is to give an overview of research and recent developments in the field of wind turbine aeroelasticity. Furthermore, some background information is given on the difference in modelling strategies that are used in the scientific community.

2.1. AEROELASTICITY

In this section, first a brief introduction into the basics of aeroelasticity is given. Subsequently, the accent shifts more specifically towards wind turbine aeroelasticity.

2.1.1. INTRODUCTION TO AEROELASTICITY

Aeroelastic phenomena arise when structural deformations induce a change in aerodynamic forces, after which the additional aerodynamic forces may produce additional deformations. These reciprocal interactions generally tend to become smaller and smaller until a certain equilibrium is reached, however they can also have a magnifying effect on each other leading to divergence and eventually material failure (Bisplinghoff et al., 1996). Aeroelasticity is based on the interaction of different properties: inertial, aerodynamic and elastic properties of the system; forming a triangle of disciplines (Clark et al., 2012), see figure 2.1. Aeroelastic effects can lead to instabilities, which might lead to structural damage and eventually failure of the structure.

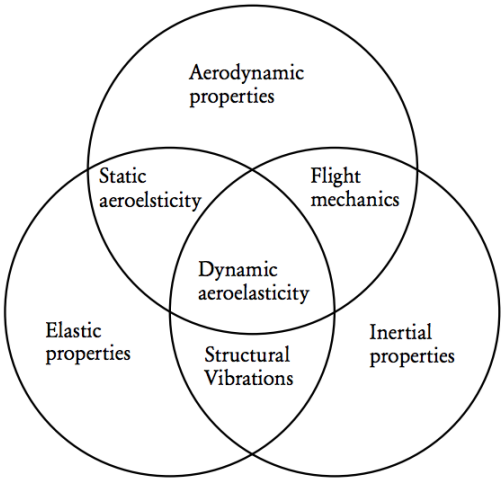

Figure 2.1: Subdivision of aeroelastic disciplines (Clark et al., 2012)

An instability has two important characteristics: it is a growing motion that is self-excited and grows exponentially (Bir and Jonkman, 2007). A self-excited motion implies that there is no associated external force feeding the instability. The self-excitation occurs by the motion of the blade and the thereby changing flow conditions. This can be better understood when a single degree-of-freedom (DOF) system is considered:

$$M\ddot{\mathbf{x}} + C\dot{\mathbf{x}} + K\mathbf{x} = \mathbf{F}(t) \tag{2.1}$$

Here M is the mass matrix, C the damping matrix, K the stiffness matrix, $\mathbf{F}(t)$ the external force and $\mathbf{x}$ contains the displacements in the number of DOF's.
It must be noted that in this example the mass, damping and stiffness matrices are constant. In order to satisfy the conditions for an instability, the motion must be self-excited, thus the forces in this system should at least depend on its motion. For simplicity, the forces on the aeroelastic system can be defined as $\mathbf{F}(t) = B\dot{\mathbf{x}}$, since

dependence of location and acceleration does not influence the system's damping and therefore stability. The equation of motion (EOM) become:

$$M\ddot{\mathbf{x}} + (C - B)\dot{\mathbf{x}} + K\mathbf{x} = 0 \tag{2.2}$$

If the effective damping, $(C - B)$, becomes negative, the system's response grows exponentially. In reality, the above simplified mathematical expression is not credible, since most instabilities involve multiple DOF's and the interaction between motion and forces is nonlinear and unsteady.

Aeroelastic instabilities can be categorized in three types on basis of the source of self-excitation:

1. Mode-coupled instabilities: Energy transfer between different modes takes place.
2. Nonlinear instabilities: Nonlinear phenomena (e.g. dynamic stall) cause the instability.
3. Parametric instabilities: This kind of instability occurs when different excitations couple and amplify (e.g. coupling of a control system with vibration of the tower).

There are a lot of different aeroelastic effects, which are extensively described by (Bisplinghoff et al., 1996) and many others. However, these will not be discussed here, since the focus lies on wind turbine aeroelasticity. The instabilities with the highest likelihood will be discussed in the remainer of this section.

2.1.2. WIND TURBINE AEROELASTICITY

The past decades, research in wind turbine aeroelasticity has increased remarkably. Multiple shape optimization studies are conducted to optimize wind turbines in terms of cost of energy (CoE) in order to be more competitive with other energy resources (A. Chehouri and Perron, 2015; Kenway and Martins, 2008). This has led to the usage of composite materials that provide elastic couplings in the blade. The rise of larger and smarter (e.g. elastic coupling) blade designs may increase the blade's proclivity to flutter. In 2004, (Lobitz, 2004) already reported that the flutter speed of MW-rated wind turbines has decreased to twice the operational speed. This emphasizes the need for good aeroelasticity models in order to assess the probability of instabilities early on in the design stage. Since then, an increasing amount of effort has put in the development of good wind turbine aeroelasticity models.

RELEVANT INSTABILITIES

Section 2.1.1 has already given a brief introduction about aeroelasticity and types of aeroelastic instabilities. However, not each instability is even likely to occur for wind turbines. (Holierhoek, 2013) has written an article about possible aeroelastic instabilities for wind turbines, from which the most relevant are discussed here.

Divergence in the torsional degree of freedom can only occur if the torsional stiffness is so low that the centrifugal twisting moment, induced by the flapping motion of the blade, is sufficient to drive the wind turbine blade into stall. However, this is only the case if there is a pitch-link failure, whereby the torsional stiffness completely disappears (Holierhoek, 2013). As pointed out by (Pavel and Schoones, 1999), this instability has not occurred yet for wind turbines. However, it should be checked, especially for large wind turbines.

Throughout years of research, it turned out that the edgewise instability is a critical instability, especially for stall-regulated wind turbines. Edgewise blade modes are aerodynamically very low damped (Hansen et al., 2006). The working principle of the edgewise instability is very simple. Figure 2.2 shows the aerodynamic damping coefficient as function of the vibration direction. The rotating airfoil section is harmonically translated along the axis x_B, relative to the rotor plane, x_R, with angle θ_{RB}. The graphs show that for vibrational directions close to 0∘, which corresponds to edgewise vibrations, the aerodynamic damping coefficient is negative, independently of the inflow speed. In contrast to edgewise vibrations, the aerodynamic damping coefficient for flapwise motion depends on the inflow speed.

(Hansen et al., 2006) also clarifies that the edgewise instability often couples with tower modes increasing its response with some orders of magnitude. This conclusion is drawn after comparing the power spectral densities of a turbine with a flexible tower and a stiff tower. It turned out that the spectral densities of the tower lateral bending moment for the case with flexible tower show a distinct peak at the frequency of the

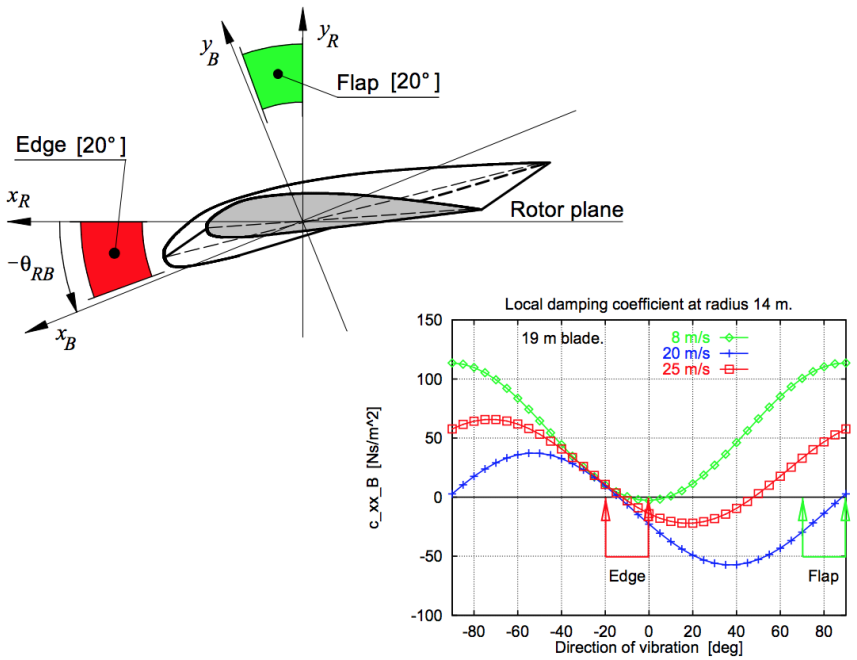

Figure 2.2: The aerodynamic damping coefficient for a rotating airfoil as function of the vibration direction θ_{RB} for three different inflow speeds (Madsen and Rasmussen, 1998)

first edgewise blade bending mode. Hence, in order to capture the full effects on the edgewise vibration, the tower must be included in the model.
The last instability that will be discussed is flutter. This instability is a well-known instability for aircraft. It is expected that the flutter speed will continuously decrease as the size of wind turbines grow (Lobitz, 2004). The flutter instability is a classical example of a mode-coupled instability involving two DOF's of the blade, namely flapwise bending and torsion. The flutter speed decreases as the frequency of these modes approach each other. Flutter is an extremely damaging instability as it develops itself within seconds.

A distinction must be made between two types of flutter: stall flutter and classical flutter (Hansen, 2007). Stall flutter involves only the first torsional mode. This instability only occurs for wind turbines operating near stall as the name says.

Assume a wind turbine already operating in stall that is exposed to a gust. The sudden increase in angle of attack decreases the aerodynamic loading, which in turn decreases the angle of attack again. For a smaller angle of attach the force will rise, which may result in an unstable cycle. Vibrations induced by stall can also occur in different directions. There are three parameters that dominate the risk of stall-induced vibrations: (Hansen, 2007):

- Airfoil characteristics: A sudden and sharp change in lift slope increases the probability of stall-induced vibrations.
- Direction of vibration: Figure 2.2 already showed that certain vibration directions are less damped.
- Structural damping: A negative aerodynamic damping could be compensated by structural damping. However, the use of advanced carbon-epoxy composite systems has reduced the structural damping of blades (Chortis et al., 2007).

Most commercial wind turbines have shifted to active-pitch-regulated systems preventing the wind turbine of operating in stall. The risk of stall-induced vibrations is therefore reduced significantly. However, classical flutter still forms a risk for long and slender wind turbine blades if the eigenfrequencies of torsional modes and bending modes approach each other. In contrast to stall-induced vibrations, stall flutter can not be

damped by structural damping as it is a more severe instability. Classical flutter may occur if the following four criteria are satisfied:

- Attached flow: An increase in angle of attack must induce a rise in lift.
- High tip speeds: High flow velocities ensure sufficient energy in the aerodynamic forces.
- Low stiffness: Both the torsional mode and flapwise bending mode must have a low frequency in order to couple.
- Aft position of the center of gravity: To ensure the right phasing between torsion and bending, the center of gravity must be aft of the aerodynamic center, especially towards the outboard region of the blade.

There are more parameters that influence the flutter limit, but the aforementioned criteria are fundamental. Although, rotor speeds are limited due to noise considerations, it can be concluded that classical flutter is most likely to occur for large flexible blades operating at rated conditions or in overspeed.

2.2. HIGH-FIDELITY AEROELASTIC CODES

As mentioned in the introduction, common wind turbine modelling approaches used by industry do not have the capability to solve highly three-dimensional, nonlinear and unsteady flows. For the aeroelastic analysis of wind turbines, methods are needed that are able to handle complex time-dependent flow phenomena, such as gusts and flow separation. This has led to the research of FSI models including higher-fidelity aerodynamic models, from which some are discussed in this section.

At full scale, coupled FSI simulations are essential for accurate modelling of wind turbines (Bazilevs et al., 2011b). The motion and deformation of wind turbine blades depends on the total air flow over the blade, while the air flow depends on the shape, position and movement of the wind turbine blades. (Bazilevs et al., 2011b) were the first to attempt a coupled FSI simulation of a full-scale wind turbine rotor for aeroelastic analysis. They used a low-order finite element Arbitrary Lagrangian-Eulerian Variational Multi-scale technique for the aerodynamics, which is a moving domain extension of the residual-based Variational Multi-Scale formulation of the NS equations. This aerodynamic solver is coupled to a structure solver that discretizes the wind turbine blades as thin composite shells using a Non-Uniform Rational B-Splines(NURBS)-based Isogeometric Analysis. The thin composite shells should approximate the surface of the wind turbine blade closely. The structural and aerodynamic model were tightly coupled and the aeroelastic equations are solved using a block-iterative process.

In order to validate their computational framework, they simulated the NREL 5-MW reference wind turbine rotor. The NREL 5-MW turbine is developed to support concept studies aiming to assess off shore wind technology. The results showed a good prediction of the torque and the blade tip deflection compared to the values from the technical report from NREL (Jonkman et al., 2009). In this study, periodic boundary conditions were used, so only one blade and one-third of the hub had to be modelled to reduce the simulation space. Therefore, this method is incapable of incorporating unsteady effects, like wind shear and tower-rotor interaction. In the future, they intend to include the tower in the simulation, because the presence of the tower will change the aerodynamics and consequently the blade loading.

In 2012, (Hsu and Bazilevs, 2012) conducted a proceeding study using the same models, but now simulated the full NREL 5-MW wind turbine. Because of the presence of the tower, the environment of the rotor is not periodic any more causing the periodic boundary conditions to be not valid anymore. In order to solve this, the complete geometry of the wind turbine had to be included in the aerodynamic mesh. Coupling between the stationary and rotating domains was performed using a sliding interface that imposed the kinematic and traction continuity at the rotating and stationary sub domains. The results of this study show that the presence of the tower has a great influence on the aerodynamic loads of the rotor. Due to the blades passing the tower, a significant drop in the aerodynamic torque is encountered by the blades. The interference between the tower and rotor creates a cyclic loading, which causes a variability in the deformation and loading of the individual blades. The non-symmetrical deformations of the blades also induced eccentric loads on the hub.

(Guo et al., 2013) proposed a CFD-CSD method that can be used for the aeroelastic analysis of large wind turbines. The unsteady NS equations are solved using a dual time-stepping approach after the space is discretized using a finite volume scheme. Low-Mach number preconditioning is applied to improve the accuracy and speeds up the numerical convergence. The preconditioning is done by multiplying the time derivative with a preconditioning matrix. The fluid model they opted for was the Spalart-Allmaras (S-A) based Detached-Eddy Simulation (DES) model, which was employed to predict separated flows with high accuracy. For the structural model they used a 1D beam model that is solved with a predictor-corrector scheme. The system is tightly coupled, which means that sub iterations within each time step are used to ensure convergence. Only the hub-blades configuration of the NH1500 wind turbine is simulated. The results were verified with a wake-vortex simulation of the same configuration. The results show good agreement with the wake-vortex model. Future work should consider interaction with the tower and different wind conditions.

Sandia National Laboratories (SNL) Wind Energy Technology Department has performed several studies to create and evaluate large wind turbine blades for horizontal axis wind turbines to promote designs that are more efficient in aerodynamic, structural and economical aspects (Griffith and Ashwill, 2011). The aim is to deliver a 100-m reference blade design for a rated 13.2-MW wind turbine. The same researchers that developed this blade conducted an aeroelastic analysis of their own blade (Corson et al., 2012). The commercially available flow solver called `AcuSolve` was used to solve the aerodynamics. For the steady-state simulation, Reynolds-averaged Navier-Stokes (RANS) simulations with a S-A turbulence model were used and for the transient simulations a Delayed-Detached Eddy Simulation (DDES) was applied. The structural dynamics of the blade were modelled in `RADIOSS` (a finite element package), where the blade is discretized using shell elements. Only a single blade is considered in the steady-state simulations, whereby the deformation of the blade is modelled by a superposition of a number of independent vibration modes. The results were compared with results from `WT_perf`(Platt and Buhl, 2012) and `FAST` (Jonkman and Buhl, 2005) simulations. The steady-state results were in reasonable agreement with the latter codes. However, the thrust, bending moment and tip displacement showed deviations in comparison to the `FAST` results. Apparently, other researchers (Resor et al., 2010) also documented that the `FAST` code delivered over-estimated values for these quantities. An explanation is that the induction factor is largely underestimated, which results in higher angles of attack and thus higher aerodynamic loads and thrust.
According to initial calculations performed by SNL using the Lobitz approach, the blade design has little margins to flutter. The analysis resulted in a predicted flutter speed of 1.0-1.1 times the maximum rated rotor speed. The CFD-based technique was also used to attempt to predict the flutter speed. But unfortunately, the method proved to be unsuitable to find the flutter speed.

(Yu and Kwon, 2013) developed a CFD-CSD aeroelastic code in a slightly different fashion. The flow is modelled by the incompressible RANS equations. The flow domain is discretized using a vertex-centred finite-volume method on an unstructured mesh. To allow the turbulent eddy viscosity to be determined, the κ-ω SST model was used. The simulations performed covered calculations for both the rotor-alone configuration and the full wind turbine. The elastic deformation of the wind turbine blades was computed using a FEM-based CSD solver adopting a nonlinear coupled flap-lag-torsion beam theory model. The data exchange between the structure and flow solver is based on a loosely-coupled methodology. A steady and dynamic aeroelastic analysis were performed on the 5-MW reference wind turbine and compared with the design values, which were obtained using a `FAST Aerodyn` simulation. The torsional deformation remained unverified, as it showed significant deviations from the design values. This could be due to the inability of the Blade-Element Momentum (BEM)-based model (`FAST Aerodyn`) to predict the aerodynamic pitching moment accurately. The research group continued their study by performing an unsteady analysis including gravitational forces, interference with the tower and rotor shaft tilt. They concluded that the coupled CFD-CSD method can predict the elastic deformations and unsteady aerodynamic loads with good accuracy.

(Carrión et al., 2014) have developed a tightly-coupled CFD-CSD code and applied it to two wind turbine models for an aeroelastic analysis. As fluid model, the compressible Helicopter Multi-Block RANS solver was used. To determine the structural deformations, the mode shapes of a finite element cantilever beam were used. The mesh adaptation is performed in three steps. The blade surface is deformed using the Constant Volume Tetrahedron method. The vertices of the multi-block grid are displaced using spring analogy, after which the grid is generated using transfinite interpolation. The coupling between the moving rotor and stationary tower was executed by a sliding plane. The simulations were performed on the NREL Phase IV and

MEXICO wind turbine, which both are small-scaled wind turbine models with a rotor diameter of 4.5 and 10 meter respectively. It must be mentioned that due to the small scale of these models, the aeroelastic effects encountered are not of the scale of full-scale wind turbines. Both static and dynamic simulations were performed, whereby two types of aeroelastic methods were implemented into the flow solver:

- A decoupled method suitable for steady-state problems, where the aerodynamic loads from the CFD solver were implemented into the CSD solver.
- A dynamic tightly coupled method for more complex unsteady problems; structure solver and flow solver are solved simultaneously. The blade deformation is a combination of the eigenvectors of the blade and is updated every time step. To obtain the eigenmode shapes and eigenfrequencies the `NASTRAN` solver is employed.

The results showed that the aeroelastic effects were larger for the more flexible blade (NREL Phase IV), which confirms the importance of aeroelastic analysis for extreme scale wind turbines with flexible blades.

The use of high-fidelity FSI methods for the aeroelastic modelling of large wind turbines has been introduced by (Hsu and Bazilevs, 2012) in 2011. Regarding the previously conducted aeroelastic studies, it is hard to draw solid conclusions about what methodology performs best in aeroelastic analysis of extreme scale wind turbines. Nonetheless some important information can be obtained from those studies. The multi-physics modelling strategy consists of multiple sub models, each taking care of its part within the overall physics. The FSI models usually consist of the following sub models: fluid model, structure model, mesh-deformation algorithm, time-coupling model and space-discretization model. For each sub model, different techniques are available that each have their advantages and disadvantages.
Some commonalities can be deduced from the discussed methodologies. It appears that (U)RANS and DES are the most commonly used fluid models. Besides, most frameworks use a strongly-coupled FSI approach to ensure a certain level of convergence at the end of each time step.
In the following sections, the choice per sub model will be discussed elaborately.

2.3. FLUID MODELS

2.3.1. HISTORICAL BACKGROUND

Through the years many fluid models have been developed, from which only a few are actually used in industrial codes. (Hansen et al., 2006) composed a comprehensive review of wind turbine aeroelasticity, including different type of aerodynamic models.

The actuator disc model may be the oldest method to assess the aerodynamic performance of wind turbines. The model is based on the one-dimensional conservation equations as originally formulated by (Rankine, 1865) and (Froude, 1889). The geometry and the viscous flow over the blades is not resolved, but the swept area of the blade is replaced by surface forces acting upon the incoming flow. Combining the method with blade-element analysis has resulted in the commonly known BEM theory. Later developments have led to the integration of actuator discs in the NS or Euler equations (Lavaroni et al., 2014). These CFD models can be used to analyze different wake states of a wind turbine, the interaction of wind turbines within a wind farm or the effect of the thermal stratification within the athmospheric boundary layer.

BEM is the most commonly used aerodynamic model to determine the loads on a wind turbine. It has earned its popularity due to its computational efficiency and simplicity. The first version of BEM was introduced by (Glauert, 1935) and consisted of a combination of one-dimensional momentum theory and blade element theory to obtain the loading over the span of the blades. However, the formulation of the governing equations contains a number of assumptions that greatly limits the method (e.g. steady flow). Over the years, different correction models have been developed to improve the method for its deficiencies, such as the dynamic wake model (Snel and Schepers, 1995), yaw/tilt model (Schepers and Snel, 1995) and dynamic stall model (Hansen et al., 2004). However, BEM still contains some major drawbacks, which even become more prominent with the rise of continuously growing blade designs. For structural reasons, thick airfoil profiles are used at the inboard section of the blades. It is difficult to obtain good and reliable airfoil data for these profiles, even for low angles of attack. Besides, because of the rotation of the wind turbine, the boundary layer is subjected to

centrifugal and Coriolis forces, which alters the two-dimensional airfoil characteristics obtained from wind tunnel testing.

Many three-dimensional inviscid aerodynamic models are developed as an attempt to capture the three-dimensional flow development around wind turbines more accurately. The lack of inclusion of viscous effects restrains the usage of such models on wind turbines. However, it contributes greatly in obtaining a better description of the dynamic inflow and overall flow development over and past the wind turbine. Including a model for the three-dimensional boundary layer flow would enhance the predictive capability of such methods considerably (Van Garrel, 2016). There are some examples of methods where boundary layer equations are coupled to a three-dimensional inviscid flow field representation using the Euler equations (Sørensen et al., 1986; Mughal, 2005). However, these methods have not yet reached the maturity as the models used in industrial practices.

The previous referred models have one common advantage over NS methods. They are relatively cheap regarding computing times. On the other hand, NS solvers contain more physics and do not depend on empirical models. They are superior in the detailed investigation of flow phenomena that can not be assessed by the simpler and less computationally expensive methods described above. The NS equations can be solved using different modelling strategies, which will be discussed in the upcoming sections.

2.3.2. RANS MODELLING

The most common approach to solve the NS equations is by time-averaging the governing equations resulting in the Reynolds-averaged Navier-Stokes (RANS) equations. The time-averaged quantity of the flow variables can be mathematically expressed as:

$$\overline{\phi}(\mathbf{x}) = \lim_{T\to\infty} \frac{1}{T}\int_0^T \phi(\mathbf{x}, t)\,dt \tag{2.3}$$

Where ϕ denotes the corresponding flow variable.
All instantaneous flow variables are decomposed into a mean and fluctuating part:

$$\phi = \overline{\phi} + \phi' \tag{2.4}$$

Here $\overline{\phi}$ is the mean part and ϕ' is the fluctuating part of the flow variable.
Since the RANS solves steady flow, an alternative model is required to solve for unsteady aerodynamics. Unsteady RANS (URANS) is a slightly adapted scheme that is able to perform transient simulations:

$$\phi = \overline{\phi} + \phi' + \phi'' \tag{2.5}$$

Here $\overline{\phi}$ is the steady part of the mean flow, ϕ' denotes the resolved unsteady part and ϕ'' is the modelled turbulence.
The origin of most CFD codes lies in the aerospace industry, hence most codes are based on the compressible NS equations. The compressible NS equations can be defined as follows:

$$\frac{\partial \rho}{\partial t} + \frac{\partial \rho u_i}{\partial x_i} = 0 \tag{2.6a}$$

$$\frac{\partial \rho u_i}{\partial t} + \frac{\partial \rho u_i u_j}{\partial x_j} = \rho f_i - \frac{\partial p}{\partial x_i} + \frac{\partial \tau_{ij}}{\partial x_j} \tag{2.6b}$$

$$\frac{\partial \rho(e+\frac{1}{2}u_i u_i)}{\partial t} + \frac{\partial \rho u_j(h+\frac{1}{2}u_i u_i)}{\partial x_j} = \rho u_i f_i + \frac{\partial u_j \tau_{ji}}{\partial x_j} + \dot{Q} - \frac{\partial q_j}{\partial x_j} \tag{2.6c}$$

Here ρ is the density, u_i is the flow velocity in the i-th direction, t is the time, f_i are body forces, p is the pressure, e is the internal energy, h is the specific enthalpy, τ_{ij} is the stress tensor of a Newtonian fluid: $\tau_{ij} = 2\mu\big(s_{ij} + \frac{1}{3}\delta_{ij}\frac{\partial u_k}{\partial x_k}\big)$, where the stress-rate tensor s_{ij} is given as $s_{ij} = \frac{1}{2}\big(\frac{\partial u_i}{\partial x_j} + \frac{\partial u_j}{\partial x_i}\big)$ and the convective heat flux q_j is found from Fourier's law: $q_j = \kappa\frac{\partial T}{\partial x_j}$, where κ is the heat-conduction coefficient.
The compressible NS equations have to be averaged in slightly different fashion. When the incompressible NS equations are time-averaged, the Reynolds stress tensor originates in the momentum equations and needs to be closed. Time-averaging of the compressible flow equations results in a triple correlation involving ρ', u'

and v', increasing the complexity of the closure problem. Hence, it would be sufficient to simplify the averaging problem. Instead of applying time-averaging, so-called Favre-averaging or density-weighted averaging (Favre, 1965) is applied:

$$\widetilde{\phi} = \frac{\overline{\rho\phi}}{\overline{\rho}} \tag{2.7}$$

The instantaneous flow variables from the NS equations are now defined as:

$$\phi = \widetilde{\phi} + \phi'' \tag{2.8}$$

The density is time-averaged: $\rho = \overline{\rho} + \rho'$.
Applying the Favre-averaging to the compressible NS equations yields:

$$\frac{\partial \overline{\rho}}{\partial t} + \frac{\partial}{\partial x_i}(\overline{\rho}\widetilde{u_i}) = 0 \tag{2.9a}$$

$$\frac{\partial}{\partial t}(\overline{\rho}\widetilde{u_i} + \frac{\partial}{\partial x_j}(\overline{\rho}\widetilde{u_i}\widetilde{u_j}) = -\frac{\partial \overline{p}}{\partial x_i} + \frac{\partial}{\partial x_j}(\overline{\tau_{ij}} - \overline{\rho u_i'' u_j''}) \tag{2.9b}$$

$$\frac{\partial}{\partial t}[\overline{\rho}(\widetilde{e}+\frac{1}{2}\widetilde{u_i}\widetilde{u_i})+\frac{1}{2}\overline{\rho u_i'' u_j''}]+\frac{\partial}{\partial x_j}[\overline{\rho}\widetilde{u_i}(\widetilde{h}+\frac{1}{2}\widetilde{u_i}\widetilde{u_i})+\widetilde{u_j}\frac{\rho \hat{u_i''} u_j''}{2}] = \frac{\partial}{\partial x_j}[\widetilde{u_i}(\overline{\tau_{ij}}-\overline{\rho u_i'' u_j''})-\overline{q}-\overline{q u_j'' h''}+\overline{\tau_{ij} u_i''}-\overline{\rho u_j''\frac{1}{2}u_i'' u_j''}] \tag{2.9c}$$

The last term from the momentum equation, $R_{ij} = \overline{\rho u_i'' u_j''}$ is the Favre-averaged Reynolds stress tensor. This additional term can be modelled with different closure models.

Compressible RANS codes are designed to solve flows in the subsonic and transonic regime, however the flow velocities over a wind turbine does not come close to those speeds. Especially at the blade's root the local Mach numbers are expected to be low. The solver could have convergence problems if Mach numbers become below 0.1 (Tweedt et al., 1997). If so, most solvers have the capability of applying low-Mach preconditioning. The system of eigenvalues is changed by pre-multiplying the time derivatives by a matrix, which decreases the acoustic wave speed in the equations (Turkel et al., 1996), assuring good convergence properties at all speeds.

TURBULENCE MODELLING

As mentioned in the previous section, averaging of the NS equations leads to additional unknowns that must be solved with additional equations. These additional equations are called closure formulas. The number of equations that have to be solved to find the values of these additional terms determine the complexity of the turbulence model. Many turbulence models are based on the Boussinesq hypothesis. In 1877, Boussinesq proposed (Boussinesq, 1877) that the Reynolds stresses could be linked to the mean rate of deformation, which is consequently linked to the viscosity:

$$R_{ij} = -\rho\tau_{ij} = -\rho\overline{u_i' u_j'} = \rho\nu_t(\frac{\partial u_i}{\partial x_j} + \frac{\partial u_j}{\partial x_i}) \tag{2.10}$$

Here ν_t is the eddy viscosity that has the same dimensions as molecular viscosity.
Over the years many turbulence models are developed that determine the eddy viscosity. The most basic turbulence models are described as algebraic (Wilcox, 2006). For computational simplicity, the eddy viscosity is often defined in terms of a mixing length. (Prandtl, 1926) described that the mixing length is the distance that a fluid parcel keeps it original characteristics before dispersing them into the surrounding fluid. The Cebeci-Smith model, Johnson-King model and Baldwin-Lomax model are examples of modern variants of the mixing length model that all make a distinction in eddy viscosity modelling between the inner and outer layer of the boundary layer. These models are very simple and rarely cause strange numerical difficulties (Wilcox, 2006). However, since these models are incomplete, certain closure coefficients must be defined beforehand. Hence, they are only suitable for type of flows where they are fine-tuned for. They will not work sufficiently if it is required to extrapolate beyond the established data base where the model is calibrated for. All three models provide good skin friction and velocity profiles for incompressible boundary layer, where the pressure gradients are not too strong. Neither model is able to predict separated flows accurately.

For all models that are discussed here, the Boussinesq approximation is assumed valid:

$$\tau_{ij} = 2\nu_t S_{ij} - \frac{2}{3}k\delta_{ij} \tag{2.11}$$

Here S_{ij} is the mean strain-rate tensor,k is the turbulent kinetic energy and τ_{ij} is the specific Reynolds-stress tensor.
As computers have increased power, more complex turbulence models have been introduced that are based upon the equation for turbulent kinetic energy or a postulated equation of the eddy viscosity. One of these two equations is incorporated in these models to introduce non-local and flow history effects in the eddy viscosity. The transport equation for turbulence kinetic energy is defined as follows:

$$\frac{\partial k}{\partial t} + u_j\frac{\partial k}{\partial x_j} = \tau_{ij}\frac{\partial u_i}{\partial x_j} - \epsilon + \frac{\partial}{\partial x_j}\left[\nu\frac{\partial k}{\partial x_j} - \frac{1}{2}\overline{u_i' u_i' u_j'} - \frac{1}{\rho}\overline{p' u_j'}\right] \tag{2.12}$$

Where ϵ is the dissipation per unit mass: $\epsilon = \overline{\frac{\partial u_i'}{\partial x_k}\frac{\partial u_i'}{\partial x_k}}$.
The so-called one-equation and two-equation turbulence models are used to close the transport equation of turbulence kinetic energy or eddy viscosity. One-equation models that solve the turbulence kinetic energy equation are incomplete, since the dissipation term in the equation is unknown. Although two-equation turbulence models have recently become more popular, the S-A model (Spalart, 2000) is very promising. This model solves the transport equation for the eddy viscosity and is complete in the sense that it involves no adjustable functions or coefficients. The S-A predictions are quite satisfactory for a wide range of flows, however it fails in accurately reproduce the correct jet spreading wakes, which gives concerns regarding the analysis of wakes. Universal models that are better capable of reproducing separated flows, are two-equation models that do not only account for the computation of the turbulence kinetic energy but also for the turbulence length scale or an equivalent.

The first two-equation model is the $k-\epsilon$ model (Launder and Spalding, 1972), which is based on the transport equations of the turbulence kinetic energy k and the dissipation ϵ. Contrary to the S-A model, this model is superior in predicting the spreading of turbulence in already turbulent flow. Unfortunately, it has problems with predicting flow separation accurately. Therefore the model would be rather unreliable in predicting the flow over thick, strong curved surfaces such as the inboard profiles of a wind turbine blade. Besides, it is extremely difficult to integrate the model over the viscous sublayer. Viscous corrections must be made to reproduce the law of the wall in an incompressible flat-plate boundary layer.
The second model is the $k-\omega$ model (Wilcox, 1988). This model is almost the same as the $k-\epsilon$ model, but the small difference between both models has a large effect. The transport equation for the dissipation rate ϵ is replaced with the transport equation for the specific dissipation rate ω. It is more beneficial to use this model as it is significantly more accurate in describing two-dimensional boundary layers with either favorable or adverse pressure gradients. The $k-\omega$ model is improved for low Reynolds number flows, compressibility and shear flow spreading. Its drawback is that the solution for free-shear flows is very dependent on the freestream value of ω.
It is well known that the two above named models have their advantages and disadvantages. The $k-\epsilon$ model is not able to predict boundary-layer flow with high adverse pressure gradients, while the $k-\omega$ model has problems with predicting free-shear flows accurately (Menter, 1992). In order to obtain a superior turbulence model, the two above mentioned models are blended. The SST k-ω model combines the best of two worlds. The use of the k-ω model at the inner parts of the boundary layer makes the model directly usable to describe the viscous sublayer without using viscous corrections. The Shear-Stress Transport formulation (SST) switches to the k-ϵ model in the freestream and therefore avoids the dependency of the solution on the freestream turbulence properties. The model produces a bit too high turbulence levels in regions of large normal strains (e.g. stagnation points), but this effect is less pronounced as with the standard k-ϵ model.

(Sørensen et al., 2002) simulated the NREL Phase VI rotor using the SST k-ω model and concluded that the results satisfied the experimental data for most cases except for medium wind speeds. Under these wind speeds massive flow separation and flow transition occurred. The SST k-ω model can also be an excellent platform for the addition of transitional models, such as the $\gamma - Re_{\theta t}$ model, which significantly enhances the performance at inboard regions (Moshfeghi et al., 2012).

An alternative approach to resolve the free-stream dependency of the k-ω is proposed by (Kok, 2000). The theoretical analysis in this study has derived a new set of constraints which the diffusion coefficients must satisfy to resolve the problem. A new set of diffusion coefficients is chosen accordingly and it is proven that they allow an accurate near-wall solution for constant-pressure boundary layers without the introduction of blending functions or computing the wall-distance. The modified turbulence model is known as the k-ω TNT model.

A more sophisticated approach that uses an alternate relation to the linear-Boussinesq approximation, is the Explicit-Algebraic Reynolds-Stress Model (EARSM). The nonlinear constitutive modelling is discussed in more detail in the following article (Hellsten, 2019). This constitutive relation for the Reynolds stress tensor can be coupled to any two-equation model platform (EDGE, 2010). (Hellsten, 2019) proposed an EARSM $k-\omega$ turbulence model. The EARSM approximation is not perfectly valid in strongly curvature or fastly rotating flows. However, due to the incorporation of the anisotropy term, improvements over the reference models were achieved in predicting mildly separated flows, and the evolution and merger of wakes.

All above described turbulence models are available in `ENSOLV`, except for the S-A and k-ϵ model. It is chosen to use either the SST k-ω or EARSM k-ω model. Both turbulence models are good in predicting mildly separated flows and therefore are suitable of simulating wind turbine blades with thick inboard cross-sections. However, it is reported that the EARSM k-ω behaves poorly in rapidly rotating flows and flows over strong-curved surfaces (Wallin and Johansson, 2002). Hence, a slight preference in using the SST k-ω model is developed.

2.3.3. LES MODELLING

Large-Eddy Simulation (LES) is an alternative method to solve the NS equations using spatial filters, resolving a part of the turbulence length scales (RANS models the full turbulence spectrum). For this reason, LES is better in capturing large turbulent flow structures than RANS. As smaller turbulent length scales are more universal, they are easier to model and therefore subgrid-scale (SGS) modelling is applied in these flow regions. Since small-scale turbulence only has a small influence on the large resolved turbulent structures, the error introduced by the modeling is low.

(Spalart, 2000) wrote a paper to clarify the many levels of fidelity for the numerical prediction of turbulent flow over a large body like a complete airplane, car or turbine. He stated that turbulence predictions face two primary challenges:

- The growth and the separation of the boundary layer.
- The momentum transfer after separation.

The first challenge is rather simple, but requires large accuracy. It appears that more complex models do not obtain a large advantage over lower-fidelity methods in predicting the development of the boundary layer. For the second challenge, newer strategies with complex time-dependent RANS or hybrid RANS-LES models are embedded. Some studies investigated the effect of grid refinement on the numerical error, while other studies aimed at introducing richer physics in the models. LES is not considered to solve the full flow domain around a wind turbine, as it is still computationally unaffordable in large simulation spaces. To alleviate the tension between predicting power and computing power, many hybrid models are developed that combine LES and RANS.

Spalart proposed a method, called Detached Eddy Simulation (DES) (Spalart et al., 1997), that combines RANS and LES into an hybrid model using the S-A turbulence model as cornerstone. The DES method is a non-zonal approach that switches between models based on the turbulence length scale and the grid spacing. The S-A turbulence model contains a destruction term for the eddy viscosity $\tilde{\nu}$, which scales with $(\frac{\tilde{\nu}}{d})^2$, where d is the distance to the closest wall. When the destruction term is balanced by the production term, the eddy viscosity scales with the deformation rate and the distance to the wall: $\tilde{\nu} \propto Sd^2$. The Smagorinksy model scales it SGS eddy viscosity with: $\nu_{SGS} \propto S\Delta^2$, where Δ is the largest grid spacing in one of three directions. Thus if d is replaced by Δ, the S-A model can also serve as SGS model.

Intuitively, there may originate a problem where d and Δ are of the same order, which is also known as the "grey area". The model will switch from RANS to LES, while the resolved turbulence does not balance the reduction in modelled eddy viscosity (Gritskevich et al., 2012). This numerical flaw is called Model-Stress Depletion (MSD). It could lead to nonphysical behavior, such as an underestimation of the skin friction, which would result in a shift of the separation line. This flow effect is called Grid-Induced Separation as it depends on the grid spacing and not on the actual flow physics. To overcome this problems, *Spalart* proposed the introduction of a shielding function that protects the RANS formulation for the DES formulation in wall bounded boundary layers. The modified formulation of DES is called Delayed Detached Eddy Simulation (DDES)(Spalart et al., 2006).

NLR has also developed a hybrid model that varies slightly from DES and DDES. The Extra-Large Eddy Simulation (X-LES) method applies a non-zonal treatment to combine RANS and LES using a single turbulence kinetic energy equation (De Cock et al., 2004). In most RANS-LES models it is difficult to define a smooth transition at the interface of both models. RANS often uses time-averaging, while LES uses spatial filters to split the turbulence length scales. Most hybrid RANS-LES methods employ these two filters in different regions of the flow domain leading to a discrepancy in the exact definition of the flow variables. In particular, the turbulent kinetic energy is defined differently, which may cause a wrong coupling at the interface. To overcome this problem, a temporal filter can be used in the LES formulation. However, a drawback is that the subgrid stresses are not Galilean invariant anymore. Hence, temporal filtering can only be applied where the flow resembles free-shear flow. The model switches from LES to RANS when the turbulent time scales are too small to be resolved by the temporally filtered flow solution.

LES-based methods are superior in predicting separated flows. However, they require very high grid standards and therefore are computationally very expensive for large-domain simulations. Besides, previous studies have shown that RANS delivers sufficient accuracy in wind turbine aerodynamics. For that reason, it is chosen to use RANS as fluid model in this study.

2.4. STRUCTURAL MODELS

In this section, an overview of different structural models implemented in aeroelastic models is given. In general, first a low-fidelity structural model is used to calculate the structural response of a wind turbine. At a later stage, a high-fidelity structural model can be used to calculate the internal stresses throughout the different laminate layers and perform buckling analyses.

From section 2.2, it can be concluded that the most used structural solvers are: the 1D modal approach and beam models (both linear and nonlinear). This section elaborates on the principles and performance of these models. The Multi-Body Dynamics approach is omitted from the literature review, since it is mainly used to define the interaction between different components, while this study focuses on the isolated wind turbine rotor (two blades and hub).

2.4.1. BEAM MODELS

Two widely used linear beam models are the Timoshenko beam and the Euler-Bernouilli beam. These models contain the assumption of small deformations. Structural modelling of wind turbines is often based on classical beam theory (Riziotis and Voutsinas, 1997; Hansen and Laino, 1997). This is due the fact that wind turbine blades are more rigid than helicopter blades and therefore have a higher stiffness. However, *Hansen et al.* stated that if wind turbine blades become longer and more flexible, it can become necessary to adopt second-order nonlinear beam theory (Hansen et al., 2006).

(Larsen and Hansen, 2004) presented three modifications to the structural part of the aeroelastic code HAWC to account for nonlinear effects (Horizontal-Axis Wind Turbine Code). HAWC is an aeroelastic code consisting of different subpackages, each dealing with a specific part of the wind turbine. The main program of HAWC is the structural model, which is a FEM model using Timoshenko beam elements. Each substructure (e.g. tower and blades) is built up from these 1D beam elements. The sub-structure model only accounts for linear deflections and the loads are placed on the undeformed state of the beam elements. This could result in inaccurate computations of the pitching moment for a deflected blade (Larsen and Hansen, 2004). In deflected state, a significant moment arm to the pitching axis is created, producing a large contribution to

the total pitching moment. Therefore the model is not valid for large rotations and displacements. *Larsen et al.* applied the following three modifications to the HAWC code and evaluated the result:

- The calculation basis of the displacements is changed from an undeformed state to an initially deformed state.
- A multi-body formulation is adopted. The coupling between the bodies is defined using coupling functions. Due to the coupling of multiple linear beams, the total system of bodies is able to account for large displacements and rotations.
- A local reference frame is assigned to each beam element, such that within that frame the displacements are small (and linear).

In recent years also a lot of research is dedicated to the development of nonlinear beam models. These models do not require modifications to account for large rotations or deformations. An extensively investigated nonlinear beam model is the geometrically exact beam theory (GEBT) (Hodges, 2003; Jelenić and Crisfield, 1999), in which the deformed state of the blade is determined exactly.

(Yu and Kwon, 2013) and (Carrión et al., 2014) have implemented nonlinear beam theory in their aeroelastic frameworks. *Carrion et al.* used the commercial finite element solver Nastran to perform the structural calculations. However, it is not possible to draw any conclusions about the performance of the nonlinear beam model, since no aeroelastic data is available from the experiments. Besides, since both wind turbine models are quite stiff, the deformations are small and presumably nonlinear effects are not significant. In the study of (Yu and Kwon, 2013), it is observed that the static aeroelastic deformations of the reference wind turbine compare well with the design values predicted by the FAST AeroDyn method.

2.4.2. LINEAR MODAL THEORY

Using modal theory is an effective way to describe the deflection of flexible bodies, while reducing the number of DOF's. The deflection shape is described as a linear combination of a few, but realistic basic functions, which are often the deflection shapes (eigenmodes) corresponding to the lowest eigenfrequencies of the structure (Hansen et al., 2006). The superposition of the eigenmodes of a system could describe the dynamic behavior of the system. Only a limited number of eigenmodes have to be included in the analysis, since it can be assumed that high-frequency modes are strongly damped. It should be noted that the number of included modes should be chosen wisely in order to obtain accurate responses. Besides, the method is only valid for small displacements as the superposition of mode shapes is based on linear theory. The displacements of the structure can be defined as follows:

$$\Delta \mathbf{x}(x, y, z, t) = \sum_{i=1}^{n} \mathbf{h_i}(x, y, z) q_i(t) \tag{2.13}$$

Where $\mathbf{h_i}$ is the modal shape of the i-th mode and q_i is the corresponding generalized coordinate.

In most commercial codes only the first three or four mode shapes are used per blade (Hansen et al., 2006), leaving out the torsional mode. However, large flexible blades often have bending-torsion coupling to alleviate the loads at high wind speeds (Fedorov and Berggreen, 2014). Therefore, torsional modes become increasingly important in the aeroelastic analysis of wind turbine blades.

(Guo et al., 2013) employed a modal approach to obtain the dynamic response of the wind turbine blade under aerodynamic loading. A predictor-corrector scheme was used to solve the structural equations of motion, enabling a tight coupling between aerodynamics and structural dynamics. The aeroelastic characteristics of the wind turbine are analyzed by evaluating the generalized coordinate response and structure response in the time domain. The study primarily focused on the performance of the fluid model, so no solid conclusions can be drawn about the performance of the structural model.

It can be concluded that the modal approach would only be useful in dynamic aeroelastic analysis, where the displacements are assumed small. Large static deflections will be most certainly not captured accurately utilizing a limited number of mode shapes.

2.4.3. 3D FEM

In 3D modelling, generally 2D composite shell elements or 3D solid elements are used which are capable of describing the material characteristics of different composites through the element thickness. A correct description of the complex aerodynamic shape and complicated laminated structural layout of a wind turbine requires the use of commercial finite element packages, such as `Nastran` (MSC Software Corporation, 2017).

However, processing the geometry in these packages is tedious and time-consuming. 3D FEM is an excellent tool to examine the stress distributions within the material, but is somewhat redundant in aeroelastic analysis. In case there is already a 3D FEM model available, it would give superior results, when coupling it to an aerodynamic model. But still, it is questionable if it is profitable to use a structural model with so many DOF's.

Commercial finite element solvers often have the feature of applying model reduction techniques in order to reduce the number of DOF's. (Flanigan, 1998) described three reduction approaches: Guyan reduction, improved reduction system and dynamic reduction. The development of these reduction approaches originated from the necessity to verify FEM models with experiments. Generally, the FEM model has more DOF's than the test model contains accelerometers. Hence, the FEM model had to reduced to a Test-Analysis Model, for which the DOF's correspond one-on-one with the accelerometers on the test configuration.

The three reduction techniques reviewed differ in ease, accuracy and required computation resources. The simplest reduction technique is the Guyan reduction method. The major advantage of this method is that it is computationally very efficient and easy to implement. Guyan reduction is a standard option in the finite element codes `Nastran` and `SDRC I-DEAS`. The largest drawback is that the method does not account for the mass effects of the omitted DOF. Therefore, this method is not suitable for structures with very high mass/stiffness-ratios. Both other models are modified versions of the Guyan reduction approach including a correction or approximation for the mass effects. However, these methods are computationally expensive and need additional computational resources. In general, Guyan reduction is most used, because of its simplicity and greater experience base.

Also, it has the characteristic of giving an exact formulation of the stiffness property. Hence, this technique would very useful in static aeroelastic computations.

2.4.4. CLASSICAL LAMINATION THEORY

Most state-of-the-art wind turbine blades are made of sandwich laminates. Hence, it is worth the effort to seek for structural modelling methods that are capable of describing the characteristics of composite laminates. Classical Lamination theory (CLT) is a fast method that adopts some effective and reasonable accurate simplifying assumptions that reduce the complex three-dimensional elasticity problem into a manageable and solvable two-dimensional mechanics of deformable bodies problem (Kaw, 2006).

`Nastran` has the possibility to describe composite laminates ply-for-ply. Three methods are available that model an entire stack of laminae with a single element and compute the matrices of elastic moduli of the element automatically. The user guide of `Nastran` (MSC Software Corporation, 2017) describes the assumptions and the derivation of the structural equations using CLT elaborately.

We4Ce provided a 3D FEM model that is compatible with `Nastran`. No effort has been put in constructing a different model.

2.5. FSI MODELS

One of the conclusions that can be drawn from section 2.2 is that aeroelastic model consists of different sub models. In addition to the fluid and structural model, an aeroelastic model comprises of a spatial coupling algorithm, mesh deformation algorithm, time integration scheme and time coupling scheme. Since, this study is limited to the available modelling techniques in `ENSOLV`, only important aspects in the fluid-structure coupling are mentioned.

2.5.1. MONOLITHIC VS. PARTITIONED APPROACH

There are two basic approaches to model the complete aeroelastic system: the partitioned and monolithic approach. The monolithic approach solves one complete system that involves both structure and aerodynamics. The partitioned approach solves the flow and structural equations separately and interchanges data between them. A large disadvantage of the monolithic approach is that it is problem-specific and therefore lacks a degree of flexibility. In turn, the partitioned approach needs additional models to couple both models, which is a source of errors. However, if it is used correctly, the partitioned approach is just as good as monolithic approaches (Van Zuijlen, 2014). Moreover, the partitioned approach allows different structure of aerodynamic models to be tested within the same overall framework.

`ENSOLV` incorporates a partitioned approach, where the simulation process is fully automated. The elasto-mechanical information of the structure (i.e. mass and stiffness matrix or mode shapes) are computed in advance using `Nastran` and are used in the structural equations to determine the structural response.

2.5.2. CONSISTENT VS. CONSERVATIVE APPROACH

In FSI simulations, the meshes at the interface of the flow and structure domain are usually non-matching (see figure 2.3), since both models require different mesh requirements. Data exchange must be transferred over the discrete interface. There are two common approaches in transferring data: the consistent approach and conservative approach.

Pressure forces from the aerodynamic model has to be transferred to the structural mesh and, in turn, the displacements of the structural model must be transferred to the aerodynamic mesh. The data exchange can be defined as follows:

$$(\mathbf{h^a}) = [G_{as}](\mathbf{h^s}) \tag{2.14a}$$

$$(\mathbf{F^s}) = [G_{sa}](\mathbf{F^a}) \tag{2.14b}$$

Here $[G_{as}]$ and $[G_{sa}]$ are the interpolation matrices, $\mathbf{h}$ are the displacements and $\mathbf{F}$ are the forces or pressures. The general opinion says that energy must be conserved over the interface (De Boer et al., 2008). The conservative-coupling approach is based on the global conservation of virtual work. However, nonphysical oscillations of the pressure forces might be transmitted to the structure mesh (Ahrem et al., 2001). These oscillations influence the accuracy of the solution and can slow the convergence process down, especially for flexible structures where the oscillations could result in deviations in the displacement of the fluid interface. The consistent-coupling approach ensures that the interpolation keeps the sum of forces constant. This leads to a transfer approach without nonphysical pressure distributions over the structure's surface. However, the energy is not always conserved, but this does not have to be a problem. In loosely-coupled unsteady simulations, the temporal error (time-lag of structure's response to force changes) already causes the energy not to be conserved. So, if the error of data transfer is significantly smaller than the time-discretization errors, the accuracy and stability of the solution will not be affected.

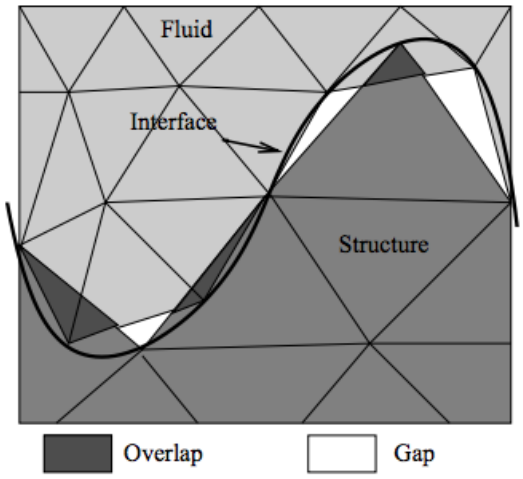

Figure 2.3: Non-matching interface for fluid and structure mesh (Bijl et al., 2008)

Many different spatial-coupling algorithm are developed in the past decades. Neither these methods will be discussed here.

ENSOLV employs a three-dimensional volume-spline interpolation (VSI) based on biharmonical operators as spatial-coupling method, which is both energy conserving and consistent (Hounjet and Meijer, 1995). However, it is not very economical to solve the associated equations to obtain the interpolation matrix. The number of support points should therefore be limited.

2.5.3. COUPLING IN TIME

When a partitioned system is supposed to perform transient simulations, it requires timing of the data exchange between the two disjoint fields. The information exchange must be carried out in a time-marching manner, meaning that one model can not progress any further than the other model. However, this does not imply that both models require the same time step.

Despite that the structural and aerodynamic equations are solved separately, the coupling of both models allows to observe the coupled system as one system of nonlinear equations. Basically two approaches can be found to solve the system of nonlinear equations in partitioned schemes: loosely-coupled and strongly-coupled algorithms (De Boer, 2008). In loosely-coupled schemes the structure and fluid are only solved once at each time step. This approach introduces an error due to the time-lag between both models, which could give rise to numerical instabilities. Reducing the time step could prevent the solution to be unstable. Strongly-coupled schemes introduce sub iterations within each time step, leading to a more robust coupling scheme. Strongly-coupled approaches should in theory converge to the solution of a monolithic approach (Bijl et al., 2008), where the equilibrium conditions at the interface are met in an exact manner.

There exist several time-coupling methods (e.g. Block-Jacobi, Gauss-Seidel, staggered schemes, ESDIRK IMEX (Bijl et al., 2008; Van Zuijlen, 2014)) that all vary in efficiency and accuracy. A balance must be sought between numerical accuracy and computational resources required to execute the coupling. Choosing a scheme that allows to use large time steps is rewarding. Hence, fully-coupled explicit Runge-Kutta schemes are not suited, since they require small time steps given their stability issues. Implicit time-integration schemes have the characteristic of allowing larger time steps, however iterative schemes are required to solve the coupled equations simultaneously (Prananta, 1999).

In order to avoid excessive computation times, a loosely-coupled staggered approach (see figure 2.4) is incorporated in ENSOLV. The coupling scheme is based on an extrapolation procedure of either the structural displacements or aerodynamic forces to the next time step. The method allows to update the structure and mesh within sub iterations, which transforms the coupling scheme into a strongly-coupled approach.

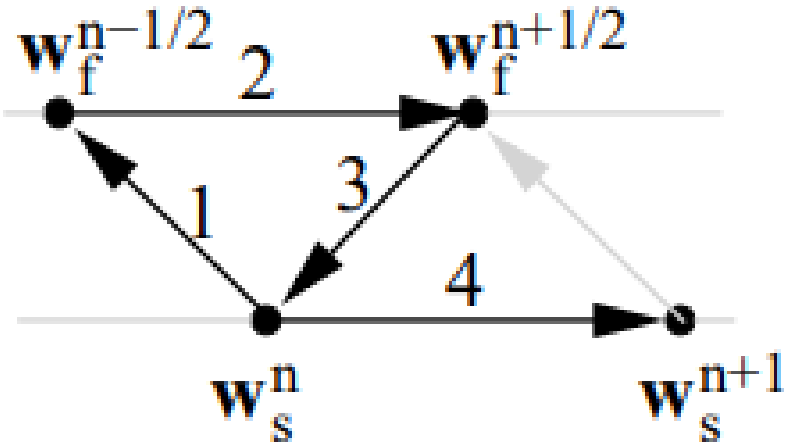

Figure 2.4: Caption

2.5.4. TIME-INTEGRATION SCHEMES

In unsteady simulations the governing equations of structure and fluid must also be discretized in time. After discretizing the solution domain in space, the system becomes semi-discrete, forming the following equation:

$$\frac{d\mathbf{W}}{dt} + \mathbf{R}(\mathbf{W}) = 0 \tag{2.15}$$

Here $\mathbf{W}$ is a vector containing the discrete solution in the finite volume cells or finite element nodes and $\mathbf{R}$ is a vector with the residuals of the equation that arose due to the spatial coupling of the governing equations. The first term is continuous in time and should be discretized using an explicit or implicit time integration scheme to fully discretize the governing equations. Explicit time-integration schemes only use the solution of previous time steps to produce the solution at the next time step. These methods are very straightforward in the sense that all information is readily available, however often small time steps are required to ensure stability. Implicit-time integration schemes also include information from future states, hence it requires to solve a system of equations each time step to determine the solution at the current time step. Therefore, these schemes require more computational resources, but they allow to use larger time steps without dealing with stability issues. Implicit schemes are popular because of their robustness.

ENSOLV uses the second-order backward difference method as time-integration scheme. The dual-time stepping method of (Jameson, 2012) is adopted to solve the system using fictitious time steps. The basic idea of this approach is to introduce fictitious time steps into the computation, so that the unsteady problem becomes a quasi-steady problem. Each time step basically solves a steady-state problem. This solution scheme is advantageous, because it gives the possibility to apply local time stepping and implicit methods for convergence acceleration (Jameson, 2012).

2.5.5. MESH-DEFORMATION ALGORITHMS

High-fidelity flow solvers that are used in aeroelastic applications require the use of computational meshes that deform as the structure is displaced. Wind turbine blades demand high robustness of the mesh-deformation algorithm, because they are often flexible and reach displacements that are a significant fraction of their total length. Besides, it is important that they are computationally cheap to mitigate the turn-around time of the aeroelastic computations. Furthermore, the mesh-deformation algorithm must possess the characteristic to keep the properties of the initial grid equally(e.g. grid distributions in the boundary layer).

In general two type of mesh-deformation strategies exist: point-by-point schemes and grid-connectivity-schemes (Bijl et al., 2008). The former method moves each node individually based on its position in space, while the latter exploits the connectivity of the internal grid points. Only the available mesh-deformation techniques implemented in ENSOLV are discussed next.

TRANSFINITE INTERPOLATION

Transfinite interpolation (TFI) is known as an easy and efficient method to deform single-block or multi-block structured grids. A multi-block grid is a collection of structured grids that fill the entire flow domain. The internal nodes of the separate blocks are displaced by an interpolation from the displacements of the boundary surface nodes along the grid lines. An additional method is required to move the corner vertices and edges of the block, which are often located non-uniformly throughout the flow domain. Most TFI algorithms are based on arclength, which preserve the characteristics of the initial two-or three-dimensional grid (Bijl et al., 2008).

VOLUME-SPLINE INTERPOLATION METHOD

NLR conducted several studies that investigated different non-planar and planar interpolation techniques, which can either be used for elasto-mechanical data transfer or mesh deformation. According to (Hounjet and Meijer, 1995), the VSI method is the most promising method because it is easily coded, robust, automatic and it is able to handle non-planar and non-smooth data. The VSI method is an extension of surface spline interpolation satisfying the three-dimensional biharmonic equation or Laplacian equation. In essence, the method based on the biharmonic operator is similar to the Laplacian variant, however the biharmonic method is fourth-order where the Laplacian method is second-order. This means that two boundary conditions at each boundary can be specified, which allows to control the cell size at the boundary and the stretching of cell sizes normal to the boundary. Hence, mesh-deformation techniques based on the Laplacian operator are not suitable for viscous flow problems around flexible structures with large deformations. Although,

this method has numerous excellent properties, it is not economical to solve the governing equations, when large grids are considered.

An hybrid method between three-dimensional VSI and TFI is used in ENSOLV, whereby the internal grid nodes of each block are displaced using TFI. The corner vertices, edges or faces of the blocks can be set to be displaced by VSI. In case of grid folding, elliptical smoothing can be used to improve the quality of the mesh.

2.5.6. GEOMETRIC CONSERVATION LAW

When fluid-structure interaction is considered, the structure and thus the fluid domain deforms. There are two methods that are capable of dealing with moving boundaries: the immersed-boundary method and body-conforming mesh method. For the immersed-boundary method, both the grid and the equations remain the same, while the boundary conditions change. For body-conforming meshes, the grid adapts itself to the deformed boundaries, whereby the motion of the grid must be included in the governing equations. The Arbitrary-Langrangian-Eulerian (ALE) formulation method is discussed as it is the most common used method to include the effects of a moving grid and it is implemented in ENSOLV.

In ENSOLV, the NS equations are discretized using finite volumes in multi-block structured grids (Michaelson, 2015). The conservative form of the NS equations is needed as a starting point for deriving the finite volume formulation (Michaelson, 2015).

The discretization applied in the ALE equations has an influence on the stability and numerical accuracy of the solution method. Two issues will be addressed that deal with the quality of the discretization, the Geometric Conservation Law (GCL) and the time-integration method. The GCL characterize algorithm that can produce similar solution on uniform flow for deforming meshes.

The grid velocity is needed to compute the additional convective flux due to the grid motion. For a moving mesh, the grid velocities and cell volumes must satisfy the GCL. The GCL is derived by taking the ALE equation of the mass balance assuming uniform flow. The derivation results in:

$$\frac{\partial}{\partial t}|_{x^0} \int_{V_t} dV = \int_{S_t} \mathbf{u_g} \cdot \mathbf{n} dS \tag{2.16}$$

The GCL determines how the grid velocity is calculated. The grid velocity does not only depend on the position of the grid points at different time steps or stages, but also on the time discretization used. The structural solver only determines the position and velocity of the grid points on the interface, but the discrete velocity of the interface calculated by the structural solver is not the same as the one on the aerodynamic grid due to the use of different time-integration schemes. The velocity of the interface can be determined by simple time-integration methods, like the second-order backward finite difference scheme:

$$\mathbf{u}_{wall}^{n+1} = \frac{3\mathbf{x}^{n+1} - 4\mathbf{x}^{n} + \mathbf{x}^{n-1}}{2\Delta t} \tag{2.17}$$

However, if this scheme is also used to compute the grid velocities, it violates the GCL and therefore artificial fluxes arise. The approach implemented in ENSOLV to determine the grid velocities can be found in the following article (Prananta et al., 2000).

2.6. ROTATIONAL EFFECTS

Rotational effects are known to influence both the aerodynamics and dynamics of a wind turbine. There are two methods to incorporate these effects in the governing equations: the multiple reference approach and moving-mesh approach.

The multiple reference approach is an analytical method that uses a rotating reference frame for the inclusion of rotational effects. The method is computationally very efficient, since the mesh is kept stationary, however it does only apply for constant rotational speeds. The total acceleration of an arbitrary point in a rotating structure with respect to fixed coordinates can be defined in terms of the acceleration in the rotating reference frame (Spera, 1994):

$$\mathbf{a_t} = \ddot{\mathbf{u}} + 2\Omega \times \dot{\mathbf{u}} + \Omega \times [\Omega \times (\mathbf{r} + \mathbf{u})] \tag{2.18}$$

Here $\mathbf{a_t}$ is the total acceleration vector, $\mathbf{r}$ is origin of an element in the fixed reference frame, $\mathbf{u}$ the displacement vector observed in the rotational reference frame and Ω is the constant angular velocity.

Substitution of the above expression into the equations of motion, leads to additional terms. These terms include tension stiffening, centrifugal forces and Coriolis accelerations. The Coriolis accelerations are often neglected, because the relative velocity of the structure with respect to the rotating reference frame is usually low. The centrifugal forces affect the eigenfrequencies and mode shapes by the change of stiffness property. The dependency on these forces implies that the dynamic characteristics of a wind turbine blade depends on the speed of rotation (Bedri and Al-Nais, 2005).

The inclusion of rotational effects on the flow can be accomplished in the same way by substitution of the alternative expression of acceleration into the momentum equations. (Herráez et al., 2014) showed that the rotational effects mainly affect the inner part of the blade. The results have shown that the effect of stall delay and lift enhancement manifested themselves separately, but mainly occurred simultaneously. Rotational effects appeared to act most prominently at the aft region of the boundary layer under stall conditions. Radial flow is induced due to the centrifugal forces acting on the separated air volume. (Bangga et al., 2017) observed the same effect and added that the transportation of separated flow due to the centrifugal force leads to boundary layer thinning and hence delayed separation.

In case of uniform inflow, the size of the flow domain can be reduced by applying periodic boundary conditions (Bazilevs et al., 2011a). The aerodynamic mesh contains a single blade as it is assumed that the flow conditions over each blade are equal.

In the moving mesh technique, the rotational effects are included numerically, whereby the entire mesh is rotated. Although, this approach is computationally more demanding, it is preferred in wind turbine simulation, because it is also valid for transient simulations. This approach can be again divided into two methods: the sliding mesh technique and the overset grid technique (also known as the Chimera grid). The overset grid method employs a cylindrical rotating mesh that is placed on top of a stationary, generally Cartesian grid, such that they are overlapping. The sliding mesh technique entails a rotating cylinder separated from a stationary mesh by a discrete interface (Abdulqadir et al., 2017) as shown in figure 2.5. Coupling of the separated grids can be done using various interpolation techniques.
Both the static and dynamic aeroelastic simulations employ an analytical approach to account for rotational effects, since uniform inflow is considered in this study.

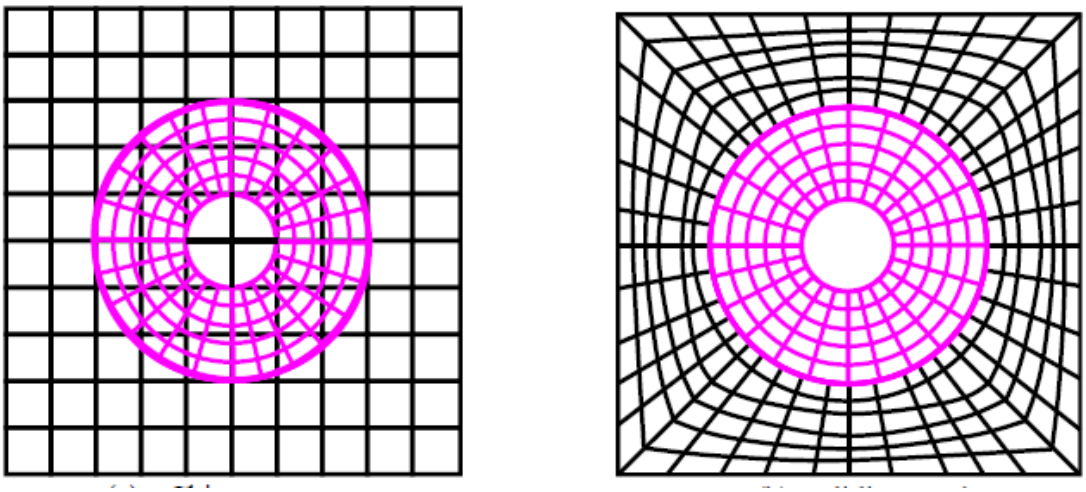

(a) The Chimera overset grid method

(b) The sliding mesh technique

Figure 2.5: Two types of moving mesh techniques (Abdulqadir et al., 2017)

2.7. FLUTTER ANALYSIS

As already mentioned earlier, current wind turbine designs should be assessed on the possible occurrence of flutter. (Lobitz, 2004) stated that the flutter speed of near future wind turbines decreases towards operational speeds. A much more recent research to the flutter prediction of a 100-meter large blade design confirms this statement (Griffith and Ashwill, 2011). In this report, *Griffith et al.* estimated the flutter speed of the SNL-100 meter blade to be 1.0-1.1 times the operational speed.

Flutter analysis methods can be divided in two types: time-domain and frequency-domain analyses. Most flutter calculations are in frequency-domain, whereby it is assumed that the vibratory motion of the structure can be described by superposition of prescribed vibrational modes (Prananta, 1999). This assumption originated from the adoption of a linear relationship between displacements and inertial, stiffness and damping forces of the structure. After obtaining the aerodynamic response for the excitation of several mode shapes for different frequencies, a complex eigenvalue problem arises, which after solving, provides the damping and eigenfrequency of the modes. There are multiple methods to determine the flutter points of an aeroelastic system in frequency-domain. The p-method, p-k method and k-method are popular flutter calculation method in aviation industry.

As current flutter methods require a large set of CFD simulations, several studies are conducted to investigate the applicability of linearized aerodynamic CFD models to flutter analysis. (Stuurman, 2016) employed a linearized method to assess flutter for an extreme scale wind turbine. It turned out that the developed approach was capable of predicting flutter-related coupling between modes, but not the instability itself. Following the study of *Stuurman*, another Dutch graduate student investigated the efficacy of linearized CFD computations for flutter analysis (Tatomir, 2019). *Tatomir* showed that the linearized force coefficients were highly dependent on reduced frequency. This implied that no set of linearized aerodynamic force coefficients could predict the unsteady air loads for harmonic airfoil motion with different reduced frequencies. Furthermore, it was concluded that the method did not account for wake effects and therefore could not predict the flutter boundaries accurately.

In time-domain flutter calculations less assumptions have to be made. An initial condition is prescribed, from which the (linear or nonlinear) equations of motions are solved using numerical integration.

2.7.1. THE K-METHOD

The k-method, also known as the V-g method, is the traditional American form of the flutter equation. This method is only valid for harmonic motion. Using the harmonic loads and introducing an artificial structural damping factor, g, the complex roots of the equations can be obtained (Heeg, 2000). The value of g represents the amount of damping that is required to keep the system oscillating harmonically. It should be negative for a stable system. It can be assumed that the system is oscillating harmonically (without decay or grow) at the flutter boundary. Therefore this method is only capable of predicting the flutter boundary (where $g = 0$).

2.7.2. THE P-METHOD

The p-method is the simplest method to understand, but may be the most difficult to apply. It gives realistic damping values throughout the entire domain and therefore it can give insight in the physical mechanisms behind the instability. However, the method is complicated because it requires an expression of the unsteady aerodynamic forces for growing and decaying motions.

2.7.3. THE P-K METHOD

The p-k method is a compromise between the p-method and the k-method. It is based on conducting a p-method type of analysis with the restriction that the unsteady aerodynamic matrix is only available for harmonic motion (Heeg, 2000). The equations of motion can be solved producing imaginary roots (Gu and Yang, 2012). The aerodynamics can then be recomputed using the frequency that resulted from the eigenvalue computation. The p-k method utilizes an iterative calculation procedure to find the reduced frequency that corresponds to the aerodynamics. The method is based on the assumption that for sinusoidal motion with slowly increasing or decreasing amplitude, aerodynamics based on harmonic motion is a good approximation. This means that only the flutter boundary is exact and the damping values in close proximity of the boundary are realistic.

2.7.4. TIME-DOMAIN METHODS

(Corson et al., 2012) attempted to find the flutter speed using a high-fidelity CFD-CSD method. The method was able to predict performance variables (e.g. thrust, torque) with reasonable accuracy in static aeroelastic simulations, but failed in predicting flutter. Two methods were adopted to find the flutter speed. The first method simulated a wind turbine rotor in still air with a time-varying rotor speed. The simulation started at 80% of the maximum rotor speed and increased its speed with 10% every 26 seconds to two times the maximum rotor speed. The tip displacement and tip speed of the wind turbine blade were monitored to evaluate the dynamic behavior. The increase in rotor speed perturbs the system sufficiently enough to induce a temporarily increase of the tip displacement. The behavior in-plane differs from the out-of-plane motion of the tip. In-plane, the temporal increase is immediately followed by a decay of the motion, while between 1.0-1.4 times the maximum rotor speed the out-of-plane displacements keeps growing. It is difficult how to interpret this behavior, but since the displacements are relatively small, the onset of flutter seems unreasonable. Increasing the duration of time at each operational condition could give a better understanding of the dynamic behavior of the blade.

Therefore, in the second approach the rotational speed is held constant and the blade is perturbed by an impulse force. The force is ramped up in five time steps, held constant for five time steps and ramped back down in either five time steps. As the force is removed, the blade is allowed to vibrate freely. For all four simulation (1.0, 1.1, 1.2 and 1.3 times maximum rotational speed), the in-plane and out-of-plane motion were characterized by an initial large-amplitude oscillation, after which the amplitudes of the oscillation decreased and the displacements converged to a mean state.

To the author's knowledge, it has not yet been possible to predict wind turbine flutter using time-domain methods, so it appears to be better to choose a method in frequency domain. Because of its simplicity and capability of exactly predicting the flutter boundary, it is chosen to use the p-k method to perform the flutter analysis.

3

METHODOLOGY

The aeroelastic framework implemented in ENSOLV requires modification to take into account structural nonlinearities. In this work, tools and software packages that were available at NLR, are employed to develop a solution strategy that could simulate highly flexible aeroelastic systems accurately.
This chapter provides an overview of the utilized software modules, the simulation conditions and the utilized solution methods. The working principle and verification of the separate sub models are discussed in chapter 4.

3.1. COMPUTATIONAL SET-UP

As mentioned in the introduction, various computational simulations were carried out comprising steady and unsteady simulations. A concise summary of the separate software packages that wee used in the simulation methodology is presented.

3.1.1. ENSOLV

The accuracy of aeroelastic analysis is highly dependent on the aerodynamic model. All flow-related simulations were performed using the in-house CFD code, ENSOLV, which is part of the ENFLOW simulation environment. ENSOLV is a multi-block, compressible CFD solver that encompasses numerous features to allow the simulation of aerodynamic, aeroelastic and aeroacoustic applications. The multi-block, structured grid is generated using ENDOMO and ENGRID, which are two separate modules of ENFLOW. The mesh-generation process is described in detail in chapter 4.
Through the years the solver has been updated and extended regularly. Different researchers contributed to the development of ENSOLV, the aeroelasticity module was mainly developed by Bimo Prananta. It must be noted that the automated aeroelastic framework is fully implemented in the ENSOLV environment, hence no coupling exists to external Computational-Structural Dynamics (CSD) packages. Elasto-mechanical data required to solve the equations of motion must be extracted from Nastran using special DMAP macros.
The mathematical formulation of the aeroelastic equations contains some minor differences depending on the aeroelastic phenomena of interest (Prananta et al., 2000); Static aeroelasticity demands a different interpretation of the flow physics than dynamic aeroelasticity. In static analysis, steady flow is generally assumed, since no vibrations are involved. The static equilibrium often contains relatively large deformations. Dynamic aeroelasticity, on the other hand, is characterized by small, time-dependent displacements causing an unsteady nature of the surrounding flow. These dissimilarities suggest a distinct formulation of the aeroelastic problem.

3.1.2. NASTRAN

Nastran is originally developed for NASA with funding of the United States government. It is a rigorously verified and validated Finite-Element Analysis (FEA) solver, which has been in widespread use for aerospace applications. Likewise, it serves as workhorse for aeroelasticity-related problems at NLR. As already briefly mentioned in the literature review, *We4Ce* provided a three-dimensional FEM model compatible with Nastran. The nonlinear finite elements and solution strategies available in Nastran are deemed sufficient for nonlinear analysis of a wind turbine blade. Therefore, no additional effort was put into the optimization of the

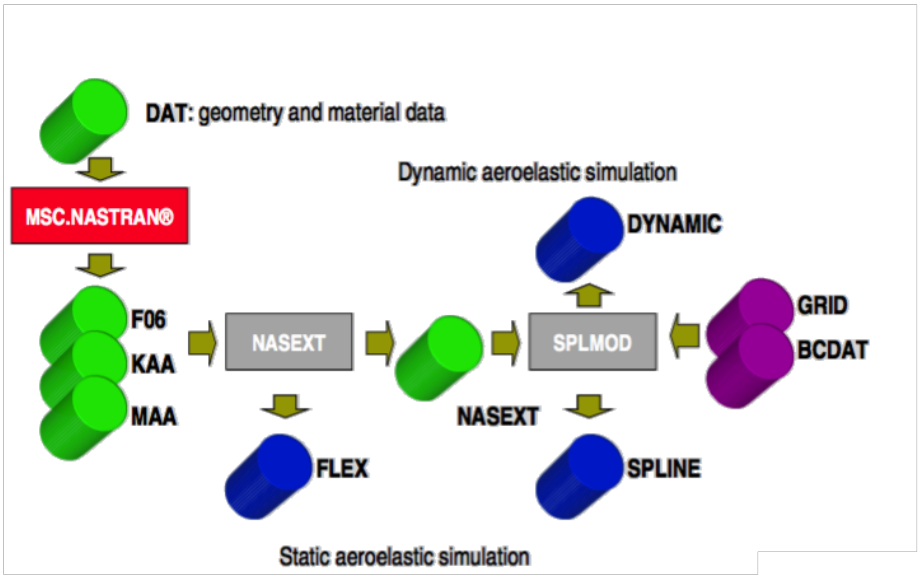

Figure 3.1: Overview of the pre-processing steps for aeroelastic simulations in ENSOLV (Kok, 2019)

structural module.

3.1.3. NLR TOOLS

NLR has developed various utilities (so called ENUTIL programs) written in ANSI Fortran 77 that perform operations required in the aeroelastic framework. The most relevant ENUTIL programs used in the pre- and post-processing of the aeroelastic simulations are discussed.

NASEXT

In this study, the tool NASEXT was solely used in the pre-processing of static aeroelastic analysis. The stiffness and mass matrices extracted from Nastran were converted into a so-called FLEX file, which is compatible with ENSOLV. Additionally, a NASEXT file was generated containing geometrical data of the structural model. The NASEXT file is required in the next pre-processing step in order to define correct coupling between structural and aerodynamic mesh.

SPLMOD

The working of the SPLMOD tool depends on the type of aeroelastic analyis. For static aeroelastic analysis, the fluid-structure interpolation matrix (called SPLINE file) was generated using the geometrical data of the aerodynamic and structural mesh.
In dynamic aeroelastic analysis, the structure is represented as a set of mode shapes determined by modal analysis. SPLMOD maps the generalized elasto-mechanical data onto the aerodynamic grid generating a DYNAMIC file. The process of generating the required input files for ENSOLV can be seen in figure 3.1.

3.2. SIMULATION CONDITIONS

Turbulence, anisotropy and non-uniform velocity profiles of inflow are parameters that greatly influence the flow field around the wind turbine. Prescription of simulation conditions should therefore be carefully defined.

3.2.1. SIMULATION SPACE AND REFERENCE FRAME

Partial Differential Equations require appropriate boundary conditions in order to be solved. These boundary conditions can be of physical or artificial nature. Situations in which they effect must be avoided. Far-field boundary conditions must be chosen sufficiently far from the wind turbine to prevent these effects from happening. Findings from earlier research report that too small flow domains could result into unstable or

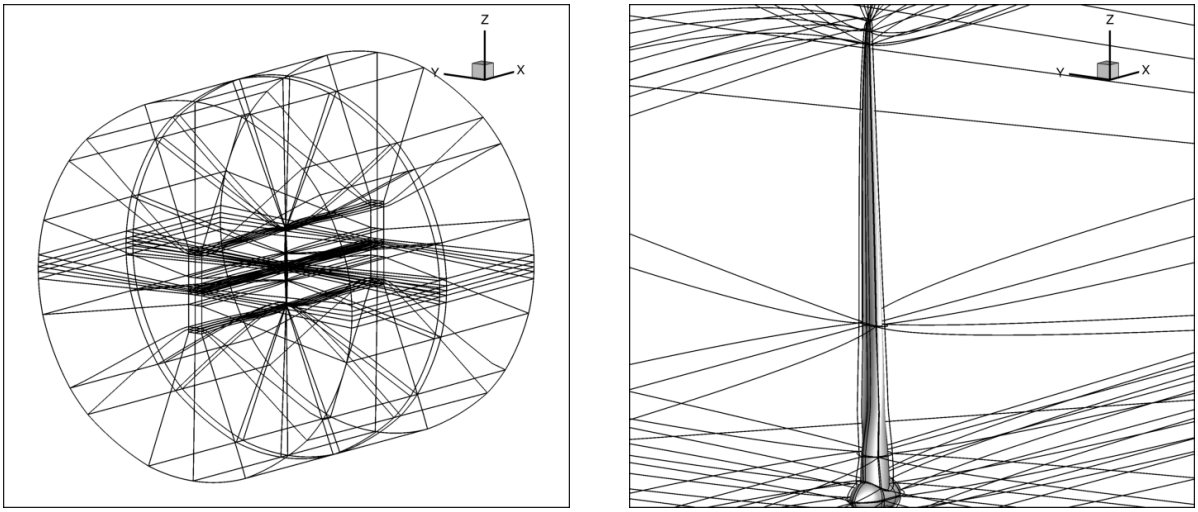

(a) Full simulation domain

(b) Close-up of the upper blade

Figure 3.2: The simulation space and body reference frame

diverging simulations (Stuurman, 2016).

The simulation domain is set to be a cylinder with a radius of five blade lengths, a distance of four blade lengths from the inlet to the blade and a distance of six blade lengths from the blade to the outlet. The dimensions of the flow domain are based on reference studies found in literature (Corson et al., 2012; Carrión et al., 2014; Stuurman, 2016). The simulation domain includes the full wind turbine rotor (two blades and a hub), because initially it was intended to apply atmospheric boundary layer flow. Besides, it would be easier to extend the simulation domain with a tower.

The coordinates of the initial geometry were defined in the body reference frame. The flow direction was set as the positive x-axis, the blade spanwise direction as the z-axis and the y-axis is perpendicular to the xz-plane. This led to a simulation domain ranging from x:(-440,660) meters, y:(-550,550) meters and z:(-550,550) meters. The simulation space including the body reference frame axis can be seen in figure 3.2.

3.2.2. BOUNDARY CONDITIONS

Far-field boundary conditions are necessary to bound the flow solution. As flow variable distributions at inlet and outlet are unknown, pressure-based boundary conditions based on the atmospheric pressure were chosen at the far-field boundaries. At the inlet a uniform velocity field is applied specifying the inflow speed.

Navier-Stokes wall conditions are imposed on the wind turbine rotor's surface. This means that the normal and tangential velocity components at the surface are kept zero and no heat transfer takes place, implying a no-slip, adiabatic wall. It was assumed that the flow over the surface is fully turbulent, hence no transition model was applied.

3.2.3. INFLOW CONDITIONS

As discussed in the literature review, geometrical nonlinearities become more prominent as structural displacements increase. Figure 3.3 and 3.4 show the design conditions of the studied wind turbine. The black dotted vertical lines indicate the test conditions that are considered (U_∞ = 7 m/s and U_∞ = 11.5 m/s). For U_∞ = 11.5 m/s the axial forces (shown in figure 3.3) are at a maximum, implying that the structural deformations will be largest. In figure 3.4), the pitch angle and rotational velocity are plotted against wind speed. The blade starts pitching, at U_∞ = 11.5 m/s, to avoid the onset of flow separation and mitigate large load fluctuations.

For ease, uniform, non-turbulent inflow is assumed, which should be sufficient to find an answer to the research question.

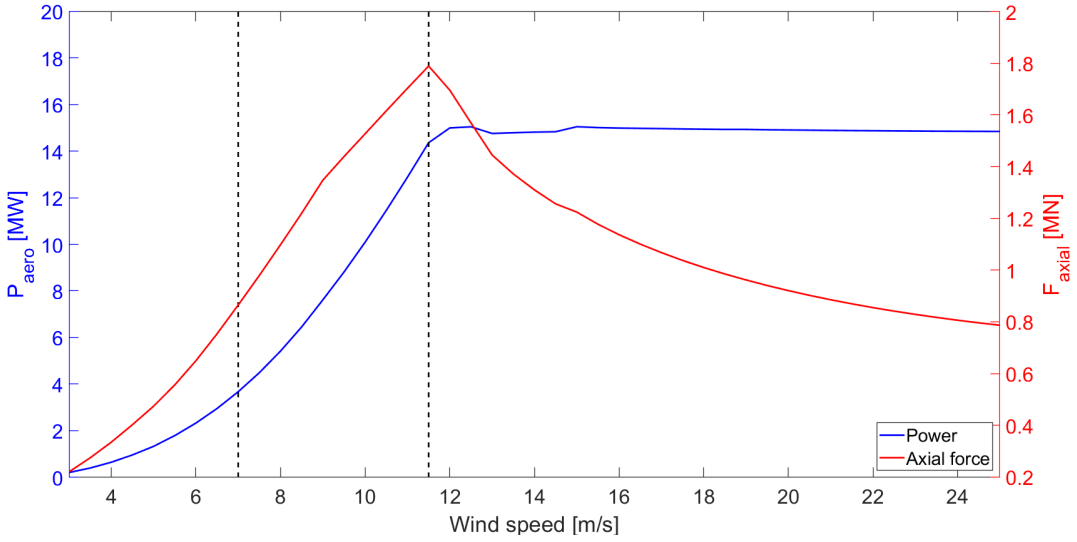

Figure 3.3: The power and axial force curve

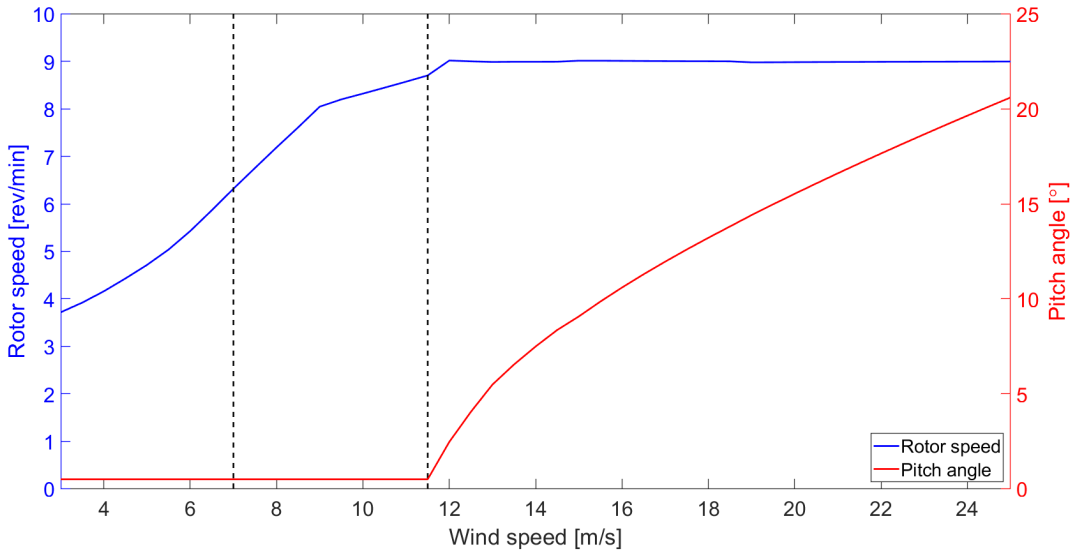

Figure 3.4: The design conditions of the wind turbine

3.3. SIMULATION METHODOLOGY

Aeroelastic analysis combines aerodynamic and structural models in order to solve the equations of motion. The system of equations is based on the reciprocal relation between aerodynamic forces and structural displacements. The one-degree-of-freedom system defined in the literature review can be extended to a three-dimensional system. The aeroelastic system can be expressed as follows:

$$[M^+]\ddot{\mathbf{x}}^+ + [C^+]\dot{\mathbf{x}}^+ + [K^+]\mathbf{x}^+ = q_\infty^+ S^+ \mathbf{C_A}(M_\infty, Re_\infty, \dot{\mathbf{x}}^+, \mathbf{x}^+) + \mathbf{B}^+ \tag{3.1}$$

Here $[M]$, $[C]$ and $[K]$ are the mass, damping and stiffness matrix, $\{\}^+$ denotes the variables have dimensions, $\mathbf{x}$ is the displacement vector, q_∞ is the freestream dynamic pressure, S is the aerodynamic reference area and $\mathbf{B}$ are the body forces (i.e. gravitational and inertial forces) and is expressed as follows:

$$\mathbf{B}^+ = [M](\mathbf{g} - \ddot{\mathbf{y}}) \tag{3.2}$$

Where $\mathbf{g}$ is the gravitational acceleration vector and $\ddot{\mathbf{y}}$ is the acceleration vector. From the literature review, it is known that the acceleration vector adds rotational terms to the equations of motion.
The aerodynamic force coefficient, $\mathbf{C_A}$, depends on the state of the structure and the flow parameters, e.g. Mach number and Reynolds number, and is expressed as follows:

$$\mathbf{C_A} = \frac{1}{L^{+2}_{struct}} \int_{S^+} p^+ / q_\infty^+ d\mathbf{S}^+ \tag{3.3}$$

Here p^+ represents the pressure. Viscous forces are omitted, since the skin friction is negligible relative to the pressure.

`ENSOLV` solves the non-dimensional form of the aeroelastic equations. Each variable in equation 3.1 is non-dimensionalized, using reference values defined in the input files. The substituted dimensionless variables are not given here, but can be found in the article written by (Prananta et al., 2000). Inserting the reference variables into the governing equations gives:

$$[M]\ddot{\mathbf{x}} + [C]\dot{\mathbf{x}} + [K]\mathbf{x} = \frac{1}{2} V^{\star 2} \mathbf{C_A} + \mathbf{B} \tag{3.4}$$

Here $V^\star$ is the speed index and is defined as follow:

$$V^\star = \frac{\overline{U}}{\sqrt{\mu}} \tag{3.5}$$

With the reduced velocity, $\overline{U}$, and mass ratio, μ, defined as:

$$\overline{U} = \frac{U_\infty^+}{\omega^+_{struct} L^+_{struct}}, \qquad \mu = \frac{m^+_{struct}}{\rho^+_\infty {L^+_{struct}}^3} \tag{3.6}$$

The speed index ensures the correct scaling between the structural model and fluid model.
The dimensionless aeroelastic equation stated above serves as starting point for the mathematical formulations for static and dynamic aeroelastic analysis. As stated earlier, the static analysis often contains large structural displacements, while dynamic analysis involves small time-dependent displacements. Hence, the total dynamic displacements can be decomposed in a mean and fluctuating part. The mean state of the deformed structure can be expressed as follows:

$$\mathbf{x_m} = \mathbf{x_{jig}} + \mathbf{h_{stc}} \tag{3.7}$$

Where $\mathbf{h_{stc}}$ is the deformation due to static aerodynamic loads. The static deformation is defined in physical coordinates to ensure an accurate description.
Dynamic aeroelastic analysis is restarted from the mean state, assuming the computed static state of the structure as initial condition. A perturbation of the equilibrium state can be applied to determine the corresponding aeroelastic response. The time-dependent displacements are defined as:

$$\mathbf{x}(t) = \mathbf{x_m} + \mathbf{x_{dyn}}(t) \tag{3.8}$$

Since the displacements are assumed relatively small, the structure is defined in terms of generalized coordinates employing a limited number of presumed modes.

3.3.1. SEMI-NONLINEAR AEROELASTIC ANALYSIS

The first analysis consisted of performing static aeroelastic simulation using the existing aeroelastic module of ENSOLV. As the structural model relies on the assumption of linearity, this method can be called a semi-nonlinear approach. The algorithm is fully-automated and implemented in the ENSOLV environment. Structural data must be readily available in the form of mass and stiffness matrices. The elasto-mechanical data of the structure was computed using Nastran and processed into the required file format using NASEXT and SPLMOD. A pre-stressed state of the blade was considered, taking into account stiffening effects due to centrifugal forces.
The equations of motion can be reformulated omitting the time-dependent terms from equation 3.3:

$$[K]^L \mathbf{x} = \frac{1}{2} V^{\star 2} \mathbf{C_A} \tag{3.9}$$

Where the $[\star]^L$ denotes the stiffness matrix is linear. Note that the body forces are omitted. It is known that the inclusion of rotational terms induces a centrifugal force on the structure. However, in linear static analysis, the forces are applied on the undeformed state of the structure, implying that the centrifugal forces would only have an elongating effect on the blade. Hence, they were neglected.
From the literature review, it was known that the spatial-coupling algorithm employed is computationally expensive. To avoid large computation times and an excessively large interpolation matrix, the 3D FEM model must be reduced or revised. It was chosen to use one of the available model reduction techniques in Nastran as it is the fastest and simplest method to obtain an equivalent structural model with less degrees of freedom. Guyan reduction (or static condensation) is a well-established and widespread used reduction method and is standard available in Nastran. This method decomposes the full structural model in so-called "active" and "deleted" nodes. It has been proven that it delivers an exact representation of the stiffness matrix and therefore is sufficient for static problems. As a drawback, the method exhibits an inaccurate representation of the mass matrix as it does not explicitly accounts for mass effects of omitted degrees of freedom. While the dynamic properties of the blade are expected to alter, it depends on the number and location of the "active" nodes to what extent. Although this drawback must be handled with care, it is expected that this drawback does not constitute problems in the dynamic analysis of current wind turbine blades as they are relatively stiff and light-weight.
The Guyan reduction can be expressed as follows:

$$\mathbf{x}_n = \begin{pmatrix} \mathbf{x}_a \\ \mathbf{x}_d \end{pmatrix} = [T]\mathbf{x}_a \tag{3.10}$$

Where $[T]$ is the transformation matrix, the subscript a denotes the active or "master" nodes and the subscript d denotes the deleted or "slave" nodes.
The original stiffness equation, $[K]^L\mathbf{x} = \mathbf{F}$ can be rewritten in the following form:

$$\begin{bmatrix} [K_{aa}] & [K_{ad}] \\ [K_{da}] & [K_{dd}] \end{bmatrix} \begin{pmatrix} \mathbf{x_a} \\ \mathbf{x_d} \end{pmatrix} = \begin{pmatrix} \mathbf{F_a} \\ \mathbf{F_d} \end{pmatrix} \tag{3.11}$$

Assuming that the forces in the slave nodes equal zero, equation 3.11 can be rewritten in terms of $\mathbf{x_a}$ only:

$$[K_{da}]\mathbf{x}_a + [K_{dd}]\mathbf{x_d} = 0 \tag{3.12a}$$

$$\mathbf{x}_d = -[K_{dd}]^{-1}[K_{da}]\mathbf{x}_a \tag{3.12b}$$

$$[K_{aa}]\mathbf{x_a} + [K_{ad}][K_{dd}]^{-1}[K_{da}]\mathbf{x}_a = \mathbf{F}_a \tag{3.12c}$$

The transformation matrix $[T]$ then becomes:

$$[T] = \begin{bmatrix} [I] \\ [t] \end{bmatrix} = \begin{bmatrix} [I] \\ -[K_{dd}]^{-1}[K_{da}] \end{bmatrix} \tag{3.13}$$

Since the energy of the system must be conserved, the new stiffness and mass matrices can be written as follows:

$$[K^G]^L = [T]^T[K]^L[T] \tag{3.14a}$$

$$[M^G] = [T]^T[M][T] \tag{3.14b}$$

Where the superscript G denotes the Guyan reduced matrices.

As follows, the reduced matrices are processed by NASEXT and SPLMOD in order to generate the required input files for the static aeroelastic analysis. The new formulation of the governing equations is expressed as follows:

$$[K^G]^L \mathbf{x} = \frac{1}{2} V^{\star 2} \mathbf{C_A} \tag{3.15}$$

Since RANS accounts for nonlinear flow effects, an iterative scheme must be adopted to solve the equation stated directly above. The iterative scheme can be expressed as follows:

$$\mathbf{h_{stc}}^{k+1} = (1-\omega)\mathbf{h_{stc}}^{k} + \omega [K^G]^{L^{-1}} \left[\frac{1}{2} V^{\star 2} \mathbf{C_A}(\mathbf{x_m^k}) \right] \tag{3.16}$$

Where $\mathbf{h_{stc}}$ are the static displacements, ω is a relaxation factor, k is the iteration counter and $\mathbf{x_m^k}$ represents the deformed state of the structure at the k-th iteration.
Note that equation 3.16 is solved at the structural mesh, the aerodynamic coefficient is interpolated from the deformed aerodynamic mesh to the structure to define the load on the structure. Subsequently, equation 3.16 is solved and the displacements are interpolated to the aerodynamic grid, after which the mesh is deformed using the mesh-deformation algorithm. This process is repeated until the equilibrium state is reached, resulting in the final linear deformed geometry, $\mathbf{x_m}^L$, and corresponding aerodynamic loads, $\mathbf{C_A}(\mathbf{x_m}^L)$.

3.3.2. FULLY-NONLINEAR AEROELASTIC ANALYSIS

The second approach comprises the existing aeroelastic framework of ENSOLV modified by the implementation of the nonlinear structural solver of Nastran, which realizes a fully-nonlinear approach. Currently, the FSI iterations must be performed manually. The structural deformations are solved in the Nastran environment using the nonlinear solver and the aerodynamic loads are computed in ENSOLV using the steady solver. Data transfer between both models is executed SPLMOD. In order to speed up the convergence process, the aerodynamic loads from the linear computed steady-state are applied to the structure. Remember that these forces were applied in the "active" nodes. Although the forces can be directly applied to the full structural model, it was chosen to interpolate them to the entire set of structural nodes to avoid odd local deformations.

In linear statics, the force-displacement relation is linear as shown in equation 3.9. Taking $\mathbf{F} = \frac{1}{2} V^{\star 2} \mathbf{C_A}$, a more general expression for the relation can be defined:

$$[K]^L \mathbf{x} = \mathbf{F} \tag{3.17}$$

This linear relation implies that the displacements are in similar direction as the forces. Additionally, the linear stiffness matrix only depends on the linear material properties and the undeformed structure. The fully-nonlinear aeroelastic approach aims to be capable of computing large displacements that involve nonlinear structural phenomena. These nonlinearities primarily consist of two aspects: stiffening effects due to initial displacements and stresses, and follower-force effects. Therefore, the linear stiffness matrix must be modified. Firstly, geometrical effects are included into the expression of the stiffness matrix. The force-displacement relationship can be rewritten as follows:

$$\mathbf{F} = [K](u)\mathbf{x} = \mathbf{F} = \{[K]^L + [K]^d\}\mathbf{x} \tag{3.18}$$

Here $[K]^d$ is the differential stiffness matrix, which depends on the deformation of the structure. In turn, the deformed state depends on the forces. Follower-forces are forces, of which the definition depends on the displacements of the structure on which they act. The most-often quoted example of such forces may be the surface pressure, where the force on the surface depends on the surface area and its orientation (Hibbit, 1979). This means that the force vector changes upon deformations. An additional follower-force stiffness must be added to the formulation of the stiffness matrix, resulting in:

$$[K]^t = [K]^L + [K]^d + [K]^f \tag{3.19}$$

Lastly, the follower-forces must be added to the equation. Since aerodynamic forces were computed around the deformed geometry, they are not set to change. The rotational forces, neglected in the semi-nonlinear

approach, have to be added as they depend on the deformation of the structure. The force-displacement relation then becomes:

$$\mathbf{F} + \mathbf{F_{cent}} = [K]^t \mathbf{x} \tag{3.20}$$

The solution approach in `Nastran` utilizes an iterative procedure based on the modified Newton-Raphson method. It differentiates itself from the previous method by updating the structure each iteration. As such, the change of the stiffness property and loads due to deformations are accounted for. In each iteration, an incremental load **P** is applied to the structure. Due to the change in geometry, the incremental load and the element force vector $\mathbf{F}^i$ are not equal, leading to a residual error. A number of iterations must be performed on the particular load level until the residual error is reduced below the specified convergence criterion. This can be expressed as follows:

$$(\mathbf{F}^i + \mathbf{F^i_{cent}}) - P = \mathbf{R}^n \rightarrow \mathbf{0} \tag{3.21}$$

Figure 3.5 shows this iterative process schematically. The total load on the structure is applied in incremental steps solving for an interim solution. The predictor-corrector scheme ensures convergence at each incremental load, marching to a final converged solution.

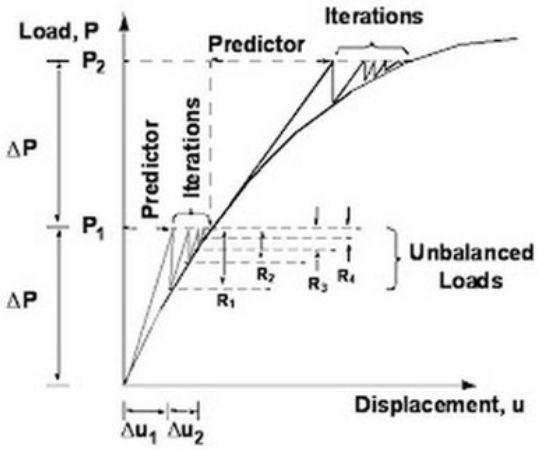

Figure 3.5: Nonlinear solution strategy in `Nastran` (Aerospace Engineering - Training, 2016)

After the solution was converged, the structural displacements from the earlier defined support points can be extracted and interpolated to the aerodynamic model to deform the mesh. Subsequently, a steady CFD solve was performed, which in turn provided the static aerodynamic load around the newly-deformed shape. This process can be repeated until the steady-state solution has reached certain convergence criteria resulting in the final nonlinear deformed geometry, $\mathbf{x_m}^{NL}$, and corresponding flow solution, $C_A(\mathbf{x_m}^{NL})$.

3.3.3. MODAL ANALYSIS

The dynamic aeroelastic analysis is restarted from the steady-state solution. As the displacements associated to dynamic aeroelastic problems are small, the structure can be defined in terms of a parametric space spanned by a finite number of mode shapes. The time-dependent displacements can be expressed as follows:

$$\mathbf{x}_{dyn}(t) = \phi_\mathbf{1} q_1(t) + \phi_\mathbf{2} q_2(t) + \ddots + \phi_\mathbf{N} q_N(t) \tag{3.22}$$

Where ϕ_i is the i-th mode shape and q_i is the i-th generalized coordinate.
The mode shapes must be selected such that they accurately represent the motion of the structure. It was therefore chosen to use the natural mode shapes of the structure. Two flutter analyses are performed: the first using the linear mode shapes and the second using the nonlinear mode shapes. In general, the eigenmodes can be calculated by solving the following eigenvalue problem:

$$\left[\omega_L^2 [M] - [K]^L\right]\phi_\mathbf{L} = 0 \tag{3.23}$$

Where $\phi_\mathbf{L}$ are the "linear" computed natural mode shapes and ω_L the corresponding modal frequencies.
Similar as in the semi-nonlinear static aeroelastic approach, the pre-stresses stiffness matrix is used to compute the eigenmodes. The tensile stresses due to the centrifugal force act as stiffener, leading to higher eigenfrequencies. The eigenvalue problem can be expressed as follows:

$$\left[\omega_L^2 [M] - ([K]^L + [K]^{cent})\right]\phi_\mathbf{L} = 0 \tag{3.24}$$

Where $[K]^{cent}$ suggests the stiffening effect.
In order to compute the "nonlinear" mode shapes, the similar eigenvalue problem is solved, however the nonlinear stiffness matrix computed by the fully-nonlinear aeroelastic approach is used. The eigenvalue problem can be expressed as follows:

$$\left[\omega_{NL}^2 [M] - [K]^T\right]\phi_\mathbf{NL} = 0 \tag{3.25}$$

Where $\phi_{\mathbf{NL}}$ are the "nonlinear" computed natural mode shapes and ω_{NL} the corresponding modal frequencies.
The mode shapes were normalized with their largest component in order for the mode shapes to be of similar magnitude. This is required for flutter analysis.

3.3.4. FLUTTER ANALYSIS

Flutter is the diverging oscillatory motion of a structure that is self-exciting due to changing flow conditions. It is of paramount importance to predict this type of instability as it will exponentially increase until catastrophic failure occurs. Flutter analysis intends to find the flutter boundary. At this boundary, the structure will adopt a self-sustained, constant-amplitude oscillation. Exceeding the flutter boundary leads to diverging motion, while remaining within the boundaries signifies damped motion. In this thesis, the p-k method was used to perform the flutter analysis. Since flutter occurs when the structure is in harmonic motion, this method assumes that the aerodynamic loads are also harmonic. This assumption is only accurate in close proximity of the flutter boundary (Gu and Yang, 2012). As in most flutter analysis methods, the structure is defined in terms of a set of mode shapes, which are computed using the modal analysis. This indicates that the structure is linearized around the deformed state of the blade, comprising a semi-linearized method. The motion of the structure can be expressed as superposition of a set of mode shapes:

$$\mathbf{x_{dyn}}(t) = \phi_{\mathbf{1}} q_1(t) + \phi_{\mathbf{2}} q_2(t) + \cdots + \phi_{\mathbf{N}} q_N(t) \tag{3.26}$$

For a set of N mode shapes.
Substituting these modes in the equations of motion and multiplying with ϕ_i^T lead to the uncoupled set of generalized equations of motions:

$$[\hat{M}]\ddot{q} + [\hat{C}]\dot{q} + [\hat{K}]q = \frac{1}{2}V^{\star 2} C_{Q_i} + B_i \tag{3.27}$$

Here the $\hat{[]}$ indicates that a matrix is generalized, leading to $[\hat{M}]$, $[\hat{C}]$ and $[\hat{K}]$ being the modal mass, damping and stiffness matrix respectively. C_{Q_i} are the generalized aerodynamic forces, that can be expresses as follows:

$$C_{Q_i} = \int_{S^+} \frac{p^+}{q_\infty} \phi_i^T \cdot \mathbf{n} dS^+ \tag{3.28}$$

P-K METHOD

The flutter equations, in p-k form, can be expressed as follows:

$$\left[V^2/c^2[\hat{M}]p^2 + V/c[\hat{C}] + [\hat{K}] - \frac{1}{2}\rho V^2[\hat{A}(ik)]\right]\mathbf{q} = 0 \tag{3.29}$$

Here $A(ik)$ is the complex aerodynamic matrix, $\hat{\{\}}$ indicates that the matrix or vector is generalized and p are the complex roots of the nonlinear eigenvalue problem: $p = \gamma k \pm ik$. Here $k = \frac{\omega c}{2V}$ is the reduced frequency and γ is the rate-of-decay. Since harmonic motion is assumed, the aerodynamic matrices are independent of γ.
As all matrices are real-valued, except for the aerodynamic matrix. The above equation can be simplified by decomposing the aerodynamic matrix into a real and imaginary part:

$$A(ik) = A^R(k) + iA^I(k) \tag{3.30}$$

The entries of the aerodynamic matrices, $A^R(k)$ and $A^I(k)$, constitute the Aerodynamic Influence Coefficients (AIC's), where the real-valued matrix contains the modal aerodynamic stiffness coefficients and the imaginary-valued matrix the modal aerodynamic damping coefficients. After substituting the above expression in the flutter equation, it becomes:

$$\left[V^2/c^2[\hat{M}]p^2 + V/c[\hat{C}] - \frac{1}{2}\rho V^2\frac{[A^i(k)]}{k}p + [\hat{K}] - \frac{1}{2}\rho V^2[A^R(k)]\right]\mathbf{q} = 0 \tag{3.31}$$

The flutter equations can be written in its final state-space form (Rodden and Johnson, 1994):

$$([A] - p[I])\{\overline{u_h}\} = 0 \tag{3.32}$$

where $\overline{u_h}$ includes the modal displacements and velocities and $[A]$ is a real matrix:

$$[A] = \left[\begin{array}{c|c} 0 & I \\ \hline -[\hat{M}]^{-1}\left([\hat{K}] - \frac{1}{2}\rho V^2 Q^R(k)\right) & -[\hat{M}]^{-1}\left([\hat{C}] - \frac{1}{4}\rho c V (Q^I(k)/k)\right) \end{array}\right] \tag{3.33}$$

By means of a process called determinant iteration, the flutter equations are solved at different inflow velocities V for complex roots p associated with the modes of interest. The iterative process is completed mode by mode for one speed and then at successive pre-selected inflow speeds (Hassig, 1971). The initial trials of the complex roots are defined as:

$$p_1 = \delta_1 + i k_1, \qquad p_2 = \delta_2 + i k_2 \tag{3.34}$$

Whereby the aerodynamic matrices $A(k_1)$ and $A(k_2)$ are interpolated from the available aerodynamic matrices. This process is repeated using the Regula-Falsi method until a previously defined degree of convergence is reached.

$$p_{i+2} = \frac{(p_{i+1}F_i - p_i F_{i+1})}{(F_i - F_{i+1})} \tag{3.35}$$

The converged value for the complex root, $p_c = \delta_c + i k_c$,is used to determine the frequency and damping of the specific mode:

$$f = \frac{V k_c}{2\pi c}, \qquad g = 2\gamma = \frac{1}{\pi} ln \frac{a_{n+1}}{a_n} = 2\frac{\delta_c}{k_c} \tag{3.36}$$

COMPUTING THE AIC'S

Computation of the AIC's is essential for flutter analysis. The AIC's must be given for a sufficient number of k values. As shown in literature review, the classical form of wind turbine flutter entails coupling of the first torsional mode with one of the flapwise modes. As will be shown in the results given in chapter 5, the sixth mode (from the linear set of mode shapes) and the eighth mode (from the nonlinear set of mode shapes) represent the first torsional mode. It was therefore decided to include the first eighth mode shapes in the analysis. The unsteady CFD simulations were carried out in `ENSOLV`, in which multiple simulations were performed similar to structural vibration analysis. The statically deformed blade was used as initial condition. At this condition, the initial displacement, velocity and acceleration are zero. The imposed harmonic motion started from the initial state and can be expressed as follows:

$$\mathbf{x_{dyn}}(t) = a\phi_\mathbf{i} \sin \frac{kV}{c} t \tag{3.37}$$

Here $\phi_\mathbf{i}$ is the mode that is excited, a is an amplitude constant, V is the reference velocity, c is the reference length and k is the reduced velocity defined in `ENSOLV` as follows: $k = \frac{\omega c}{V}$. Where ω is the circular frequency in rad/s.

The generalized aerodynamic forces (GAF's) were derived by mapping the integrated pressures onto the separate mode shapes and recording the time response. The GAF's can be expressed as follows:

$$GAF_{ij} = \int_{S^+} \frac{p^+}{q_\infty^+} \phi_j^T \cdot \mathbf{n} dS^+ \tag{3.38}$$

Where i denotes the mode that is excited and j the mode shape in which the aerodynamic forces are mapped. It is essential for the accuracy of the analysis that the GAF's converge to a periodic response. As the p-k method is in frequency-domain, the time-dependent GAF's must be converted into frequency-domain. The built-in Fast-Fourier Transform (FFT) function `FFT` in `Matlab` was employed to perform that operation. The Discrete Fourier Transorm (DFT) transforms a sequence of equally-spaced samples of a function (in this case the GAF) into a same-length sequence of equally spaced samples of the Discrete-Time Fourier Transform (DTFT), which is a complex-valued function of frequency. The DFT can be found in every textbook of vibrational analysis and can be expressed as follows:

$$X_k = \sum_{n=0}^{N-1} x_n \exp -i \frac{2\pi k n}{N} \tag{3.39}$$

Here k denotes the number of the frequency bin, N is the number of samples and k is the sample frequency. Because the imposed sinusoidal motion of the structure assumes constant amplitude and reduced frequency,

the aerodynamic response can only be obtained for a single reduced frequency. Therefore, merely the complex number of the first frequency bin is considered to determine the AIC's. The AIC's are computed by dividing the FFT of the particular GAF by the FFT of the imposed motion. The derivation of the AIC's is as follows:

$$A(ik) = \begin{bmatrix} A_{11}(ik) & A_{12}(ik) & \dots & A_{1n}(ik) \\ A_{21}(ik) & A_{22}(ik) & \dots & A_{2n}(ik) \\ \vdots & \vdots & \ddots & \vdots \\ A_{d1}(ik) & A_{d2}(ik) & \dots & A_{dn}(ik) \end{bmatrix} \tag{3.40}$$

And so:

$$A^R(k) = real(A(ik)), \quad A^I(k) = imag(A(ik)) \tag{3.41}$$

It was chosen to use the data from the last vibration period to compute the AIC's in order to ensure good convergence. For the p-k method it is required to extrapolate the AIC's to $k = 0$ in order to complete the aerodynamic matrices.

3.3.5. ANALYSIS SET-UP

The set of analyses that were performed in this work, required communication and data transfer between different software modules. At the beginning of this chapter, a concise overview of the utilized software packages was given. In this section, a clear representation of the mutual interactions and processes between the variety of software modules is given. As may noticed, `ENSOLV` functioned as the core of the solution methodology, while various in-house tools and packages performed the pre- or post-processing steps needed to enable the performed simulation. Figure 3.6 summarizes the entire analysis set-up.

Pre-processing of the static aeroelastic analysis can be decomposed in two main operational processes: generating the aerodynamic grid and generating input files that involve the FSI coupling. A concise impression of the mesh-generation process is depicted for completeness, but will be discussed in more detail in chapter 4. As mentioned earlier in this chapter, the elasto-mechanical data must be readily available prior to the analysis. Special DMAP macros developed at NLR enable extraction of the stiffness and mass matrix from modal analysis (SOL103), after which `NASEXT` and `SPLMOD` convert the data into desirable formats. The aerodynamic grid, prescription of the boundary conditions and flow conditions, and the files containing the interpolation matrix and structural matrices served as input to `ENSOLV`, after which the static aeroelastic analysis can be started. `ENSOLV` utilizes a fully-automated approach to solve the equations of motion.

With regard to saving time and work, the fully-nonlinear aeroelastic approach was restarted from the semi-nonlinear solution. This simulation approach is not yet automated, causing it to be quite labour-intensive. The steady-state solution of both static analyses served as initial condition for the flutter analyses. Linear and nonlinear pre-stressed mode shapes are computed and imported into `ENSOLV` to excite the blade. Both flutter analyses contained 64 unsteady CFD simulations, exciting eight separate mode shapes at eight successive reduced values. Since no parallel computation could be performed, it is decided to execute four simulations sequentially per node (including eight processors), which allowed the performance of a full flutter analysis at once. The aerodynamic response data was exported to the `Matlab` environment so it can be processed further. A correction model is applied to filter still-existing transient effects, after which the AIC's were computed. The AIC's and generalized elasto-mechanical data obtained from modal analysis were imported, after which the nonlinear eigenvalue problem was solved. The damping and frequency characteristics of the blade mode were saved and plotted to create frequency- and damping plots of the blade.

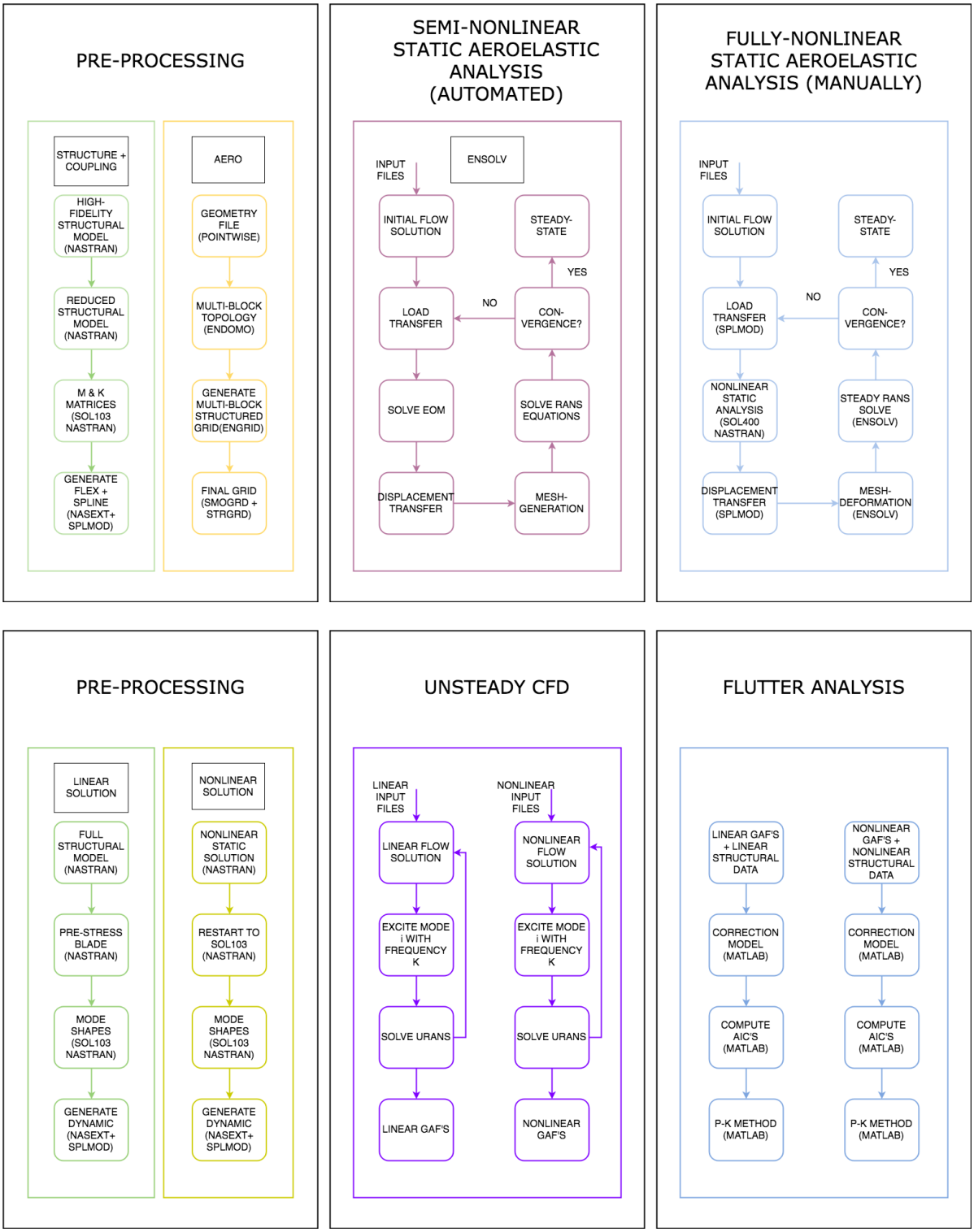

Figure 3.6: Overview of the entire analysis set-up

4

MODELS

The sub models incorporated in the aeroelastic framework are discussed in this chapter. First, the geometrical and structural characteristics of the analysed wind turbine blade used in this study are presented in section 4.1. In section 4.2, the process of mesh-generation of the blade is explained and the results of the subsequent grid-convergence study are discussed. The coupling models involved in the analysis methodology are presented in section 4.3. Finally, the fluid and structural model are verified for a number of test cases.

4.1. WIND TURBINE BLADE

4.1.1. BLADE'S GEOMETRY

The wind turbine blade used in this study is a theoretical blade, designed by a Dutch blade design company, called *We4Ce*. It originated from one of its earlier blade designs by upscaling and is modified using the integral wind turbine design tool FOCUS. The 220 meters-diameter, two-bladed, clock-wise rotating, pitch-regulated turbine has a power rating of 15 MegaWatt (MW) and contains individual pitch control. The blades are twisted and contain a variety of airfoil types over the span to optimize its performance. In figure 4.1, the geometry of the blade is shown, where the different colors indicate airfoils with a varying thickness-to-chord ratio ($t/c = 0.8$ at the root and $t/c = 0.18$ at the tip). Wind turbine blades have similar requirements as to airplane wings. In general, the cross-sectional shapes are chosen to obtain the best lift-to-drag characteristics. As the surface area contributes greatly to unwanted drag, these shapes are fairly thin. However, wind turbine blade design also depends on structural requirement, which means that the blade must become thicker towards the root. In order to meet the structural requirements at the inboard part of the blade without using "fat" shapes airfoils, blunt-trailing edge airfoils are incorporated in the blade design. Besides providing good structural characteristics, these cross-sectional shapes lead to reduction of sensitivity to soiling (Mertes et al., 2011). The sections in the middle and outboard regions of the blade consist of conventional (sharp trailing edge) airfoils. The exact type of airfoils are not given due to confidentiality reasons.

The twist distribution and planform shape of the blade are also determined to optimize the aerodynamic performance. It is evident that the optimization of these design parameters is also constrained to structural and manufacturing issues. From figure 4.2, it can be observed that the twist distribution can be subdivided in three regions: the inboard, the outboard and the tip region. As the relative wind speed is higher at the tip, the apparent wind angle relative to the rotor is greater. Hence, the twist decreases constantly over largest part of the blade. At the tip, the twist increases to alleviate tip loads. Additionally, large twist angles appear at the inboard part of the wind turbine blade. In this area, transition occurs from a cylindrical shape towards the blunt trailing-edge airfoil shapes. The blade is heavily twisted in that region to avoid excessive flow separation, which could lead to undesired drag.

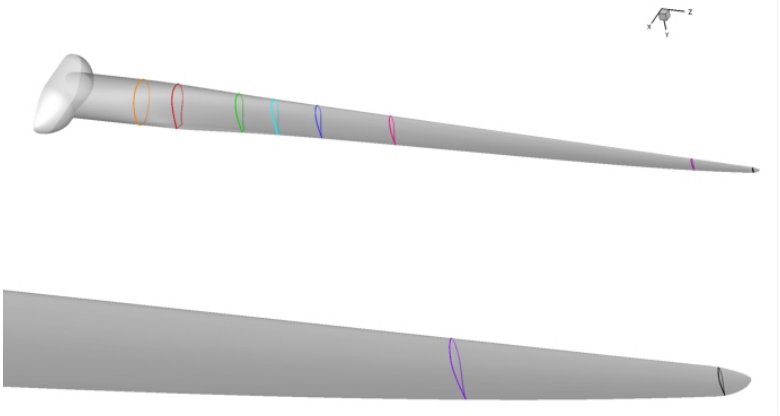

Figure 4.1: The blade geometry with the different airfoil profiles highlighted

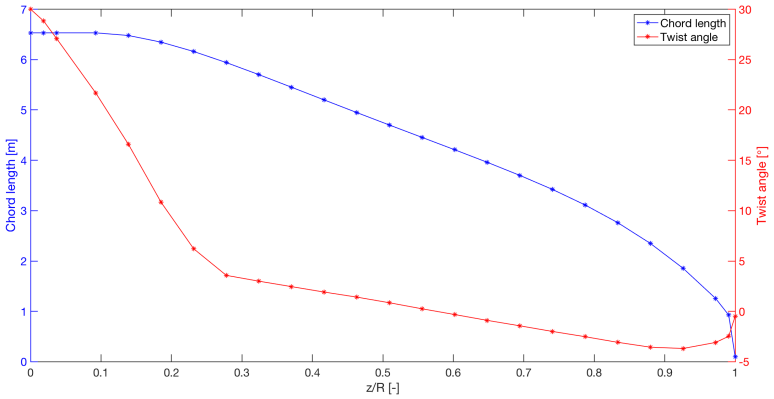

Figure 4.2: The chord and twist distribution of the blade (the y-axis is multi-functional and the units of the axis are listed in the legend)

4.1.2. BLADE STRUCTURAL PROPERTIES

Structural blade design is driven to maintain its structural integrity and avoid material failure, while keeping its weight low and minimize material usage. Additionally, structural design has evolved towards smarter blade design that can adapt their shape to the wind conditions. The most prominent example is the inclusion of bending-torsion coupling in the blade to adapt the effective incidence angles to the wind (Fedorov and Berggreen, 2014).

As shown in the aerodynamic design, thick cross-sectional shapes are integrated in the design to provide good structural properties. *We4Ce* also provided the structural model of the blade, which was generated by FOCUS. This integrated wind turbine design tool has the capability of generating 3D FEM models from equivalent beam models that are used in low-fidelity aeroelastic analysis. The sectional stiffness's of the equivalent beam model are shown in figure 4.3. Evidently, the inboard region of the blade has the highest stiffness, since the cross-sectional shapes are largest. The cross-coupling stiffness defines the degree of coupling between flapwise bending moment and deformations in edgewise direction. The positive cross-coupling stiffness indicates that downwind flapwise moment results in a deformation in-plane in the direction of the leading edge.

4.1.3. BLADE EIGENMODES

From now on, only the 3D FEM model is considered. A modal analysis was carried out to obtain a better understanding of the dynamic characteristics of the blade. The literature review has showed centrifugal forces impact dynamic behavior of rotating structures by an increase in natural frequency. Consequently, the eigenmodes of the blade were determined for an unloaded and a pre-stressed condition. The pre-stressed condition considered the stiffening effect corresponding to the angular velocity of load case 1: $\Omega = 8.7$ rev/min. The results are shown in table 4.1.

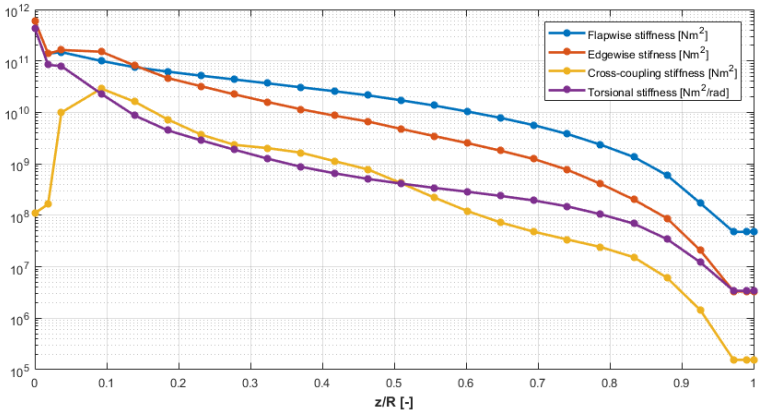

Figure 4.3: Cross-sectional stiffness's over the blade (the y-axis is multi-functional and the units of the axis are listed in the legend)

Mode number	Unloaded state [Hz]	Pre-stressed state [Hz]	Mode shape
1	0.486	0.525	1st flapwise bending
2	0.725	0.732	1st edgewise bending
3	1.300	1.348	2nd flapwise bending
4	2.162	2.191	2nd edgewise bending
5	2.619	2.675	mixed bending
6	4.161	4.219	1st torsional
7	4.260	4.346	mixed bending
8	4.571	4.704	mixed bending

Table 4.1: The eigenmodes computed for the unloaded and pre-stressed state of the wind turbine blade

The computed eigenfrequencies confirm that centrifugal forces stiffen the blade. This implies that dynamic behavior of structures depends on speed of rotation. As a result, it is essential to take into account stiffening effects in the aeroelastic analysis of a rotating structure.
In order to get a better understanding about the shape of the modes, a frequency response analysis is carried out in `Nastran`. Firstly, an external sinusoidal force of $100N$ in flapwise direction is applied at the tip for a certain frequency range. Secondly, the same loading is applied in edgewise direction. Both frequency responses are depicted in figure 4.4. The red-dotted lines represent the frequencies of the blade's modes. It is expected that the tip displacements are amplified at the natural frequencies of the blade.
The results clearly show that the first and third mode are flapwise bending modes, while the second is an edgewise bending mode. For the other mode shapes, the response is more complicated, which indicates a mixing of vibrational directions. With the aid of mode visualization, see appendix E, the type of modes can be determined. It follows that the sixth mode shape represent the first torsional mode, and the fifth, seventh and eighth mode are "mixed" bending modes as there is no dominant vibration direction perceptible.

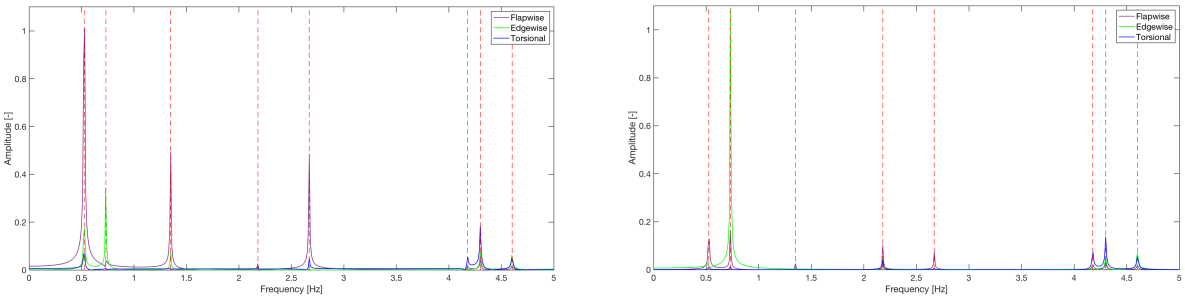

(a) Force frequency response for sinusiodal load out-of-plane

(b) Force frequency response for sinusiodal load in-plane

Figure 4.4: Force frequency responses for sinusiodal loads with a frequency between $f = 0Hz$ and $f = 5Hz$

4.2. MESH DEVELOPMENT

Prior to this study, no CFD analysis was performed of this blade yet, hence a new mesh had to be developed. As mentioned in chapter 3, ENSOLV is part of the ENFLOW environment, which consists of the following modules (Kok, 2019):

- ENSOLV: The fluid solver.
- ENDOMO: The domain modeler.
- ENGRID: The grid generator.
- ENADAP: The grid adaptor.

ENDOMO and ENGRID are used to generate the multi-block structured grid required for CFD analysis in ENSOLV. ENADAP can be used to improve the multi-block grid by using an initial flow solution, but was not used in this study.

4.2.1. MESH STRUCTURE

For most wind turbine applications, a body-fitted approach is used in mesh generation. In general, three types of meshes can be distinguished in this approach: the structured mesh, the unstructured mesh and the hybrid mesh (see figure 4.5). The difficulty and computational costs of generating body-fitted meshes to complex geometries is of concern in the analysis of wind turbines. Unstructured meshing methods simplify the process, because tetrahedral cells are used instead of orthogonal hexahedral cells. However as unstructured meshes are based on arbitrary relations, they require memory to store the inter-connectivity relations. Structured meshes, on the other hand, are better capable of capturing the boundary layer correctly, because the are aligned with the local streamlines. The major drawback is the difficulty to handle complex geometries. Hybrid meshes blend both mesh strategies, combining best of two worlds.

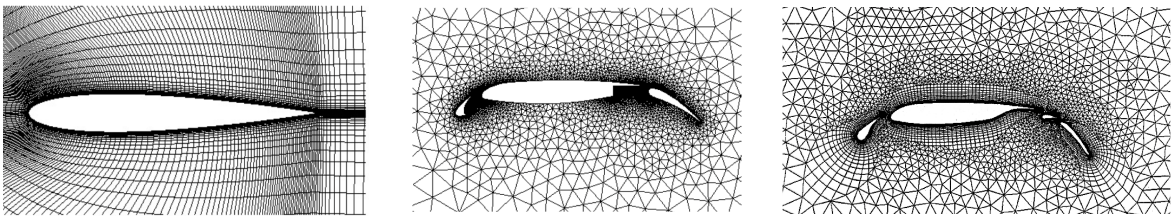

(a) Structured mesh (b) Unstructured mesh (c) Hybrid mesh

Figure 4.5: Three types of aerodynamic meshes

Multi-block grids alleviate the difficulty of generating structured grids around complex geometries. Besides, they provide the opportunity to run simulations in parallel on multi-processor computing systems, solving flow problems more efficiently. ENSOLV computes two- or three-dimensional flow solutions on multi-block structured grids. As shown earlier, the ENFLOW environment contains in-house developed modules for generating multi-block grids. The mesh-generation process consists of three steps. First, ENDOMO is used to create the block-topology description around the imported CAD model. The flow domain is bounded defining appropriate far-field conditions. As follows, the topology is imported into ENGRID, after which structured grids are created. And finally, two in-house codes are used to smooth the grid and obtain boundary layer resolution adjacent to the surface of the object.

4.2.2. MESHING PROCEDURE

SURFACE GEOMETRY

In order to create the multi-block topology around the wind turbine rotor, the geometry must be imported in ENDOMO. The Computer-Aided Design (CAD) geometry including a single blade is provided by *We4Ce*. Most file formats for CAD designs can not be directly imported into ENDOMO. As ENDOMO is compatible with segment files, commercial mesh-generation software was used to convert the CAD model into a segment file. An iterative approach is used to generate an identical geometry in ENDOMO.
First, the CAD model (using IGES) is imported into Pointwise. Discrete curves were drawn over the span of the consisting of cross-sectional segments. Four additional discrete curves were created to that connected

the spanwise segments. Subsequently, the set of discrete curves were exported and converted into the required format to be imported in ENDOMO. In ENDOMO, the initial blade geometry was created by the generation of discrete surfaces. The initial surface description was, in turn, transferred back into Pointwise, where the points of geometry were projected onto the CAD model. After several iteration steps, all points of the discrete surfaces were located on the actual geometry. Copying and rotating the final blade geometry led to two blades.

HUB MODELLING

Currently, the CAD model merely contained the blade geometry. As the full rotor was analysed in this work, the hub must be devised. The geometry of the hub is based on the design of Enercon E-126 wind turbines shown in figure 4.6). The Enercon E-126 is characterized by its groundbreaking gearless drive concept, which distinguishes itself with its unique streamlined hub and housing (Enercon GmbH, 2016). It was attempted to approach the shape in ENDOMO for a 2-meter hub radius. The hub and the blades are blended into one piece using Pointwise, after which the final geometry was imported into ENDOMO.

Figure 4.6: Visualization of the hub geometry of the Enercon E-126 (Enercon GmbH, 2016)

MULTI-BLOCK TOPOLOGY

It was chosen to adopt an O-type grid around the blade as the implementation was simple and straightforward. In order to create the O-grid, the geometry of the blade is decomposed in multiple faces, shown in figure 4.7a. Blocks adjacent to the surface can be semi-automatically generated. These so-called Navier-Stokes blocks are useful to obtain good resolution near the wall in order to capture the boundary layer accurately. As the outer boundaries of the flow domain represent a cylinder, it was decided to connect the Navier-Stokes blocks and outer boundaries using a H-type topology. Figure 4.7b and 4.7c show the entire multi-block topology used to create the mesh.

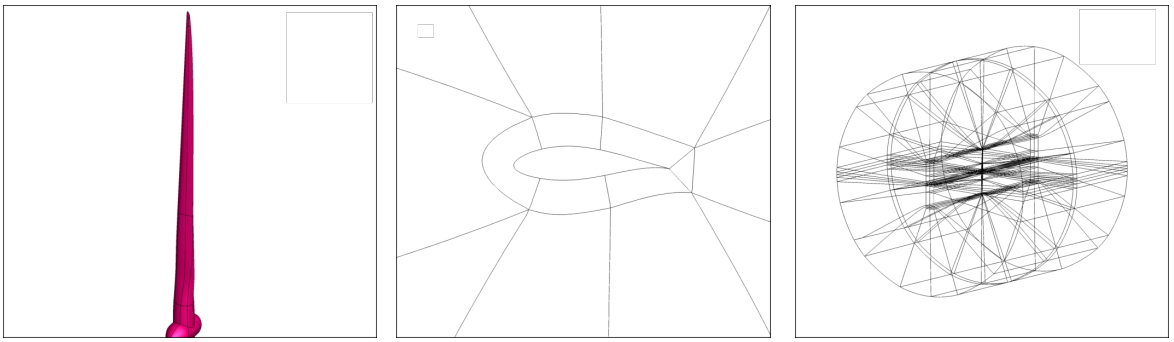

(a) The face topology on the surface of the blade (b) O-grid around a cross-section of the blade (c) The full multi-block topology

Figure 4.7: An overview of the topology in different layers of the aerodynamic mesh

4.2.3. GRID GENERATION

ENGRID was used to generate the aerodynamic mesh using the multi-block topology. Each block in the multi-block topology contains an orthogonal grid, where the grid cells are defined in i, j and k direction. The grid-generation process commenced by defining the number of grid points on the edges. Because of orthogonality, ENGRID automatically defined the grid dimensions of opposing edges. The distributions of the points on the edges were adapted to obtain smooth transition over block boundaries. Additionally, grid distributions of high-curved surface regions were modified in order to capture large gradients of flow variables. After realizing a reasonable good aerodynamic mesh, the grid is smoothed with the in-house tool SMOGRD. The smoothing tool, based on the biharmonic equations, increases the grid quality automatically, which reduces the time

required for obtaining a well-working grid. The tool adapts the grid distribution at block boundaries, but also computes a modified position of those boundaries. In other words, the tool works across block boundaries, which makes it very efficiently.

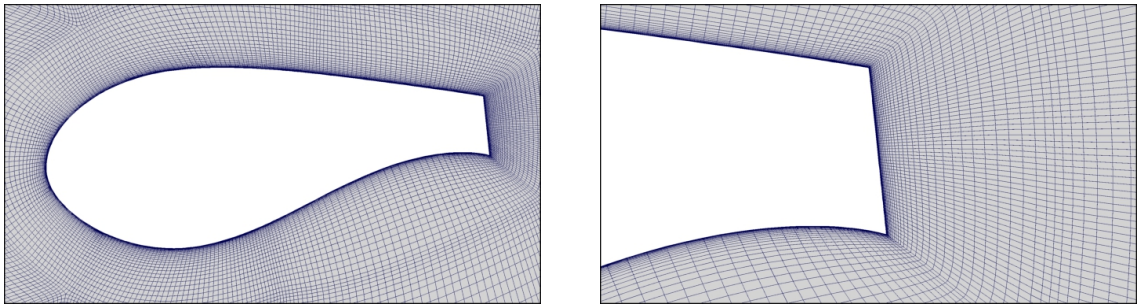

(a) The O-grid

(b) Close-up of the trailing edge

Figure 4.8: Fine grid resolution in the boundary layer at $z/R = 0.26$

4.2.4. Y+ VALUE

Boundary layer modelling is essential in CFD analysis. As the boundary layer contains the smallest eddies in turbulent flow, resolving these scales require a vast number of grid cells. In order to reduce computational costs, a variety of models are developed that capture flow variables in the boundary layer accurately. These models are based on self-similar behavior of turbulent boundary layers. In RANS, there are two common ways to simulate the behavior of the inner layer of the turbulent boundary layer. Wall functions, developed by using universal relations based on experiments, can be used to model the turbulent boundary layer. These wall functions are generally reasonable accurate and reduce computational costs significantly. The second approach requires a cell size smaller than the height of the viscous sublayer, for $y^+ \leq 5$. From figure 4.9 it can be seen that below $y^+ \leq 5$, the law-of-the-wall depends on a linear relationship between the dimensionless variables, u^+ and y^+. The y^+ is expressed as follows:

$$y^+ = \frac{y u_\tau}{\nu}, \tag{4.1}$$

Here y is the height of the first cell, u_τ is the friction velocity and ν is the kinematic viscosity.
`ENSOLV` does not have the option to use wall functions. Hence, the grid must be suitable of resolving the viscous part of the turbulent boundary layer. The cell size of the first grid cell for $y^+ = 1$ was calculated using flat-plate theory (Schlichting and Gersten, 2001). The following equations were used:

$$C_f = 0.0592 Re_c^{-0.2} \tag{4.2}$$

$$dy = 2\frac{y^+ c}{Re_c \sqrt{\frac{C_f}{2}}} \tag{4.3}$$

Here C_f is the skin friction coefficient and Re_c is the chordwise Reynolds number.

In order to capture the boundary layer correctly, the normal growth rate of the cells in the Navier-Stokes blocks must not exceed 1.2. The in-house tool `strgrd` is used to redistribute the cells within the Navier-Stokes blocks, for $y^+ \approx 1$ and a stretching factor of 1.2. Using the above stated formula, led to an off-wall spacing in the order of 10^-5 to 10^-6 meters. As a result, a large number of cells were required if an universal cell stretching was retained. Therefore, the cell stretching to far-field boundaries was increased. In figure 4.8, the grid distribution of the Navier-Stokes block is depicted.

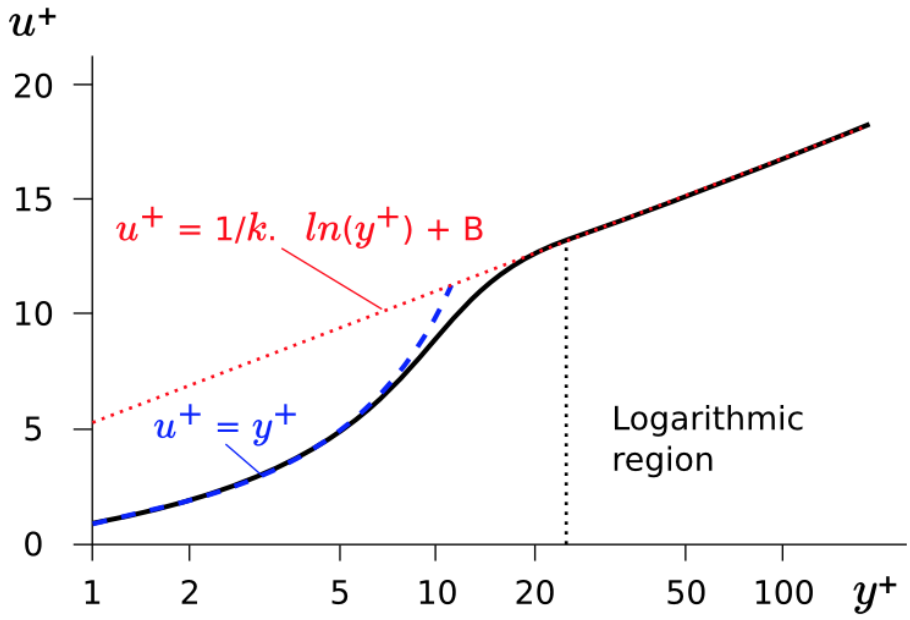

Figure 4.9: The dimensionless boundary-layer profile (CFD Online, 2011)

4.2.5. GRID QUALITY

The final grid quality metrics are obtained by running `ENGRID` in batch mode. A grid quality report is generated, in which different mesh parameters are listed. The mesh characteristics slightly depended on the number of cells, however the values of the quality metrics were reasonable similar. Table 4.2 shows the mesh quality of the grid used in all CFD simulations concerning this work. It must be noted that the grid quality report merely provided maximum values per block. Hence, the averages of those values are added to the presented table in order to give a more complete representation of the grid quality. Yet, the aspect ratio appears substantially large. Due to large dimensions of the model and small volume cells in the NS blocks, the maximum values of aspect ratio were huge. When the NS blocks are omitted from the quality report, the average of maximum values declines to approximately 600. The cells adjacent to the wall and the remaining cells in the NS blocks substantially increased the average values of the aspect ratio heavily.

Mesh quality metrics	Maximum value	Average value
Stretching [-]	1.80	1.32
Turning [∘]	30.0	15.4
Aspect ratio [-]	3.00E5	4.47E4

Table 4.2: Mesh quality metrics of the final grid (Mesh #2 of the grid convergence study)

4.2.6. GRID CONVERGENCE STUDY

Grid convergence is important in CFD analysis as it investigates the effect of grid size on the computational results. It is clear that the solution becomes more accurate for an increasing number of cells. Very fine meshes, on the other hand, require high computation times. Hence, a compromise must be sought between numerical accuracy and computational expenses. In this study, various mesh configurations were tested and analyzed on their performance. For the case shown, various cross-sectional pressures and the lift and drag distribution are shown for an inflow wind speed of $V = 11.5$ m/s over the rigid blade. It was observed that leading edge and trailing edge pressures were highly dependent on the number of chordwise cells and their distributions. However, the enhancement of numerical accuracy by increasing the number of chordwise cells was bounded. It was observed that further grid refinement did not lead to better prediction of pressures, in particular at small z/R. Therefore, three geometrically-equal grids are shown comprising 290 chordwise cells. The mesh characteristics of the three meshes are presented in table 4.3.

Mesh ID	Mesh #1	Mesh #2	Mesh #3
Total # of cells	30M	20M	15M
# of spanwise cells	290	196	168
# of chordwise cells	290	290	290
# of boundary layer cells	64	64	48
max(y^+)	≈1	≈1	≈1

Table 4.3: Mesh characteristics of the three meshes used in the grid convergence study

As shown in figure 4.10 and 4.11, the number of cells in the NS-blocks appeared critical to obtain good results. All meshes produced reasonable similar pressures for the four cross-sections that are shown. Additionally the lift- and drag characteristics over the blade were analyzed. The lift and drag were calculated using the procedure shown in appendix B. Looking at the lift and drag distribution shown in figure 4.12, it can be concluded that Mesh #3 overestimates the lift over the entire span of the blade. Furthermore, these distributions confirm the similarity of Mesh #1 and Mesh #2. It also appeared that the flow at the inboard region did not converge. This was caused by high unsteadiness of the flow over the cylindrical and transition part of the blade. Table 4.4 shows the root-mean-square deviation of the lift-and drag coefficients between three meshes, with and without inclusion of the inboard part of the blade, $z/R < 0.2$. The RMS values show that Mesh #2 produced similar results as Mesh #1. It was decided to use Mesh #2 as a larger mesh size did contribute considerably to the accuracy of the flow solution, while it has substantially saved computation times.

Root-mean square deviation of lift coefficient		
	$0 \leq z/R \leq 1$	$0.2 \leq z/R \leq 1$
Mesh #1 - Mesh #2	0.0625	0.0125
Mesh #2 - Mesh #3	0.2228	0.0377
Mesh #1 - Mesh #3	0.2092	0.0285
Root-mean square deviation of drag coefficient		
	$0 \leq z/R \leq 1$	$0.2 \leq z/R \leq 1$
Mesh #1 - Mesh #2	0.0165	0.0022
Mesh #2 - Mesh #3	0.0767	0.0031
Mesh #1 - Mesh #3	0.0648	0.0049

Table 4.4: Root-mean square deviation of the lift- and drag coefficients between different meshes

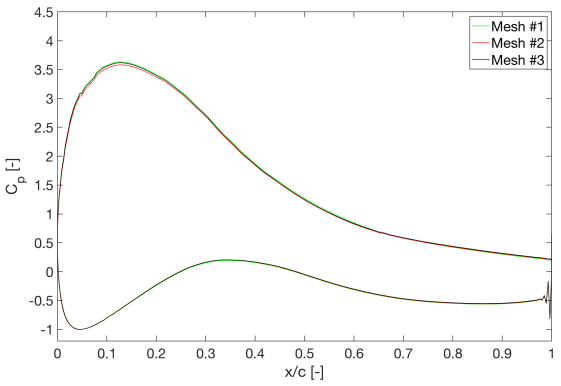

(a) At $z/R = 0.23$

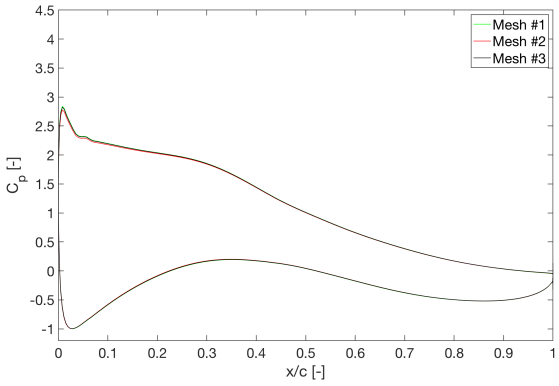

(b) At $z/R = 0.46$

Figure 4.10: Pressure distribution at cross-sections for different meshes

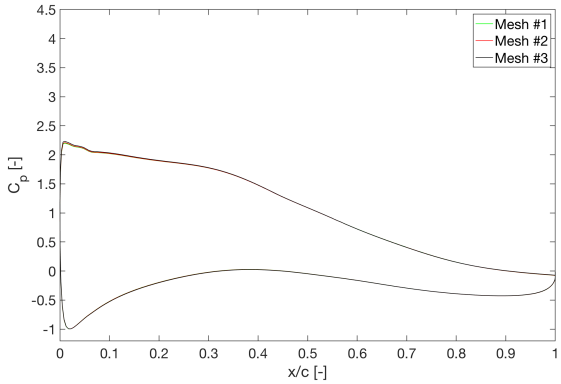

(a) At $z/R = 0.68$

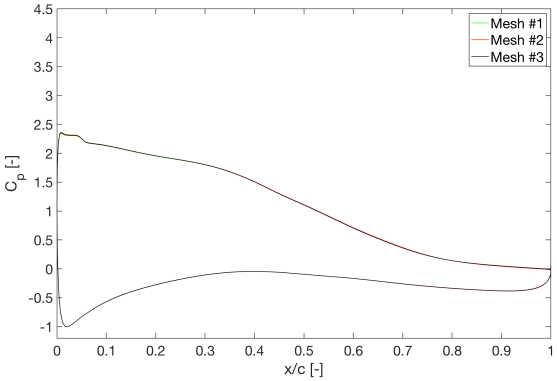

(b) At $z/R = 0.91$

Figure 4.11: Pressure distribution at cross-sections for different meshes

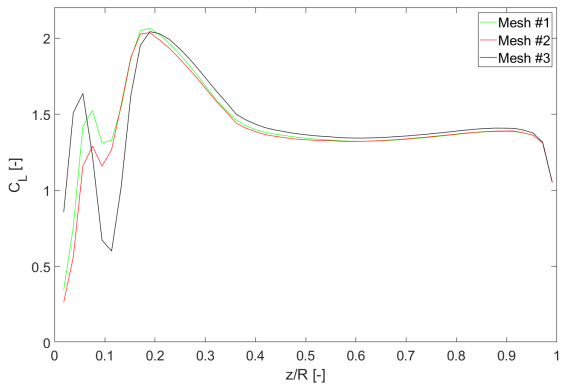

(a) Lift distribution

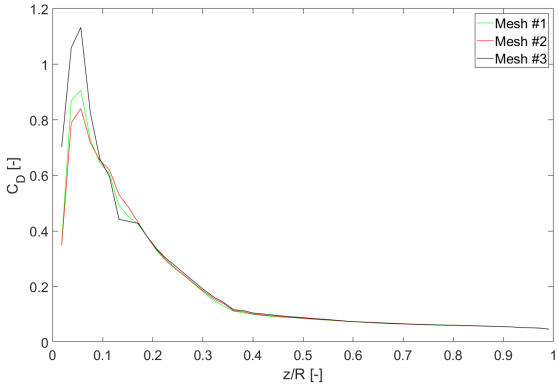

(b) Drag distribution

Figure 4.12: The lift and drag distribution over the span of the blade for different meshes

4.3. COUPLING MODELS

In this study, the Fluid-Structure Interaction (FSI) model was composed of three sub models: a spatial coupling model, a grid-deformation algorithm and time-integration model (for flutter analysis).

4.3.1. SPATIAL COUPLING: VOLUME-SPLINE INTERPOLATION METHOD

Spatial coupling between fluid and structure mesh was performed using the VSI method. Methods of load and data transfer require some basic principles that are explained in this section. The exact working principle of the approach will not be discussed, but can be found in the article by (Hounjet and Meijer, 1995). The interface geometry of fluid and structure mesh is often non-matching. A data exchange method must be applied to transfer information across the discrete interface. A variety of methods were found in literature that produce interpolation matrices required in FSI modelling. The interpolation matrix G_{as} relates the deflections on the structural grid to the deflections on the aerodynamic grid:

$$(\mathbf{h^a}) = [G_{as}](\mathbf{h^s}) \tag{4.4}$$

As shown in the literature review, energy must be conserved over the discrete interface. The transformation of force vectors between aerodynamic and structural grid must be structurally-equivalent (Hounjet and Meijer, 1995). In other words, it is required that aerodynamic forces ($\mathbf{f^a}$) and their structurally equivalent values ($\mathbf{f^s}$) acting on the structural grid do the same virtual work. Conservation of virtual work can be expressed as follows:

$$(\partial\mathbf{h^a})^T(\mathbf{f^a}) = (\partial\mathbf{h^s})^T(\mathbf{f^s}) \tag{4.5}$$

Substituting equation 4.4 into 4.5 gives the following expression:

$$(\partial\mathbf{h^s})^T[G_{as}]^T(\mathbf{f^a}) = (\partial\mathbf{h^s})^T(\mathbf{f^s}) \tag{4.6a}$$

$$(\partial\mathbf{h^s})^T\left[[G_{as}]^T(\mathbf{f^a}) - (\mathbf{f^s})\right] = 0 \tag{4.6b}$$

$$(\mathbf{f^s}) = [G_{as}]^T(\mathbf{f^a}) \tag{4.6c}$$

However, it is known that conservation of virtual work can lead to unphysical oscillations in pressure. In order to transfer loads accurately without artificial effects, the following list of requirements must be met by the interpolation method:

- No unrealistic wild oscillations should occur.
- No pathological end effects should occur. As the number of support points is often limited, the interpolation should not give exceeding values outside the range of support points. It should be noted, however, that interpolation methods are not suited for extrapolation. Thus, the location and number of support points must be chosen carefully.
- The interpolation is exact at the support points.

It is proven that the VSI technique copes with the above stated requirements. Therefore, it was assumed that this method is sufficient if it is correctly applied.

The selection of the support points must be done carefully. It was decided to pick six or seven grid points per cross-section (depending on the number of shear webs) of each spanwise meter, totalling to approximately 1600 support points. The support points were located at the leading edge, trailing edge, midpoint of each shear web and shells at the pressure and suction side respectively. The adequateness of the spatial-coupling algorithm was verified by comparison of deformations on structural mesh and fluid mesh. The deformed and undeformed state of both meshes are shown in figure 4.13 and 4.14. The figures were extracted from the load case where $U_\infty = 11.5$ m/s. Although details are not visible, it shows similarity of the overall displacements.

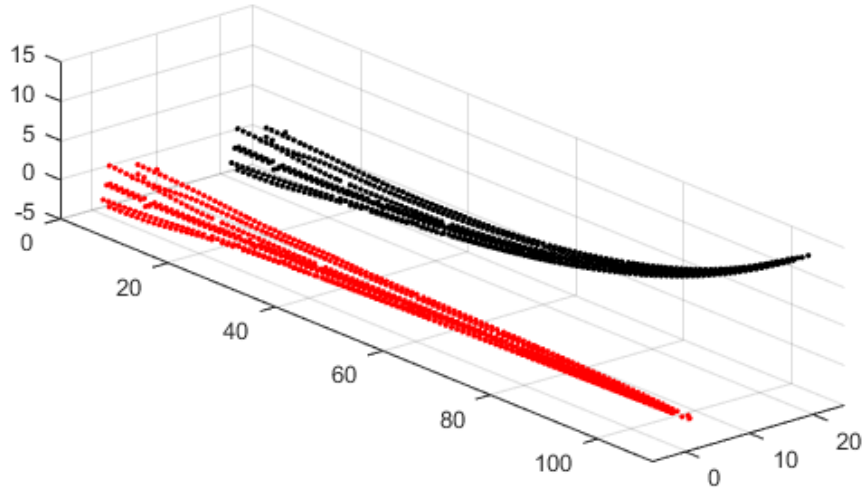

Figure 4.13: Structural nodes of the wind turbine in deformed and undeformed state (U_∞ = 11.5 m/s)

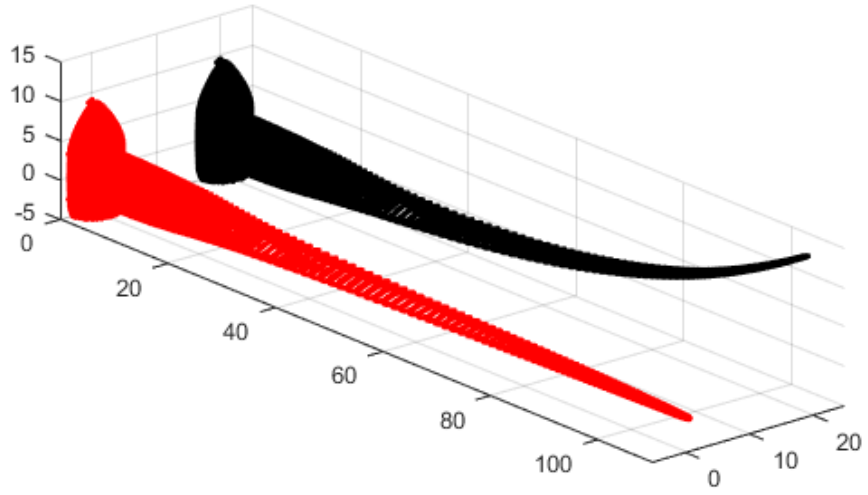

Figure 4.14: Fluid mesh nodes of the wind turbine in deformed and undeformed state (U_∞ = 11.5 m/s)

4.3.2. GRID DEFORMATION: VOLUME-SPLINE INTERPOLATION METHOD AND TRANSFINITE INTERPOLATION METHOD

A grid deformation algorithm was required to deform the multi-block grid in order to adapt the grid as the structure deforms. The algorithm should be kept simple and efficient, but most of all robust and grid-quality conserving. The VSI method used as coupling model can also be used to deform the grid around deflected structure. Applying VSI to deform aerodynamic grids consisting of millions of grid cells leads to high computing times. The systems of equations become excessively large, slowing down the solution process. In order to save time, it was chosen to include a limited set of support points in the mesh-deformation process. Since the displacements of the wind turbine were smooth, no crucial deformation data was lost. It was chosen to specify the grid points modulo to four, implying that one of four successive grid points was used as support point. Moreover, VSI was exclusively used to displace vertices of the blocks. The remainder of the grids points were displaced using the Transfinite Interpolation (TFI) method, since TFI it is very efficient method in deformation of structured grids. As each block consisted of orthogonal grids with i,j,k-topology, normalized arc lengths (s,t,u) of the initial grid can be blended in the TFI formulation preserve initial grid characteristics (Prananta et al., 2000).
The normalized arc lengths in x-direction can be defined as follows:

$$s_{i,j,k} = \frac{\sum_{m=1}^{i} ||\mathbf{x}_{m,j,k} - \mathbf{x}_{m-1,j,k}||}{\sum_{m=1}^{NI} ||\mathbf{x}_{m,j,k} - \mathbf{x}_{m-1,j,k}||} \tag{4.7}$$

Where NI are the number of grid points over the edge in i-direction and $\mathbf{x}$ are the coordinates of the initial grid. This means that $s_{0,j,k} = 0$ and $s_{NI,j,k} = 1$. The determination of new grid locations of surface grids can be expressed as the following two-step recursion formula:

$$d\mathbf{x}^1(i,j) = (1 - s_{i,j})\, d\mathbf{x}(0,j) + s_{i,j}\, d\mathbf{x}(NI,j) \tag{4.8a}$$

$$d\mathbf{x}^2(i,j) = d\mathbf{x}(i,j) + (1 - t_{i,j})\big(d\mathbf{x}(i,0) - d\mathbf{x}^1(i,0)\big) + t_{i,j}\big(d\mathbf{x}(i,NJ) - d\mathbf{x}^1(i,NJ)\big) \tag{4.8b}$$

$$d\mathbf{x}(i,j) = d\mathbf{x}^2(i,j) \tag{4.8c}$$

Where $d\mathbf{x}$ is the set of displacements of block vertices computed by VSI.
Equation 4.8a computes the displacements in the interior of the face in i-direction by straight-line interpolation. Subsequently, equation 4.8b corrects the displacements for contribution in j-direction. In three-dimensional space, the TFI-method considers a three-step recursion formula to compute the displacements. The expressions for the three-dimensional form can be found in the technical report by (Prananta et al., 2000).

4.3.3. TIME-INTEGRATION OF FLUID MODEL: 2ND-ORDER BACKWARD DIFFERENCE SCHEME

In flutter analysis, time-dependent CFD simulations are performed. Solving the unsteady RANS equations requires a time-integration scheme. As the aerodynamic mesh discretizes the flow domain spatially, the flow equations can be expressed as a semi-discrete formulation:

$$\frac{d(VU)_{i,j,k}}{dt} + V_{i,j,k} R(U)_{i,j,k} = 0 \tag{4.9}$$

Where U is the flow-state vector, R is the residual and V is the grid cell velocity.
The second-order backward difference method is the most commonly used integration method available in `ENSOLV`. As shown in literature review, implicit-time integration schemes provide good stability characteristics and therefore it allows to use larger time steps. Applying this scheme to the time derivative leads to the following equation:

$$\psi_1\big((VU)^{n+1}_{i,j,k} - (VU)^{n}_{i,j,k}\big) - \psi_2\big((VU)^{n}_{i,j,k} - (VU)^{n-1}_{i,j,k}\big) + V^{n+1}_{i,j,k} R(U^{n+1})_{i,j,k} = 0 \tag{4.10}$$

Where $\psi_1 = \frac{1}{\Delta t^n} + \frac{1}{\Delta t^n - \Delta t^{n-1}}$ and $\psi_2 = \frac{1}{\Delta t^{n-1}} - \frac{1}{\Delta t^n + \Delta t^{n-1}}$, with $\Delta t^n = t^{n+1} - t^n$. The dual time-stepping method is adopted to solve the resulting equations. Fictitious time steps are introduced reforming the unsteady equations in a quasi-steady problem. As a result, each time step solves a steady state problem that can be described as follows:

$$\widetilde{R}(U^{n+1})_{i,j,k} + P^{n+1}_{i,j,k} = 0 \tag{4.11}$$

In which $\widetilde{R}$ is the unsteady residual: $\widetilde{R}(U^{n+1})_{i,j,k} = \psi_1 U_{i,j,k} + R(U)_{i,j,k}$ and P is a forcing function:

$$P^{n+1}_{i,j,k} = \frac{1}{V^{n+1}_{i,j,k}}\big(-(\psi_1+\psi_2)(VU)^{n}_{i,j,k} + \psi_2 (VU)^{n-1}_{i,j,k}\big) \tag{4.12}$$

As may noticed, the equations include grid cell velocities. Grid cell velocities must be accounted for as they produce additional convective fluxes. Most commonly, they are computed by volumes swept by cell faces between two time steps. The exact procedure of computing the grid velocity can be found in the following technical report by (Prananta et al., 2000).

4.4. FLUID MODEL

The literature review showed that RANS is capable of solving wind turbine aerodynamics with good accuracy. As the considered test cases comprised normal operating conditions, attached flow was expected for most part of the blade. For attached flow, it is assumed that RANS resolves the flow accurately.

4.4.1. LOW-MACH PRECONDITIONING

The derivation of the compressible RANS equations is explained in literature review. Wind turbine flow can be considered low-speed and therefore is regarded as incompressible flow. For low speed flow, the compressible flow equations become stiff due to a large disparity between acoustic wave speed and convective wave speed. As a consequence, the convergence of steady-state computations may deteriorate. To alleviate this problem, low-Mach preconditioning can be applied. These methods change the eigenvalues of the system reducing the disparity of wave speeds. Although the Mach number of incoming wind is relatively low, the local flow velocities over the blade exceeded Mach = 0.1. Hence, in case no convergence-related problems emerged, it was chosen not to apply low-Mach preconditioning in the current study.

4.4.2. SOLUTION PROCEDURE

`ENSOLV` utilizes a highly efficient solution scheme that achieves an acceleration factor of 2 to 10 in comparison to conventional solution methods. The so-called multi-grid scheme performs relaxations on different grid levels to accelerate the convergence on the finest grid level. The solutiona on coarser levels of the computational grid are used to make large wavelength components of the error converge faster. There are many variations in multi-grid algorithms, but the principle remains the same. The restriction operator transfers the solution and residual of a fine grid to a coarser grid, where computations are performed to correct the fine grid solution. The exact working principle can be found in documentation about `ENSOLV` (Kok, 2019). The multi-grid scheme is shown in figure 4.15.

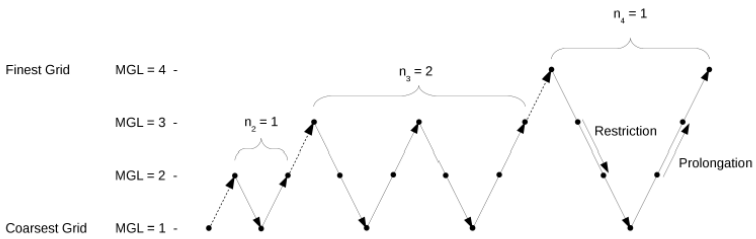

Figure 4.15: The multi-grid scheme

4.4.3. VERIFICATION

A former NLR graduate student already validated `ENSOLV` for wind turbine aerodynamics. (Ten Pas, 2016) used wind tunnel data publicly available from the EU project Mexico (Schepers et al., 2012) to validate the flow solver. The measurements were carried out on a 4.5-meters diameter rigid wind turbine model in the Large-Low Speed wind facility of DNW (German-Dutch Wind Tunnels).
The results were in good agreement with experimental data. However, the wind turbine used in the current study possesses some unique design features that differentiates itself from the validated model. Because of its extreme scale, the structural design had to satisfy high structural requirements. As a result, the blade design incorporated a thick cylindrical-shaped profile at the root that smoothly transforms into thick airfoils

with blunt trailing edges. These profiles may cause flow separation, which could lead to inaccurate solutions as the utilized fluid model lacks sufficient transition and turbulence models. Since no validation data was directly available for this blade design, the fluid model was verified following a two-step approach.

In literature, experimental data was found for the DU97-W-300-10 flatback airfoil, one of the thick-trailing edge profiles incorporated in the blade design. The first verification step consisted of comparing two-dimensional CFD data to experimental data from wind tunnel testing. The second verification step compared pressure distributions at several spanwise sections of the three-dimensional CFD solution to pressure distributions computed by `Xfoil` and `Rfoil`.

C_p-DISTRIBUTION ALONG THE DU97-W-300-10 FLATBACK AIRFOIL

In the Virginia Tech Stability wind tunnel, wind tunnel measurements were conducted to determine the noise and aerodynamic performance characteristics of a 10%-thick trailing edge version of the DU97-W-300 airfoil (Berg and Barone, 2008). The experiment was carried out in a propeller-powered wind tunnel, providing a Reynolds number of $Re_c = 3.2 \cdot 10^6$, and the airfoil was placed at ten degrees angle of attack. The boundary layer was tripped by placing zigzag tape at $x/c = 0.05$ and $x/c = 0.1$, on the upper and lower surface respectively. According to the article, stall conditions were not reached, implying two-dimensional attached flow conditions. The pressures obtained from measurements were compared to two-dimensional computations performed in `Xfoil` and `ENSOLV`, shown in figure 4.16. It can be observed that the computed pressures deviated from experimental results. It appeared that `Xfoil` significantly overestimated the suction peak, which corresponds to findings in literature (Ramanujam and Ozdemir, 2017). The suction peak observed in the CFD pressures was in reasonable agreement with experimental data, however the suction side pressures were underestimated over the majority of the chord length. Based on these results, it was difficult to state to what extent the fluid model accurately predict the pressures over a blunt trailing edge airfoil. For this reason, an additional verification step was performed.

SECTIONAL C_p-DISTRIBUTIONS ALONG THE WIND TURBINE BLADE

Since the experimental data was based on two-dimensional flow, also computations were carried out taking into account three-dimensional flow effects. The sectional pressure distributions at several spanwise locations from the full-rotor CFD simulation were compared to the results from `Rfoil` and `Xfoil`, where the pressures obtained from `Rfoil` were corrected for rotational effects. As shown in figure 4.17, the pressure distributions at four cross-sections ($z/R = 0.37$, $z/R = 0.48$,$z/R = 0.90$ and $z/R = 0.99$) were analyzed.
Due to the rotating motion of the blade, the pressure coefficient must be computed differently than usual. A different expression for the dynamic pressure must be substituted, leading to:

$$C_P = \frac{p - p_\infty}{\frac{1}{2}\rho\left(U_\infty^2 + (\omega R)^2\right)} \tag{4.13}$$

Here p is the static pressure, ρ is the density, p_∞ is the atmospheric pressure, U_∞ is the wind velocity, Ω the angular velocity in rad/s and R the distance to rotation axis.
It can be noticed that `Xfoil` predicted higher values for the pressure than the CFD computations. This is a consequence of assumptions made in the determination of the wake geometry (Ramanujam and Ozdemir, 2017), based on assumption of inviscid flow. In `Rfoil` a scheme is implemented that includes viscous effects in the determination of the wake geometry, which has led to better lift predictions. The results showed that `Rfoil` approached the CFD results more closely, especially for the most inboard section. Furthermore a large disparity in suction peak pressure can be seen at the outermost cross-section. The reason for this effect may be two-fold. First of all, the reduction in pressure can be denoted to the tip-effect. Earlier findings of (Lindenburg, 2003) had proven that sectional lift is reduced for rotating airfoils. Two-dimensional methods do not account for three-dimensional flow effects at the tip causing an overprediction of the suction peak. Additionally, as the stagnation point slightly shifted, it can be concluded that the angle of attack changed. As long as two-dimensional flow occurs, `Rfoil` and `ENSOLV` predict similar sectional pressure distributions.

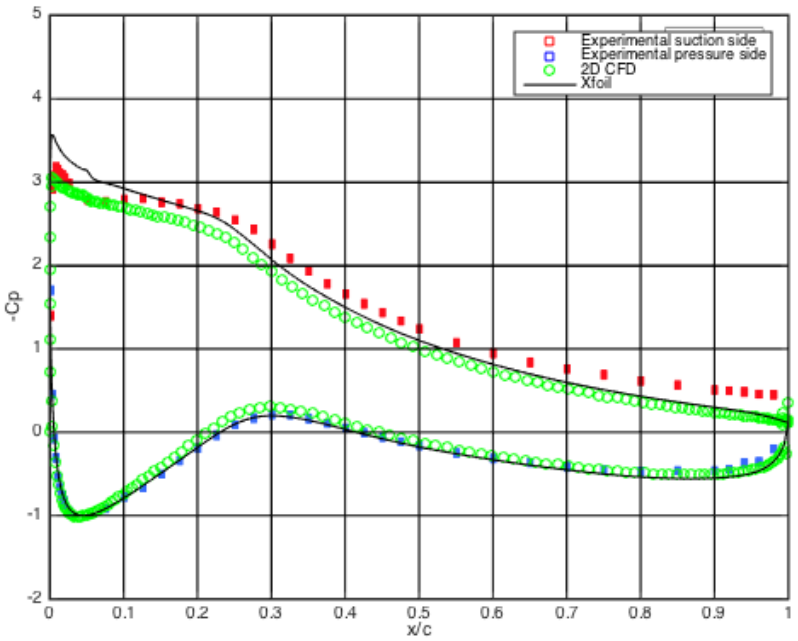

Figure 4.16: Comparison pressure distribution over DU97-W-300-10 flatback airfoil between experimental data, 2D CFD and Rfoil for $Re_c = 3.2 \cdot 10^6$ and $\alpha = 10°$ (Berg and Barone, 2008).

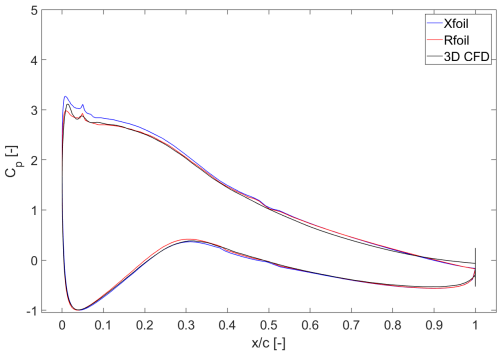

(a) At $z/R = 0.37$ with $t/c = 0.3$

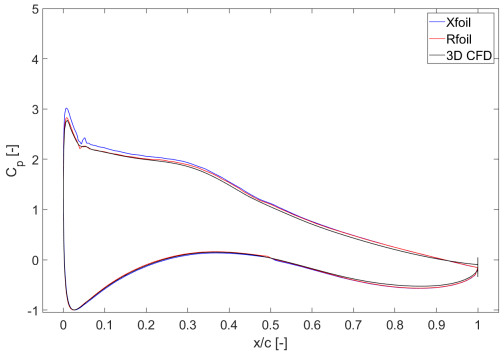

(b) At $z/R = 0.48$ with $t/c = 0.25$

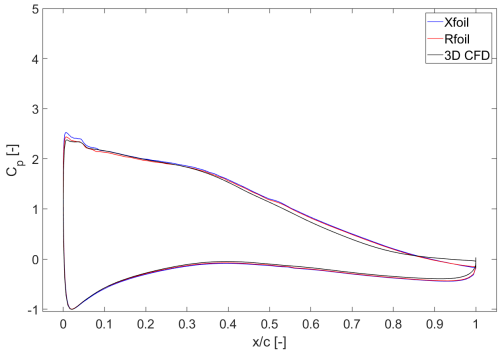

(c) At $z/R = 0.90$ with $t/c = 0.21$

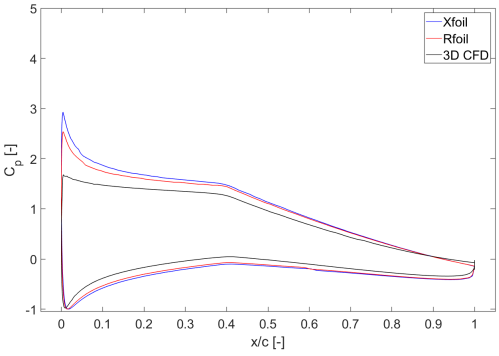

(d) At $z/R = 0.99$ with $t/c = 0.18$

Figure 4.17: Comparison of the pressure distributions at several spanwise locations

4.5. STRUCTURAL MODEL

The structural model used is a three-dimensional FEM model provided by *We4Ce*. Since the model is compatible with `Nastran`, a wide range of solution methods can be applied to assess its behavior. As mentioned in the methodology, the Guyan reduced model was used in the semi-nonlinear aeroelastic approach. Several test cases were performed to verify its performance compared to the original model.

4.5.1. MODEL DESCRIPTION

As shown in figure 4.18, the overall lay-out of the structure consists of an outer shell and multiple inner shear webs, varying in number and location throughout the span of the blade. As mentioned earlier in this chapter, the structural model was automatically generated using the integrated design tool `FOCUS`. Due to the vast decrease in chord towards the tip, the integrated mesh-generation tool of `FOCUS` constructed deteriorated elements at the tip. In order to avoid numerical issues, the FEM model was shortened by a meter.

The blade geometry is meshed using quadrilateral shell elements, in which material properties of the composite laminates are described using a combination of PCOMPG cards and MAT8 cards. The PCOMPG card enabled to define the properties of a multi-ply composite laminate layer-by-layer, while the MAT8 card defined the composite plies as orthotropic material. CLT was used to compute the equivalent properties of a plate from the material definitions (Sale et al., 2013). An elaborate explanation of the implementation of this theory in `Nastran` can be found in `Nastran`'s user manual (MSC Software Corporation, 2017). As already mentioned in section 4.2.2, the hub was not designed yet. Since the hub was not of interest, the root of the blade was fixed using single-point constraints (SPC's).

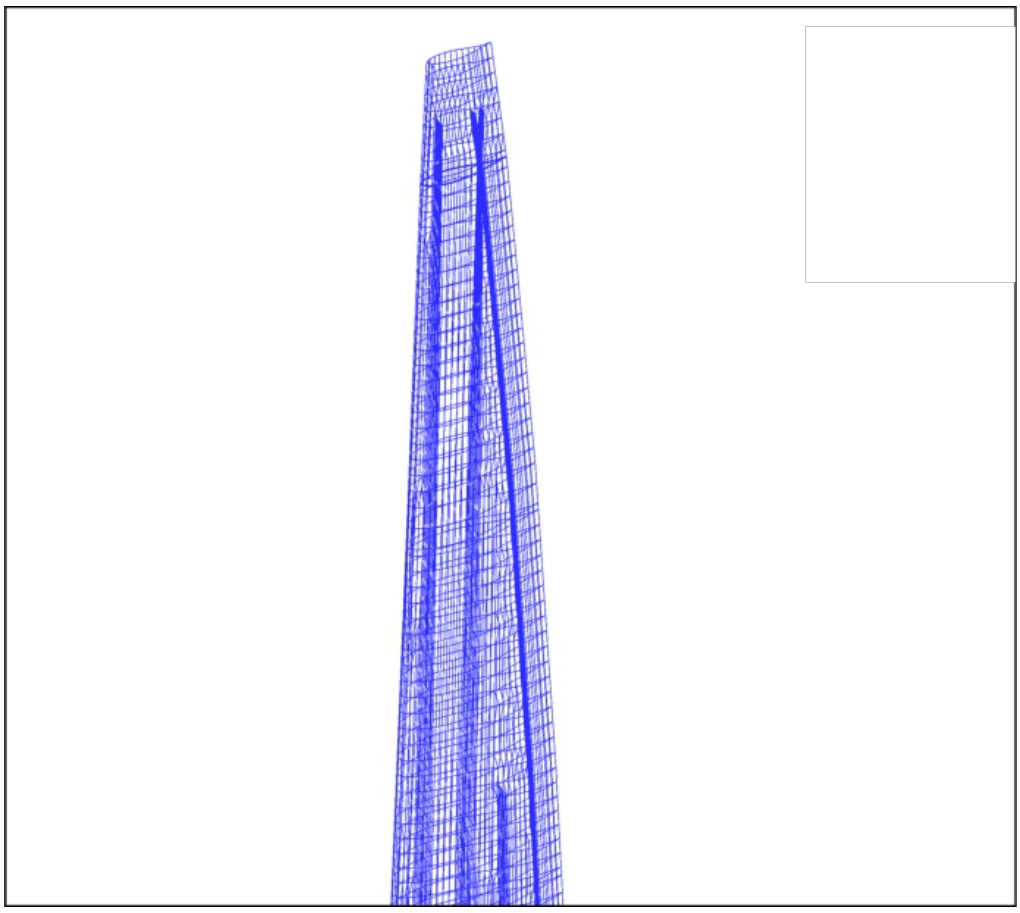

Figure 4.18: A close-up from the tip of the three-dimensional FEM model

4.5.2. MODEL ADJUSTMENT

As stated earlier in this chapter, the FEM model was one meter shorter than the aerodynamic problem. Problems may be arise in the coupling between both models. In particular, artificial displacements can originate at the tip due to a lack of surrounding support points. In fact, the tip displacements must be extrapolated to the aerodynamic model. The VSI provided a zero-th order extrapolation, resulting in an unphysical representation of the tip. To resolve this, additional support points were added to the tip to ensure correct interpolation of the tip displacements. It was chosen to add two structural nodes at the location of the tip leading- and trailing edge respectively. They were connected to the existing structural model using rigid bar elements (RBE2 elements). However, in this manner, a singular stiffness matrix was generated because these elements have an infinite stiffness. In order to resolve this, the added tip nodes were duplicated and connected their equal using an extreme stiff spring element. This technique appeared to work. The model adjustment resulted in linear extrapolation of the displacements to the tip.

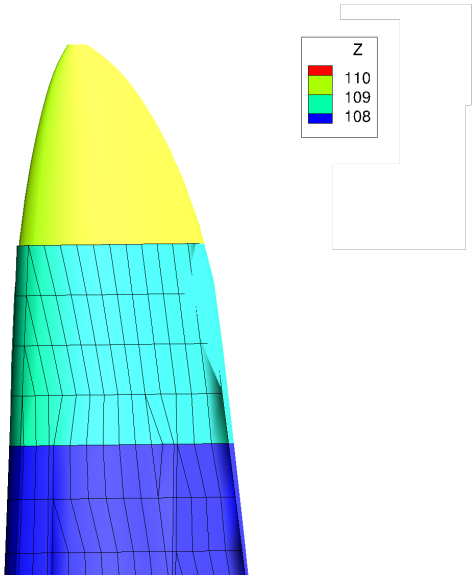

Figure 4.19: Representation of the fluid and structural model at the tip

4.5.3. VERIFICATION

Two test cases were performed in the verification of the reduced model, including static analysis and modal analysis.

STATIC ANALYSIS

As mentioned in the methodology, Guyan reduction provides an exact representation of the linear material stiffness matrix. Hence, in linear static analysis both models would compute similar displacements in matching nodes. Accordingly, the reduced model is verified by comparing the results to the solution of nonlinear static analysis. For nonlinear static analysis, it is required to adopt the full model. Table 4.5 summarizes the performed test cases.

Bending		
Test case	Load type	Load magnitude
Tipload 10 kN	Force in flapwise direction (F_x)	10 kN
Tipload 40 kN	Force in flapwise direction (F_x)	40 kN
Tipload 10 kN	Force in edgewise direction (F_y)	1 kN
Torsion		
Test case	Load type	Load magnitude
Tiptorsion 10 kNm	Moment around z-axis (M_z)	10 kNm

Table 4.5: Static test cases considered for verification of the reduced model

The displacements resulting from the various load cases are presented in table 4.6. Considering the displacements are small, the reduced model produced similar results. Although the differences are small, it can be observed that they increasingly deviate as the loads were amplified. It can be concluded that the model reduction did not effect static analysis.

Bending		
Test case	Flapwise displacement (full)	Flapwise displacement (reduced)
Tipload 10 kN	$8.1783 \cdot 10^{-1}$ m	$8.1787 \cdot 10^{-1}$ m
Tipload 40 kN	3.2556 m	3.2715 m
Test case	Edgewise displacement (full)	Edgewise displacement (reduced)
Tipload 10 kN	$2.1074 \cdot 10^{-1}$ m	$2.1075 \cdot 10^{-1}$ m
Torsion		
Test case	Torsion (full)	Torsion (reduced)
Tiptorsion 10 kNm	$9.7609 \cdot 10^{-2}$°	$9.7641 \cdot 10^{-2}$°

Table 4.6: Results of the static test cases considered for verification of the reduced model

MODAL ANALYSIS

The second test case involved modal analysis in order to assess the influence of reduction on dynamic properties of the model. The modal analysis was performed for a rotating blade analogous to the first test case (U_∞ = 11.5 m/s). This implies that both models are pre-stressed by a centrifugal force corresponding to an angular velocity of Ω = 8.7 RPM. Table 4.7 shows the results of the modal analysis. It appeared that higher modes were more significantly affected in terms of their natural frequency. Subsequently, a Modal Assurance Criterion (MAC) analysis was carried out to determine the similarity of the mode shapes of both models. The MAC value is calculated as the normalized dot product of two sets of vectors and can be thought of being the correlation between two modal vectors squared:

$$MAC(\{\phi_f\},\{\phi_r\}) = \frac{|\{\phi_f\}^T\{\phi_r\}|^2}{(\{\phi_f\}^T\{\phi_f\})(\{\phi_r\}^T\{\phi_r\})} \tag{4.14}$$

Here ϕ_f is one of the modal vectors of the full model and ϕ_r is the corresponding modal vector of the reduced model.

Due to omitted mass effects, the computed modal characteristics of the wind turbine blade changed. The MAC values showed a similar trend as the differences in frequencies. Depending on the set of "active" nodes, mode shape and natural frequency, the modal characteristics were influenced by the model reduction. In order to ensure a proper characterization of the structure of the blade, the modal characteristics of the full blade were used in the "linear" flutter analysis.

Mode number	Full model [Hz]	Reduced model [Hz]	Difference [%]	MAC [%]
1	0.525	0.525	0.00	100.0
2	0.732	0.732	0.00	100.0
3	1.347	1.348	0.05	100.0
4	2.180	2.191	0.47	100.0
5	2.668	2.675	0.25	100.0
6	4.174	4.219	1.08	99.9
7	4.300	4.346	1.08	98.9
8	4.602	4.704	2.22	98.4
9	6.359	6.455	1.51	99.7
10	7.432	7.760	4.41	78.9
11	7.666	8.154	6.37	77.3
12	8.548	8.778	2.72	99.3

Table 4.7: Results of the modal analysis for the full and reduced structural model (Ω = 8.7 RPM)

4.5.4. BUCKLING ANALYSIS

In the continuous upscaling of wind turbines, optimum design strategies were adopted to limit the weight increase of the blades. These strategies have led to the use of alternative materials and thin-walled structures, which raised the risk on buckling behavior (Ounis and Balehouane, 2016). The linear-elastic buckling finite element analysis of structures can be formulated as an eigenvalue problem (Zienkiewicz and Taylor, 2005):

$$([K] + \lambda[K_G])\phi = 0, \tag{4.15}$$

where $[K]$ is the global stiffness matrix, λ is the buckling load factor, $[K_G]$ is the geometric stiffness matrix and ϕ are the buckling modes. The linear geometric stiffness (or differential stiffness) matrix is created by initial stresses due to pre-loading the structure for the specific load case. As linear analysis is considered, the geometric stiffness depends linear on the displacements.

5

RESULTS

The results of the performed simulations are presented in this chapter. Two similar simulations of a rotating wind turbine were considered, for different wind speeds: $U_\infty = 7$ m/s and $U_\infty = 11.5$ m/s. The associated operational parameters to these two load cases are shown in table 5.1. The most important parameters specified in the input files of ENSOLV can be found in appendix .

Simulation conditions				
Load case	V [m/s]	Ω [rev/min]	Pitch angle [$\circ$]	Tip speed ratio [-]
1	11.5	8.7	0.5	8.7
2	7	6.3	0.5	10.4

Table 5.1: The two simulation conditions that are considered

5.1. LOAD CASE 1

The first case considered an uniform inflow of 11.5 m/s. According to the design curve shown in the methodology, the axial forces are largest for this load case. Hence, it is expected that the nonlinear structural effects will be most prominent.

The aerodynamics around the rigid blade is discussed prior to the results of the static aeroelastic simulation in order to gain insight on the overall flow development. Subsequently, the effect of deformations on the aerodynamic loads was assessed.

5.1.1. AERODYNAMICS AROUND RIGID BLADE

This section presents the steady aerodynamic solution around the jig shape of the rotor. The flow characteristics are discussed by means of convergence data, velocity- and pressure plots and streamlines.

RESIDUAL ANALYSIS

The convergence of the flow solver was checked to assure that the solution had reached a steady-state. For this simulation, three grid levels were used in the multi-grid scheme, in which the number of iterations was set to 5000 per grid level. Due to the multi-grid scheme, a single CFD analysis can also serve as a grid convergence study. Since the mesh coarsened with order two, the approximate grid sizes could easily be calculated with the knowledge that the fine grid contained ≈20 million cells. Table 5.2 provides a brief summary of the cell sizes:

Mesh refinement	Total number of grid cells
Fine	20M
Medium	2.5M
Coarse	0.3M

Table 5.2: Summary of grid sizes used in residual analysis

The particular wind speed of U_∞ = 11.5 m/s will apparently result in attached flow as this load case concerns an operational condition of the design curve. Therefore, it was expected that the flow solver would not have major difficulties in reaching a converged flow solution. Figure 5.1 shows that the residuals of the steady-state flow solver decreased by approximately four orders of magnitude, implying reasonable convergence. However, they did not progress to commonly desired convergence levels in the order of 10^{-4}. The root mean square (RMS) residuals stagnated and started oscillating around a final value. Stagnation of the residual values could imply bad grid quality or unsteadiness in the flow. It is also clearly visible that the coarse grid level reached substantially lower residual values. This signified that eventual unsteadiness of the flow was not presented by the coarse grid. Bad grid quality could however lead to inaccuracies leading to errors in computed aerodynamic forces. Hence the convergence of the aerodynamic forces is checked.

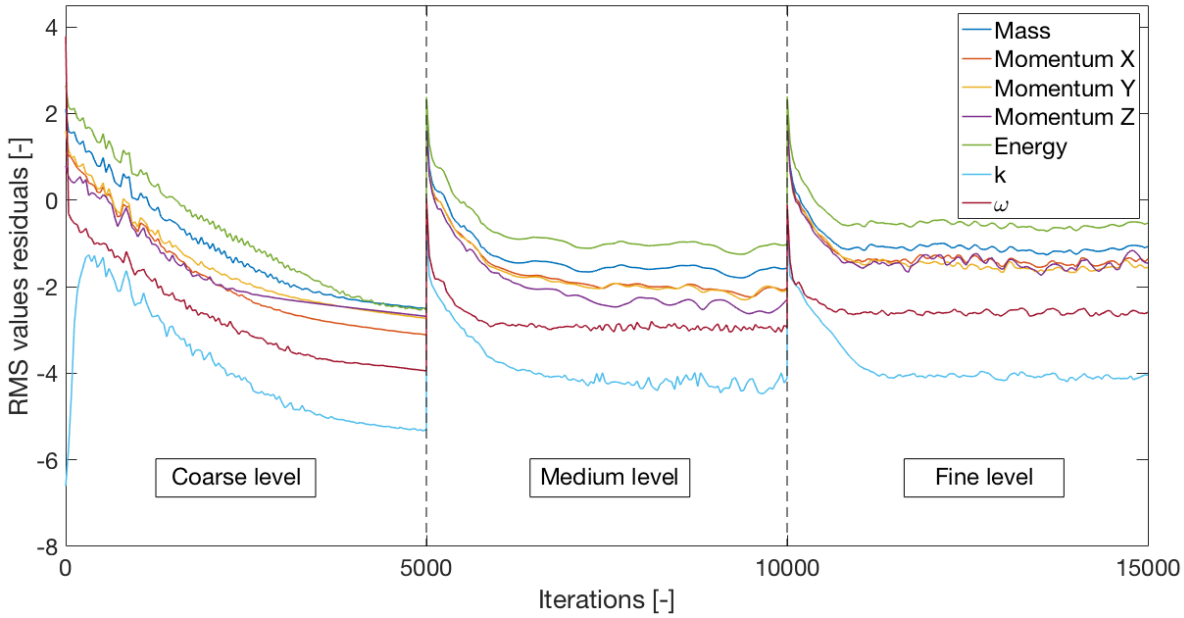

Figure 5.1: Residual plots from steady aerodynamic simulation in ENSOLV (U_∞ = 11.5 m/s)

Only the development of the total forces of the rotor were available in the convergence file.

CONVERGENCE OF AERODYNAMIC FORCES

Unfortunately, ENSOLV only records the total forces on the object in the convergence file. In the analysis of wind turbines, this results in a distorted view of the working forces. As the in-plane forces of the separate blades work in opposite directions, the recorded in-plane force cancels out. Since the out-of-plane forces are most significant in the aeroelastic deformations, these give a good impression of the accuracies attained. To give a clear representation of the force magnitudes reached after convergence, the force development of the distinct meshes is presented in figure 5.2. It must be noticed that the thrust force (i.e. force in x-direction) of the full rotor is shown. The convergence plot showed that the thrust converged to a final value. Additionally, the force differences showed that a relatively large mesh was needed to obtain good results. As was shown in the convergence study, the solution deteriorated when less cells were used in the boundary layer or in the chordwise direction. It is advised to use a sufficient number of grid cells in order to predict correct pressure distributions. In particular, the leading- and trailing edge region require a denser grid distributions as the pressure gradients are large in those areas.

The final forces and moments working on the wind turbine rotor are shown in table 5.3. The results showed that the force in y-direction differs most between both blades. It was concluded that the discrepancy between both blades was the result of unsteady flow at the root. In fact, residual information given by the output file showed that RMS values were highest in the blocks around the hub and cylindrical-shaped blade segment.

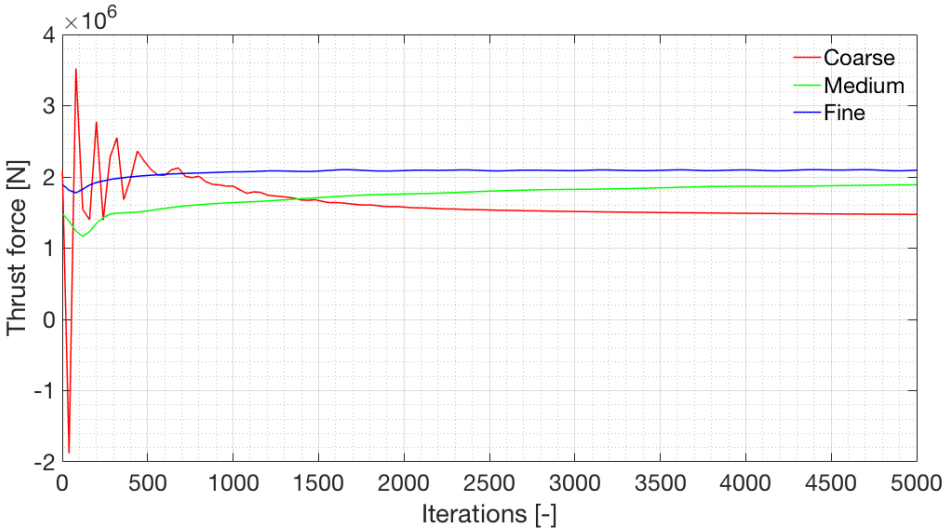

Figure 5.2: Grid convergence analysis of thrust force

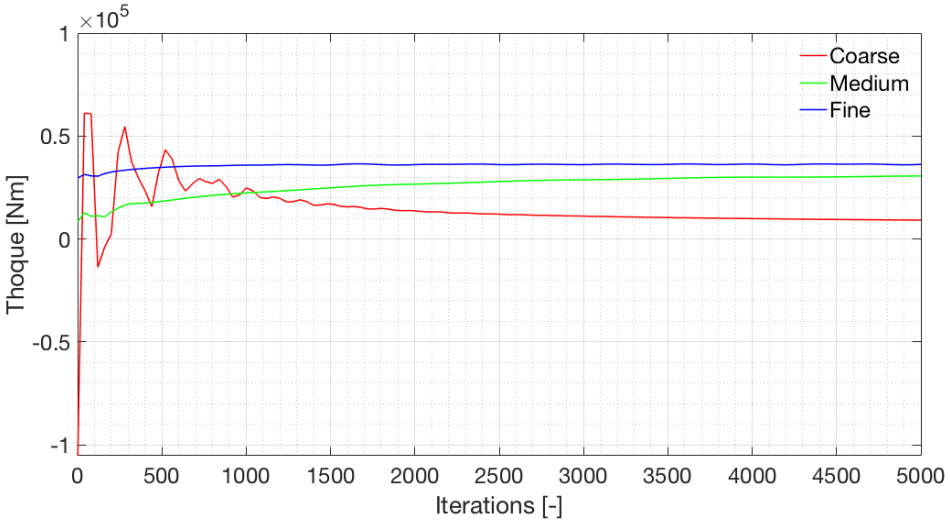

Figure 5.3: Grid convergence analysis of torque

Forces			
Component	$\sum F_x$	$\sum F_y$	$\sum F_z$
Upper blade	$1.0467 \cdot 10^6$ N	$-1.4960 \cdot 10^5$ N	$2.5129 \cdot 10^4$ N
Lower blade	$1.0455 \cdot 10^6$ N	$1.5471 \cdot 10^5$ N	$-2.5358 \cdot 10^4$ N
Hub	$2.4851 \cdot 10^3$ N	$1.8694 \cdot 10^3$ N	$2.4738 \cdot 10^2$ N
Moments			
Component	$\sum M_x$	$\sum M_y$	$\sum M_z$
Upper blade	$-9.1230 \cdot 10^6$ N·m	$7.4274 \cdot 10^7$ N·m	$9.6304 \cdot 10^4$ N·m
Lower blade	$-9.1209 \cdot 10^6$ N·m	$-7.3978 \cdot 10^7$ N·m	$-9.3607 \cdot 10^4$ N·m
Hub blade	$4.4926 \cdot 10^1$ N·m	$4.4237 \cdot 10^2$ N·m	$-2.6243 \cdot 10^3$ N·m

Table 5.3: Final forces and moments per component (U_∞ = 11.5 m/s)

FLOW AND PRESSURE PLOTS

To visualize the flow around the blade, `Tecplot` was used to generate velocity, pressure and streamline plots at several cross-sections. To get a clear representation of the pressures, additionally the pressure distributions were given. The flow variables shown in the plots are normalized by the local free-stream velocity. At $z/R = 0.12$, massive flow separation occurred behind the blade segment as shown in figure 5.4a. Transition from the cylindrical root to thick blunt trailing edge airfoils takes place in this region. As expected, the flow was unsteadiness in this region. The steady solver attempted to solve the unsteady flow, resulting in a vortical flow structure. However, as the streamlines merged downstream, it can be concluded that it was not capable of capturing unsteady vortex shedding. Figure 5.7a shows that a significant adverse pressure gradient arises slightly aft the location of the suction peak, leading to onset of flow separation. This was obviously an effect of the thick profile. The flow phenomenon observed explained the stagnation of residuals. Furthermore as shown in figure 5.6, it appeared that separated air was driven outwards, resulting in a radial velocity component. Highly three-dimensional flow emerged. In the middle region of the blade the flow is nicely attached and two-dimensional. Figure 5.7b shows excellent aerodynamic properties of the blunt trailing edge airfoil. Minor numerical issues appeared at the trailing edge, as consequence of the discontinuous shape. Lastly, at $z/R = 0.90$ the flow was attached, but three-dimensional occurred. This was caused by the tip. The difference in radial flow speed implied the formation of a tip vortex. In order to adequately analyze this effect, unsteady computations must be performed. In case of interest, additional flow and pressure plots are given in appendix C.

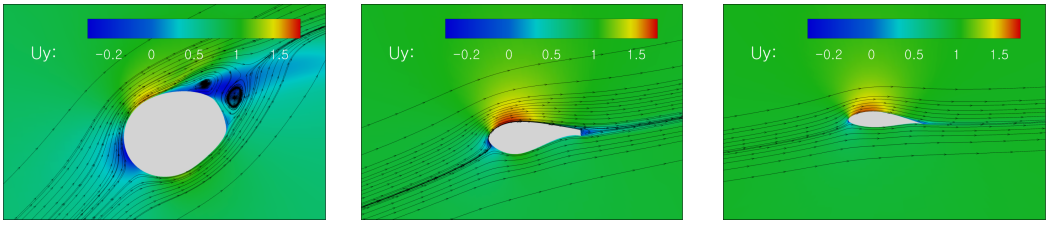

(a) $z/R = 0.12$ (b) $z/R = 0.31$ (c) $z/R = 0.90$

Figure 5.4: Streamlines and velocity in y-direction at several spanwise cross-sections ($U_\infty = 11.5$ m/s)

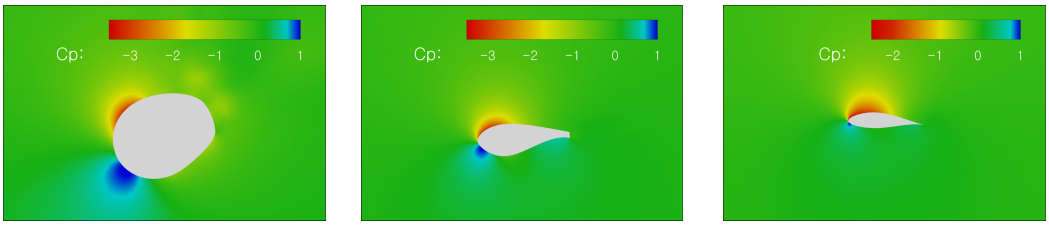

(a) $z/R = 0.12$ (b) $z/R = 0.31$ (c) $z/R = 0.90$

Figure 5.5: Contour plots of pressure at several spanwise cross-sections ($U_\infty = 11.5$ m/s)

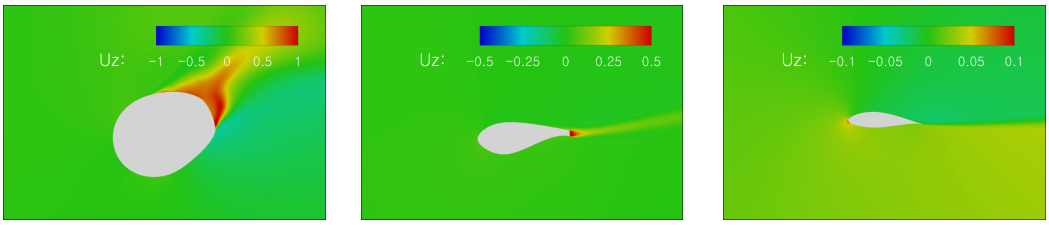

(a) $z/R = 0.12$ (b) $z/R = 0.31$ (c) $z/R = 0.90$

Figure 5.6: Velocity in z-direction at several spanwise cross-sections ($U_\infty = 11.5$ m/s)

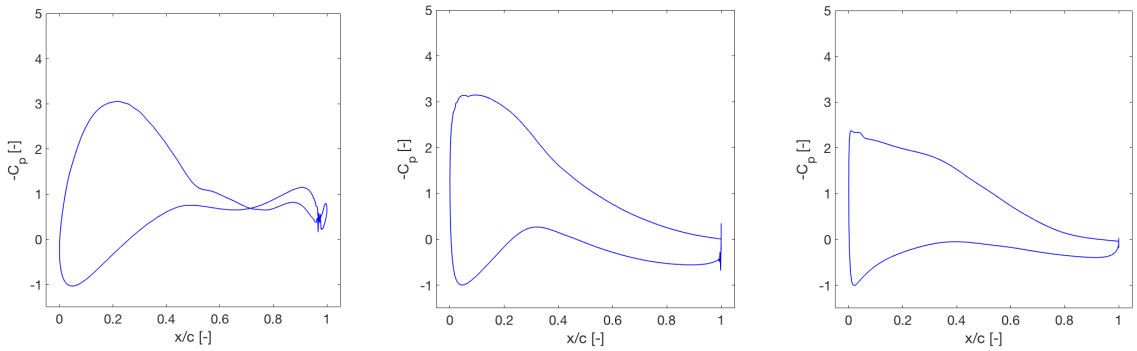

(a) $z/R = 0.12$ (b) $z/R = 0.31$ (c) $z/R = 0.90$

Figure 5.7: Pressure distribution at several spanwise cross-sections ($U_\infty = 11.5$ m/s)

Realizing that flow separation occurred, it was interesting to determine to what extent his behavior applied to the blade. As mentioned in the methodology, the surface walls imply zero tangential and normal velocity. The no-slip condition was applied. In order to determine the onset of flow separation, an alternative method must be performed. It was chosen to analyze the skin friction lines on the surface. These lines were calculated by taking the streamlines of the vector field of wall shear stress. The resulting streamlines can be found in figure 5.9 and confirmed that the flow is mainly separated at the root. Towards the tip, it seemed that a skin friction line was located slightly upstream of the trailing edge as can be observed at both sides of the blade. Although no flow separation was observed in the velocity plots, this could indicate that a slight portion of trailing edge separation occurred.

COMPARISON TO BLADE-ELEMENT MOMENTUM RESULTS

The aerodynamic loads obtained from CFD analysis are compared to BEM results. As shown earlier in this chapter, the majority of the blade exhibited two-dimensional attached flow conditions. It was assumed that BEM could give similar results. The flapwise and edgewise forces are depicted in figure 5.8. The lift- and drag polars used in the BEM computations, were obtained from `Rfoil` calculations. As it appeared that `Rfoil` did not produce correct data for the inboard segments, the transitional and cylindrical region were replaced by the thickest integrated airfoil profile. Hence at the inboard region the flapwise force displayed a linear behavior. It appeared that `Rfoil` slightly overestimated the flapwise forces. While in the middle part of the blade, the estimation of the edgewise forces reduced. The discrepancies in lift- and drag were already observed in literature and analyzed in the fluid model verification in chapter 4. When the force distributions were compared without including the results of $z/R \neq 0.35$, it was shown that BEM results deviated 2.7% and 3.8% from the flap- and edgewise forced computed by CFD respectively. It can be concluded that for attached conditions, BEM gives a good estimate of aerodynamic forces. But BEM does not produce adequate solutions when more complex or critical flow conditions originated. Experimental data or high-fidelity analysis must be performed to determine appropriate corrections.

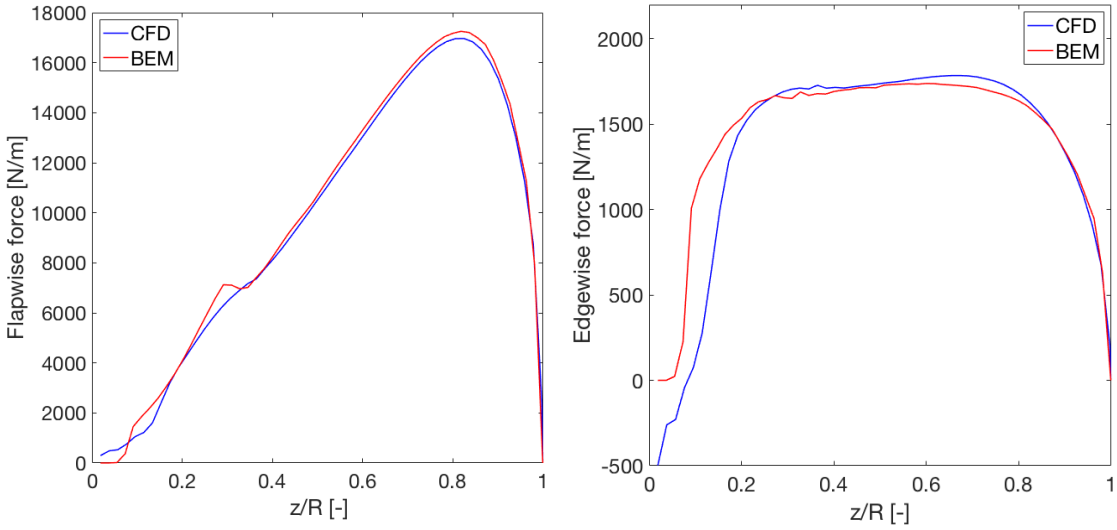

(a) Flapwise forces over the blade

(b) Edgewise forces over the blade

Figure 5.8: Comparison of CFD and BEM results for steady flow (U_∞ = 11.5 m/s)

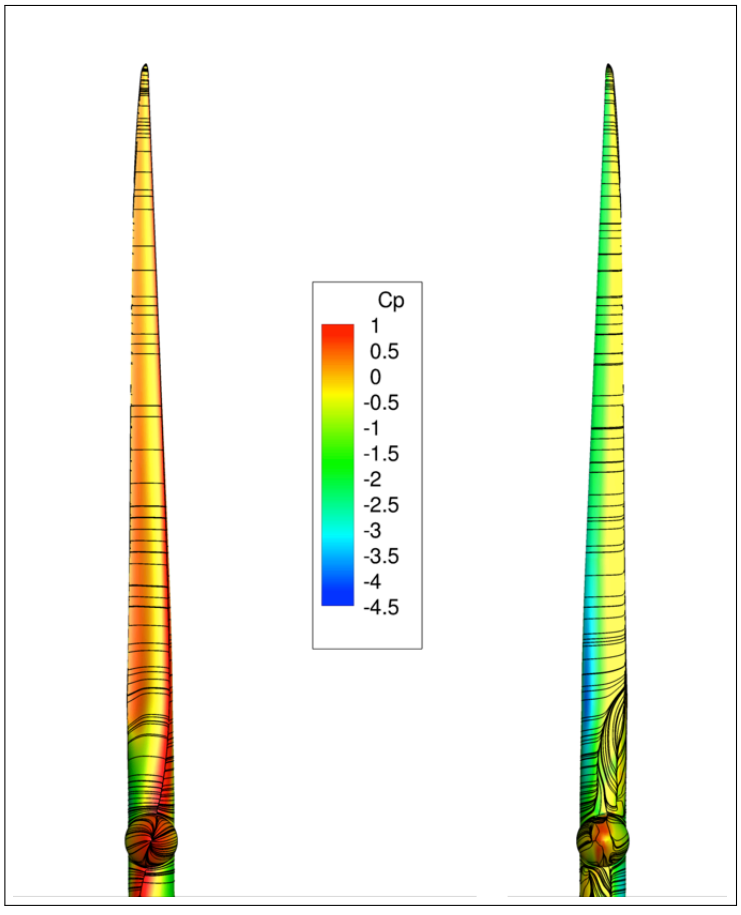

Figure 5.9: Limiting streamlines and pressure coefficient on the pressure (left) and suction (right) side of the rigid wind turbine blade (for U_∞ = 11.5 m/s)

5.1.2. STATIC AEROELASTIC SIMULATION

In this section, the results from the static aeroelastic analysis are presented. As described in the methodology, the steady-state deformation and corresponding flow field was solved using the in ENSOLV implemented static aeroelastic solver.

From this section on, convergence plots are omitted to avoid an overload of figures. The pressure and velocity plots are displayed to show the effect of the deformations on the flow field around the blade. Subsequently, the loads in undeformed and deformed are compared to provide insight in the aeroelastic coupling of this blade.

FLOW AND PRESSURE PLOTS

Flow around the deformed blade is visualized by similar plots as shown in the rigid case. The greatest part of the blade experienced similar flow conditions. It was evident that flow separation occurred at the cylindrical section shown in figure 5.10a. The largest difference in the flow characteristics can be observed at the tip. At $z/R = 0.90$ shown in figure 5.7c, it can be noticed that the suction peak was smaller and the stagnation point ($C_p = 1$) was located closer to the leading edge, indicating an angle of attack reduction. Similar as for the rigid case, the remaining velocity and pressure plots are given in appendix D.
As shown in figure 5.17, the limiting streamlines on the deflected surface were roughly similar to the undeflected case. The deformation of the blade did not influence the onset of flow separation, which is obvious as negative torsion leads to lower angles of attack.

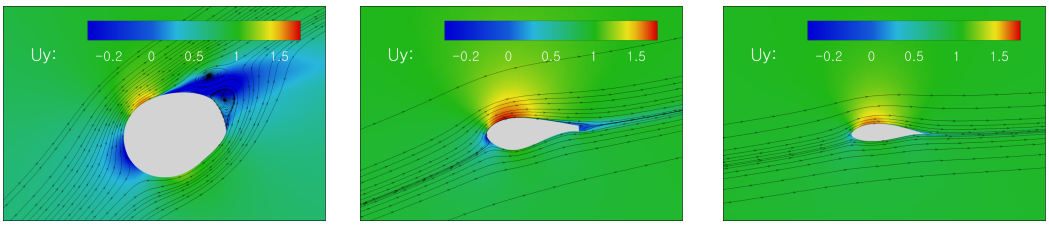

(a) $z/R = 0.12$ (b) $z/R = 0.31$ (c) $z/R = 0.90$

Figure 5.10: Streamlines and velocity in y-direction at several spanwise cross-sections ($U_\infty = 11.5$ m/s)

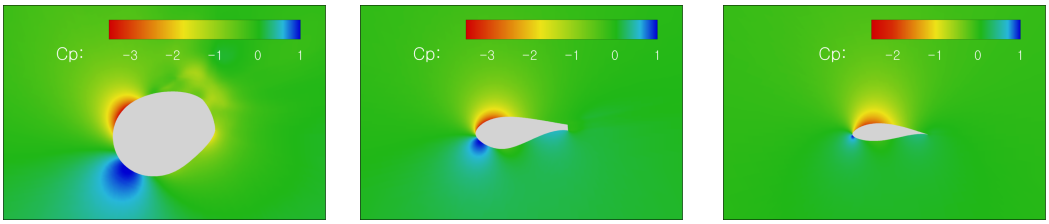

(a) $z/R = 0.12$ (b) $z/R = 0.31$ (c) $z/R = 0.90$

Figure 5.11: Contour plots of pressure at several spanwise cross-sections ($U_\infty = 11.5$ m/s)

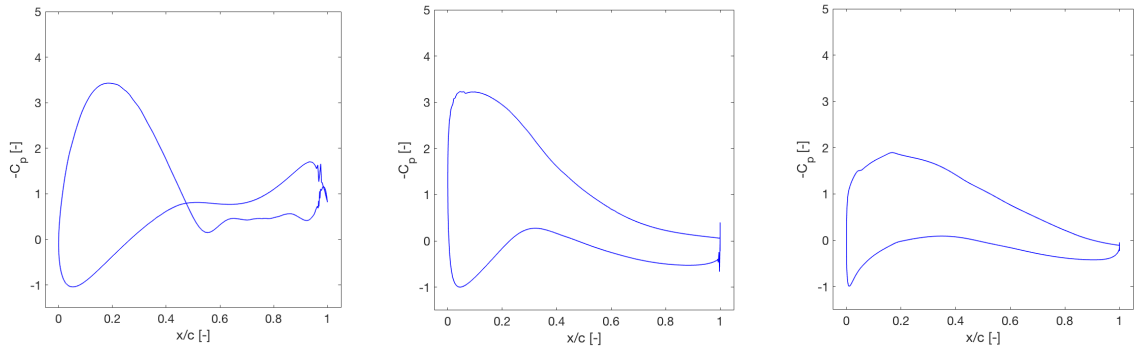

(a) $z/R = 0.12$ (b) $z/R = 0.31$ (c) $z/R = 0.90$

Figure 5.12: Pressure distribution at several spanwise cross-sections (U_∞ = 11.5 m/s)

FSI ITERATIONS

As described in the methodology, the aeroelastic solver includes a linear structural model. The pre-stressed linear stiffness matrix was incorporated to solve equations governing static aeroelastic analysis. Due to linear characteristics of the structural model, it was assumed that the structure adopted its final shape after the flow was converged. Figure 5.13 and 5.14 shows the displacements in the three main directions after convergence within a threshold of 0.1% of the final displacement. The results showed a tip displacement of 16 meters, which corresponds to 15% blade radius. It may be expected that structural nonlinearities affect the steady-state solution. Furthermore, some valuable insights were derived from the results. As known from the methodology, in linear analysis the deformations are pointed in similar direction as applied loads. Figure 5.14a confirmed this event, showing that the tip displaced radially outward relative to the initial state. The blade was elongated due to applied loads. This artificial effect increased the effective rotor area, resulting overestimation of rotor performance. In reality, higher-order terms included in nonlinear models cause geometric couplings. Independently of material effects, bending would displace the tip radially inward causing a reduction in effective rotor area. Additionally it was shown that the aerodynamic loads resulted in a large tip torsion. The negative values imply that the leading edge of the blade was twisted into the wind. This elastic effect was incorporated to alleviate loads for heavier wind conditions. This effect is clearly visible in figure 5.15. The flapwise- and edgewise forces were substantially reduced due to deformations.

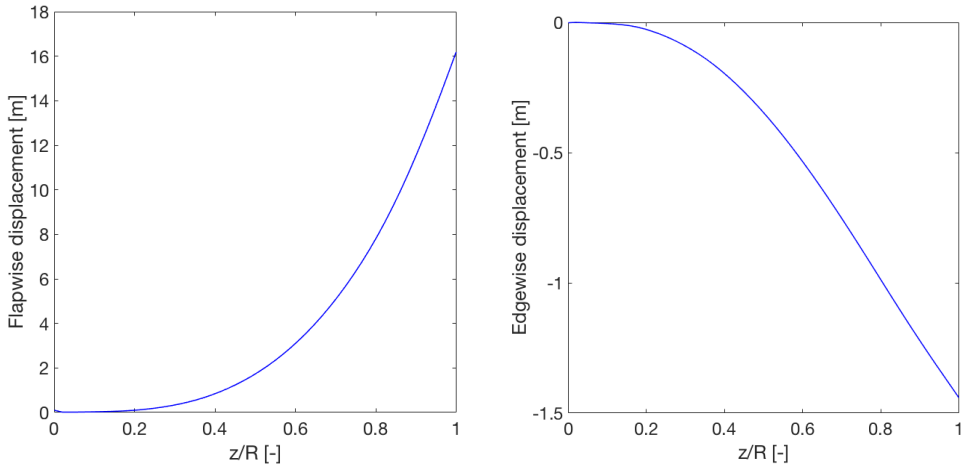

(a) Flapwise displacements (b) Edgewise displacements

Figure 5.13: Structural displacements of the linear deformed blade for U_∞ = 11.5 m/s

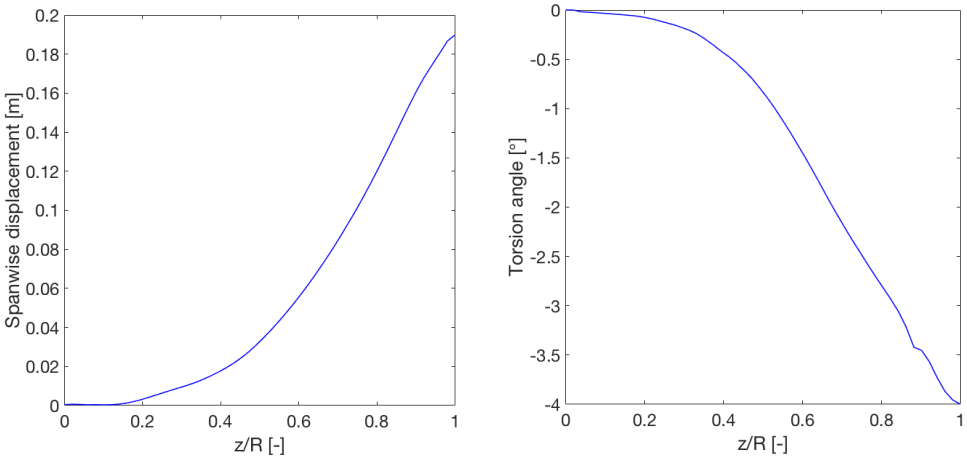

(a) Spanwise displacements

(b) Torsion angle

Figure 5.14: Structural displacements of the linear deformed blade for U_∞ = 11.5 m/s

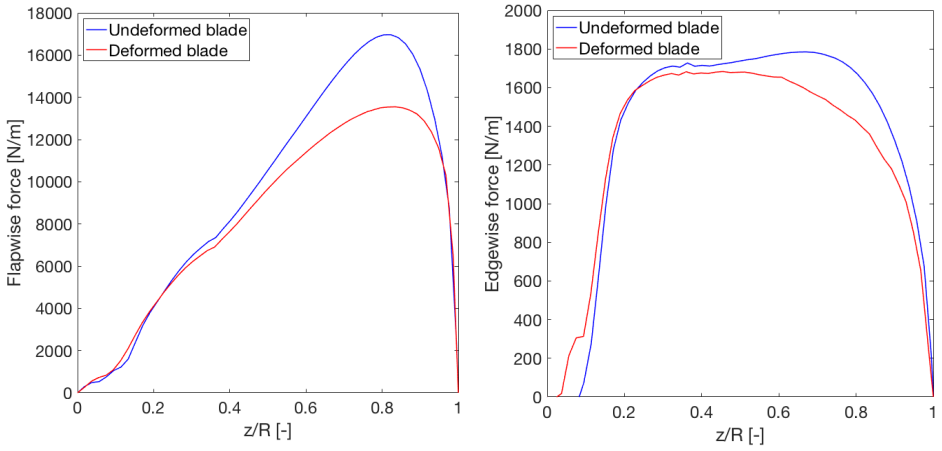

(a) Flapwise forces over the blade

(b) Edgewise forces over the blade

Figure 5.15: Comparison of the aerodynamic forces over the rigid and linear deformed blade for U_∞ = 11.5 m/s

BUCKLING ANALYSIS

The next step would be to perform a fully-nonlinear FSI iteration in order to evaluate the effects of structural nonlinearities on static deflection. As explained in the methodology, the forces obtained from semi-nonlinear aeroelastic analysis were mapped on the full structural model. Subsequently the nonlinear computations were performed. Numerous efforts were conducted to perform the static analysis, but the solution did not converge. Regardless of the solver settings, the solution started diverging at approximately 60% of the total load. It appeared that the deformations led to local defects of shell elements. The area of deteriorated cells was located at approximately 90 meters span at the suction side of the blade. It appeared that the grid defects were caused by large incremental rotations between successive shell elements. These numerical instabilities seemed to have a physical cause. Due to a reduction in local stiffness, local buckling occurred. Subsequently, a linear buckling analysis was conducted to investigate these event. The buckling analysis was performed in `Nastran` using the SOL105 solution procedure. Notice that a linear analysis was executed. Therefore only a geometrical stiffness correction was performed based on small displacements. Besides, the results only provide an overview of the buckling modes (i.e. eigenvectors) and associated load factor (i.e. eigenvalues). As buckling modes are generalized vectors, they do not present actual displacements and stresses. Hence, the results do not contain information about the severeness of the instability. The results are shown in table 5.4. As buckling often leads to structural failure, only the first five modes were given. It can be seen that the first buckling mode has a load factor of approximately 0.42. It seemed that the load factor is significantly smaller than the value at which the nonlinear static analysis failed to converge ($\approx$ 0.4 and $\approx$ 0.6 of the total

load respectively). This is a result of nonlinear effects. Due to the iterative solution process, shell elements in close proximity of the buckling region, adopted some of the stresses, causing alleviation of the defected elements.

Mode number	Buckling load factor λ
1	0.4208
2	0.4213
3	0.4264
4	0.4268
5	0.4581

Table 5.4: Overview of the first five buckling modes for $U_\infty = 11.5$ m/s

Figure 5.16 shows the location of the first buckling mode. As shown high compressive stresses occurred in the particular region. The two vertical black lines are located at 90 and 93 meters span. As the thickness of the material decreases towards the tip, it can be stated that material stiffness's are relatively low. As a consequence further stiffness reduction led to local buckling

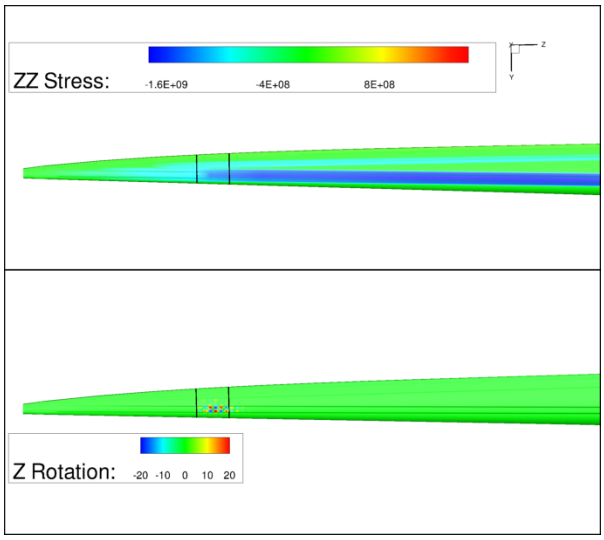

Figure 5.16: An overview of the compressive stresses (in Pa) and buckling effects (visualized by the Z rotation of elements in degrees) on the suction side of the blade. The vertical black lines range from 90 to 93 span.

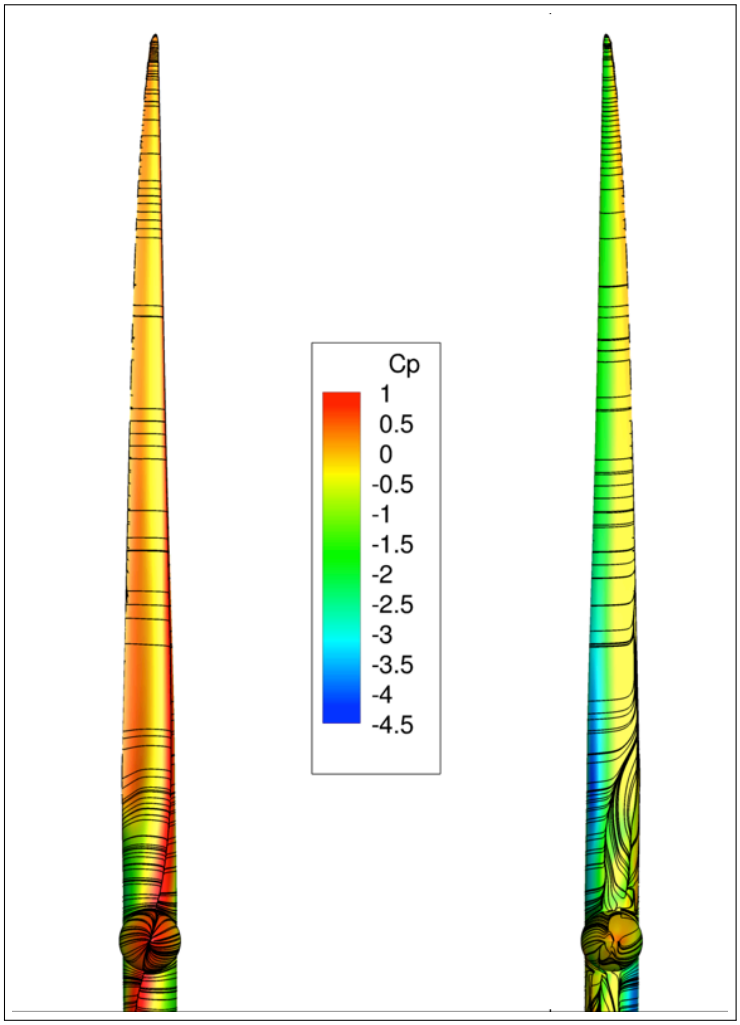

Figure 5.17: Limiting streamlines and pressure coefficient on the pressure (left) and suction (right) side of the linear deformed wind turbine blade (for U_∞ = 11.5 m/s)

5.2. LOAD CASE 2

In this section, the results from the second load case ($U_\infty = 7$ m/s) are presented. This operational condition was chosen with the expectation that the blade loads would not cause excessive buckling effects. As shown in the design curve presented in the methodology, the axial loads predicted in BEM computations were approximately halved compared to load case 1.

5.2.1. STATIC AEROELASTIC SIMULATION

For this load case, only the results from static aeroelastic analysis are discussed. First, the results from the semi-nonlinear static aeroelastic analysis performed in `ENSOLV` are discussed. Subsequently, the results from the fully nonlinear aeroelastic approach are analyzed, after which both solutions are compared.

LIMITING STREAMLINES

The limiting streamlines from figure 5.22 affirmed that the flow characteristics were similar compared to case 1. The flow over the blade was still two-dimensional and attached, except for the inboard region. The remaining velocity and pressure plots are omitted as they do not contribute to new findings or insights.

BUCKLING ANALYSIS

With the knowledge obtained from load case 1, a buckling analysis was performed prior to the sequence of aeroelastic analyses. The results obtained from linear-buckling analysis are shwon in table 5.5. Like in case 1, the load factor of the first buckling mode was beneath the critical load, which implied that buckling also occurred in the current load case. As shown in the first load case, the nonlinear structural solver is capable of exploring post-buckling behavior. Figure 5.18 shows that the compressive stresses are more than twice as low as for case 1, which explains the higher buckling load factors.

Mode number	Buckling load factor λ
1	0.8512
2	0.8589
3	0.8641
4	0.8649
5	0.9328

Table 5.5: Overview of the first five buckling modes for $U_\infty = 7$ m/s.

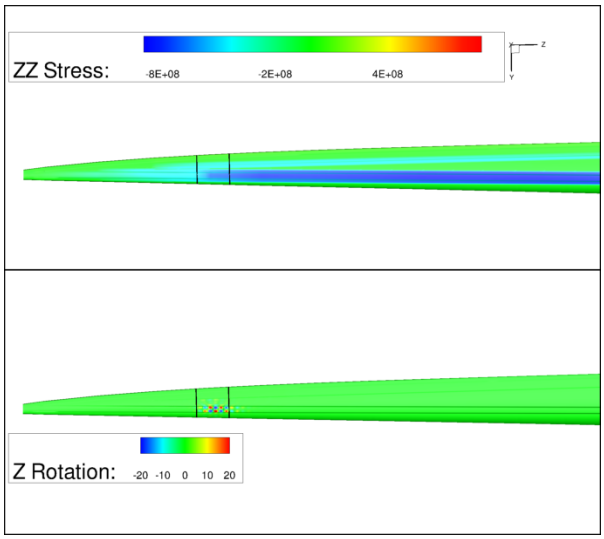

Figure 5.18: An overview of the compressive stresses (in Pa) and buckling effects (visualized by the Z rotation of elements in degrees) on the suction side of the blade. The vertical black lines range from 90 to 93 meters.

NONLINEAR DEFORMED BLADE

Despite the occurrence of buckling, it was decided to execute the nonlinear analysis. As described in the methodology, the analysis compromised of a manually performed coupling between ENSOLV and Nastran. The forces derived from the semi-nonlinear static aeroelastic approach were applied as initial condition in order to speed up convergence. The analysis results showed that a converged solution was obtained. Consequently, the displacements were interpolated to the aerodynamic mesh, after which the mesh could be deformed and a steady CFD analysis was performed. The results showed that the aerodynamics loads hardly changed as shown in figure 5.21. Therefore, the performance of additional two-way iteration was omitted as it was supposed that the solution would not significantly change. In figure 5.19 and 5.20 the displacements in several degrees of freedom are displayed. Additionally, figure 5.23 provides rendering of both deformed blade shapes. The differences in flapwise and edgewise displacements are clearly visible, where the largest deviation existed for the flapwise displacements as expected. The discrepancy in flapwise and torsional deformation were mainly caused by follower-force effects. Due to bending of the blade, the orientation of centrifugal forces relative to the blade axis changed, causing a restoring bending moment. This moment opposed the aerodynamic forces alleviating the magnitude of displacements. More importantly, a torsional moment was created due to the aft location of the mass centre relative to the shear centre line of the blade. Although the torsional deformations reduced, it resulted in higher loads as a consequence of larger angles of attack. For this load case, only a tip torsion of 0.27° was observed, causing only a minimum change in aerodynamic loads. It is expected that torsional deformation becomes larger and the discrepancy between the deformations increase. As already expected, the displacements in spanwise direction changed sign. Higher-order geometric terms led to spanwise displacement due to bending. The linear deformed blade was almost 0.5 meters longer than the nonlinear deformed blade. Since the discrepancy in spanwise displacements comprised 0.5 meter, it was expected that the difference did not lead to significant overestimation of thrust and torque. Furthermore, the results showed that the edgewise displacement were differently distributed along the blade. This effect was a result of changing stiffness. In the region where local buckling occurred, the stiffness reduced resulting in higher displacements. It can be concluded that structural nonlinearities did not affect the steady-state solution for this load condition. However, the nonlinear effects are clearly visible and are expected to lead to an increasing deviation of deformations for heavier load cases. For comparison, the semi-nonlinear static approach computed a tip torsion of 4° for the first load case, which is almost twice as large as in this case. Therefore it can be concluded that for heavier wind conditions linear structural modelling is not sufficient to solve static aeroelastic problems for concerning extreme scale wind turbines accurately.

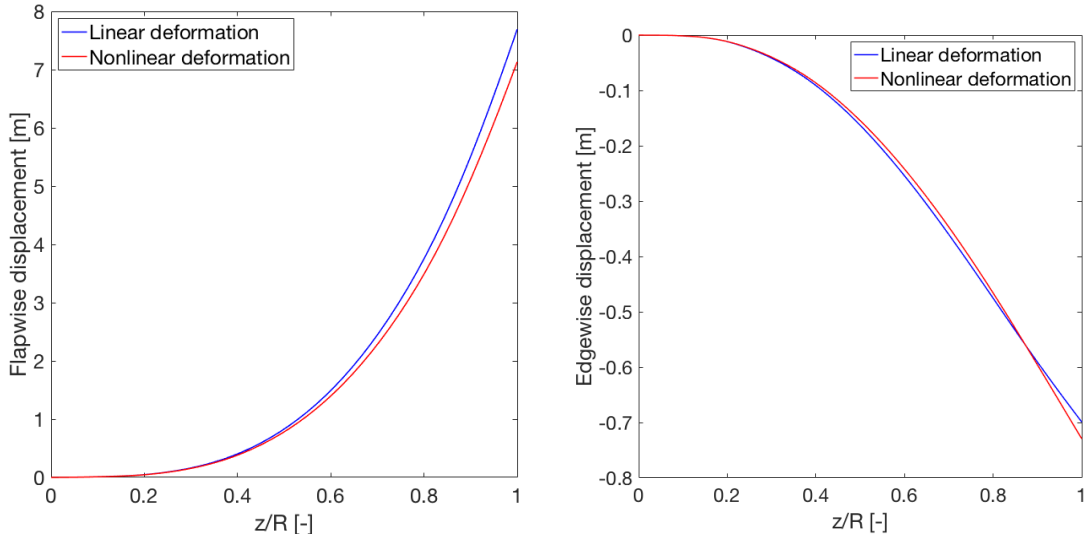

(a) Flapwise displacements

(b) Edgewise displacements

Figure 5.19: Comparison of the structural displacements of the linear and nonlinear deformed blade for $U_\infty = 7$ m/s

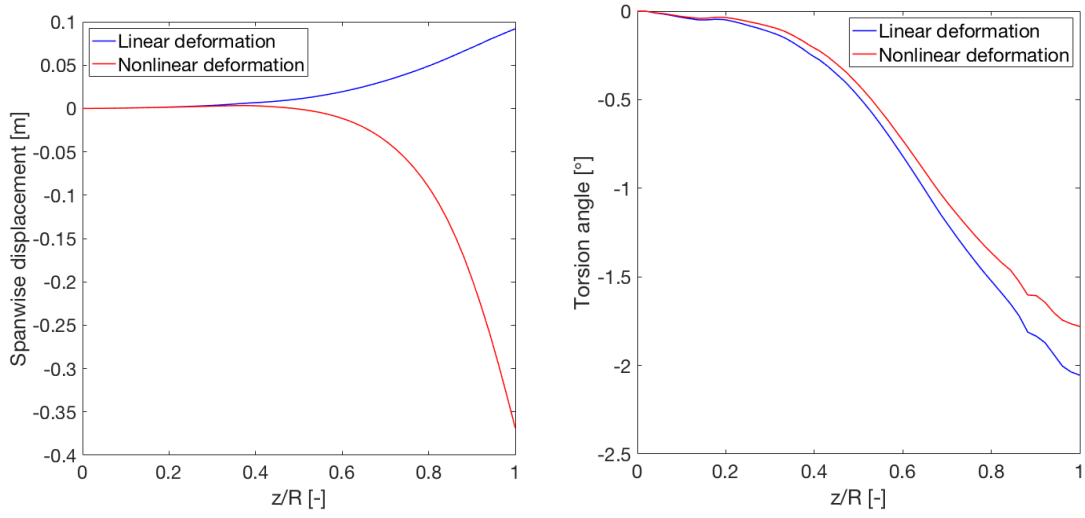

(a) Spanwise displacements

(b) Torsion angle

Figure 5.20: Comparison of the structural displacements of the linear and nonlinear deformed blade for $U_\infty = 7$ m/s

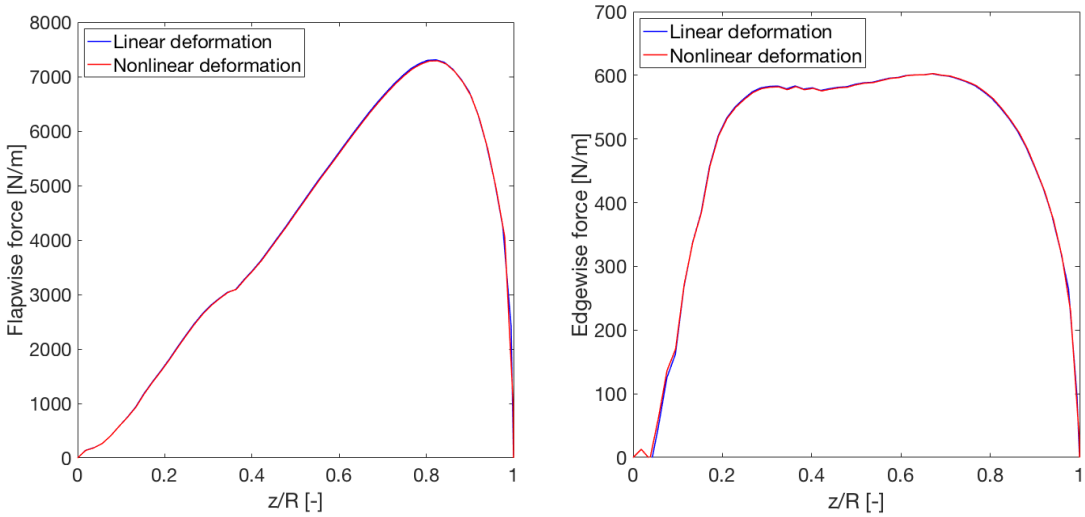

(a) Flapwise forces

(b) Edgewise forces

Figure 5.21: Comparison of force distributions along the linear and nonlinear deformed blade for $U_\infty = 7$ m/s

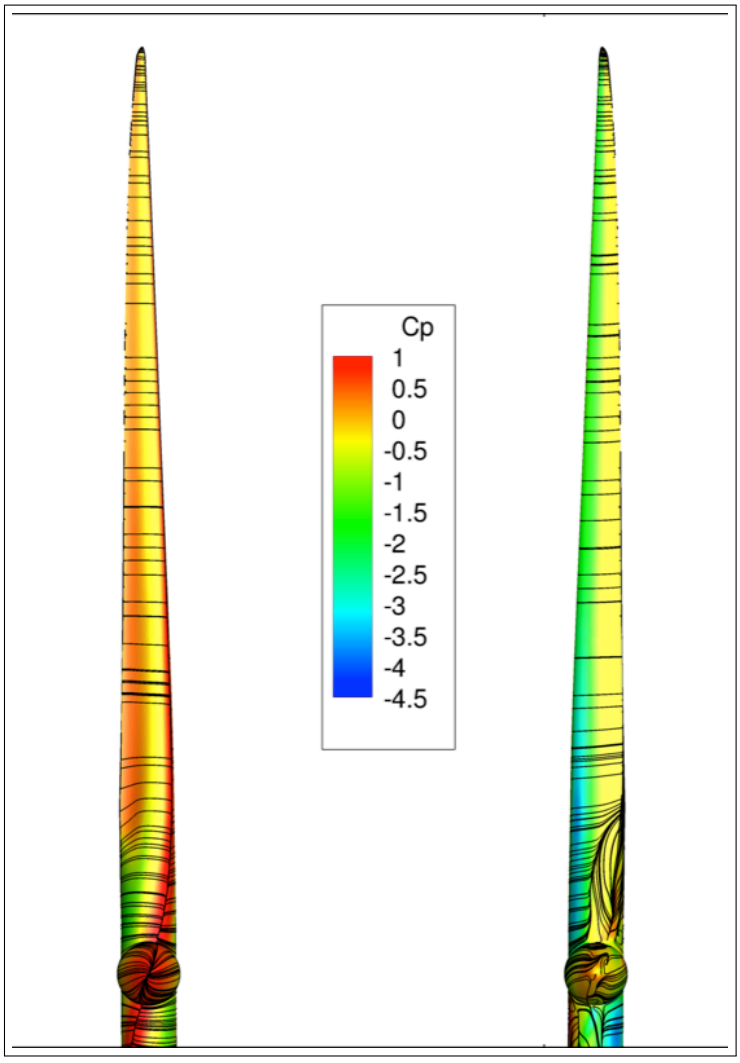

Figure 5.22: Limiting streamlines and pressure coefficient on the pressure (left) and suction (right) side of the linear deformed wind turbine blade (for $U_\infty = 7$ m/s)

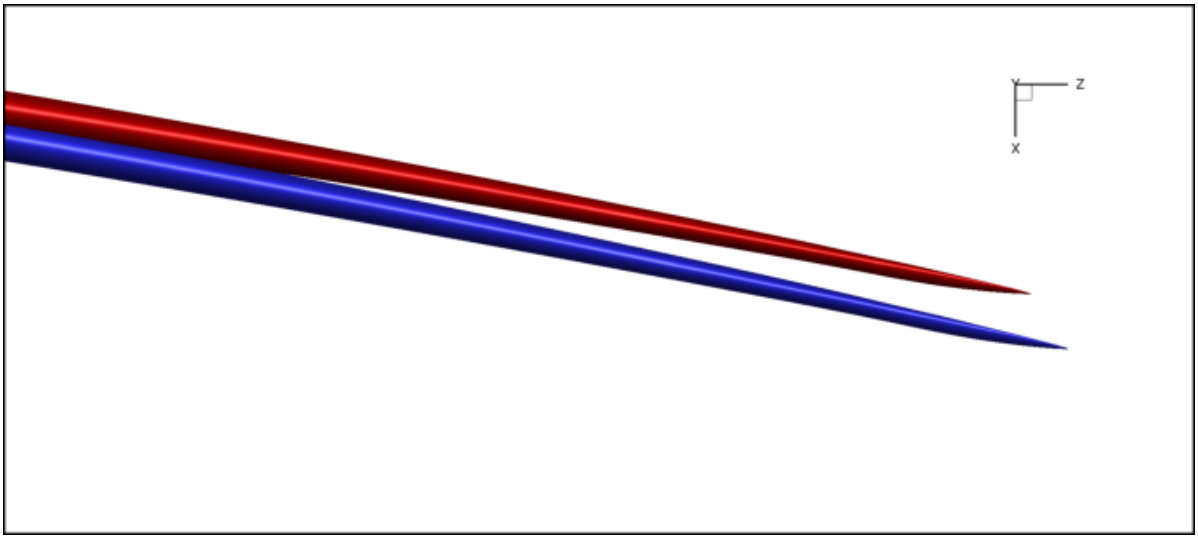

(a) Side view

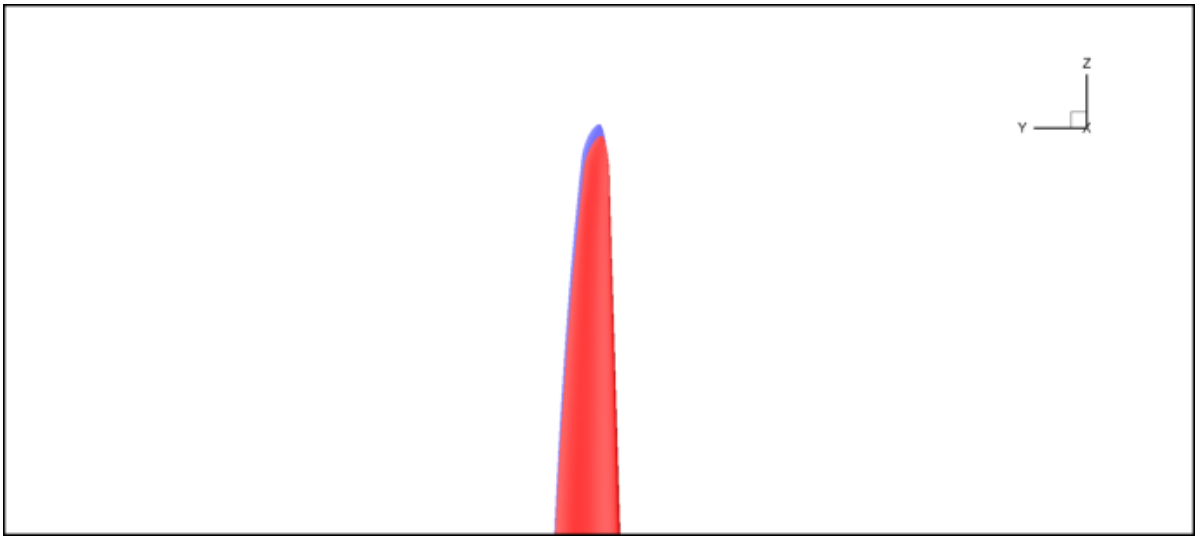

(b) Front view

Figure 5.23: A visualization of the tip displacements of the linear and nonlinear statically deformed blade.
Blue: Linear deformation: $dX_{tip} = 7.69$ m; $dY_{tip} = -0.70$ m; $dZ_{tip} = 0.09$ m; $d\phi_{tip} = -2.05°$,
Red: Nonlinear deformation: $dX_{tip} = 7.13$ m; $dY_{tip} = -0.73$ m; $dZ_{tip} = -0.37$ m; $d\phi_{tip} = -1.78°$.

5.2.2. FLUTTER ANALYSIS

In order to assess the effect of structural nonlinearities on the stability of the wind turbine, flutter analyses were carried out. To be more specific, the flutter analyses were restarted from the steady-state solution acquired from the semi-nonlinear and fully-nonlinear static aeroelastic approach respectively, using a semi-linearized approach. As already mentioned in the methodology, it was essential to include the first torsional mode to be able to predict classical flutter. Therefore, the first eight modes were included in the analyses.

It must be noted that transient simulations including forced mode vibration were performed on the coarse grid level, because this type of analysis could only be carried out in a single domain (and therefore a single node). For unknown reasons, it appeared that parallel computing did not work for these type of simulations.

As shown in the methodology, the flutter analyses were restarted from steady-state conditions. This section compares the results from "linear" and "nonlinear" flutter analysis.

MODAL ANALYSIS

Modal analysis was performed around the linear and nonlinear statically deflected structure to assess the effect of nonlinearities on the dynamic properties of the blade. The first eight eigenfrequencies were analyzed and were used in the flutter analysis. Pre-stressing effects due to initial stresses and displacements led to two distinct set of mode shapes depending on the inclusion of structural nonlinearities. Figure 5.24 shows the eigenfrequencies for different states of the blade. As shown, initial stresses had an opposing effect compared to centrifugal stiffening. Presumably, this effect is a consequence of alternation of the orientation of the force vector, causing the influence of centrifugal forces on the stiffness to be decreased. From the eigenfrequencies however, it appeared that nonlinearities did not influence the results significantly, especially for the lower mode numbers. It is of major importance to analyze the characteristic shape of the modes. Figure 5.25 and 5.26 visualize the first and sixth mode shape from the pre-stressed undeformed blade and loaded nonlinear deformed blade. It can be seen that the first mode shape remained similar, but the sixth changed. In appendix E the remainder of the mode shapes are shown. It can be concluded that the blade dynamics changed due to the inclusion of nonlinear structural effects.

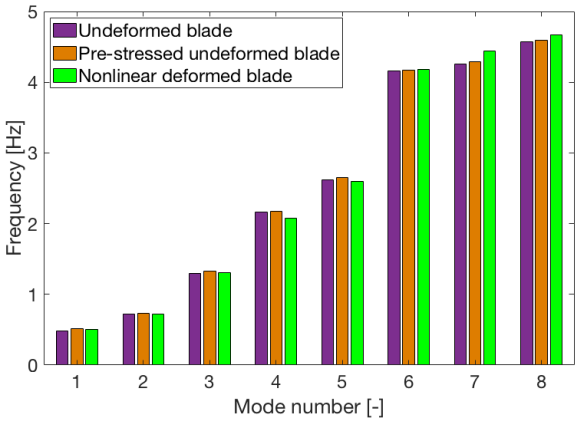

Eigenfrequencies in Hz			
Mode number			
1	0.486	0.510	0.508
2	0.725	0.729	0.718
3	1.300	1.329	1.307
4	2.171	2.173	2.075
5	2.626	2.651	2.596
6	4.205	4.175	4.168
7	4.304	4.290	4.439
8	4.676	4.595	4.673

Figure 5.24: The first eight eigenfrequencies for the undeformed blade with and without stiffening effect, and the nonlinear deformed blade subject to rotational and aerodynamic forces

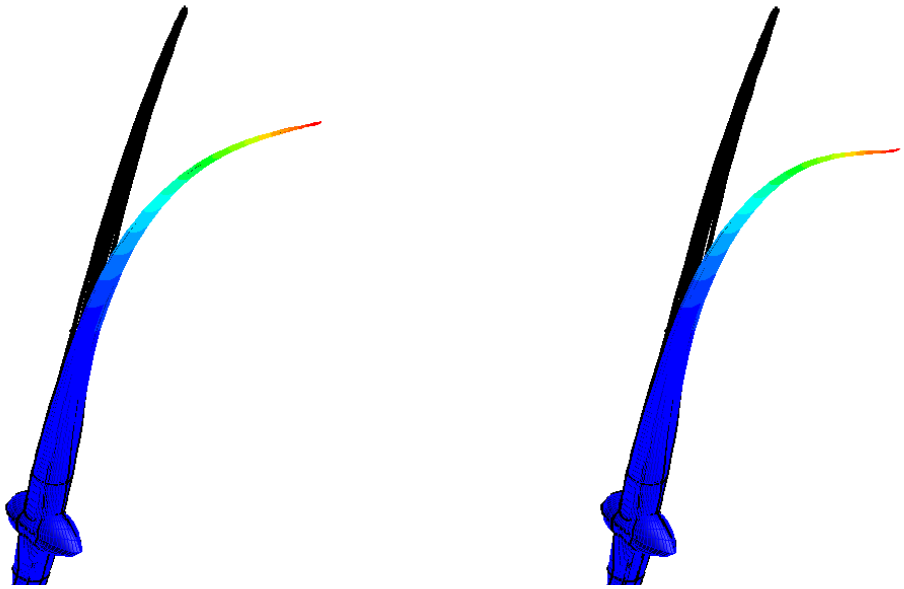

Figure 5.25: First mode shape; **Left**: Φ_1^L, f = 0.510 Hz; **Right**: Φ_1^{NL}, f = 0.508 Hz

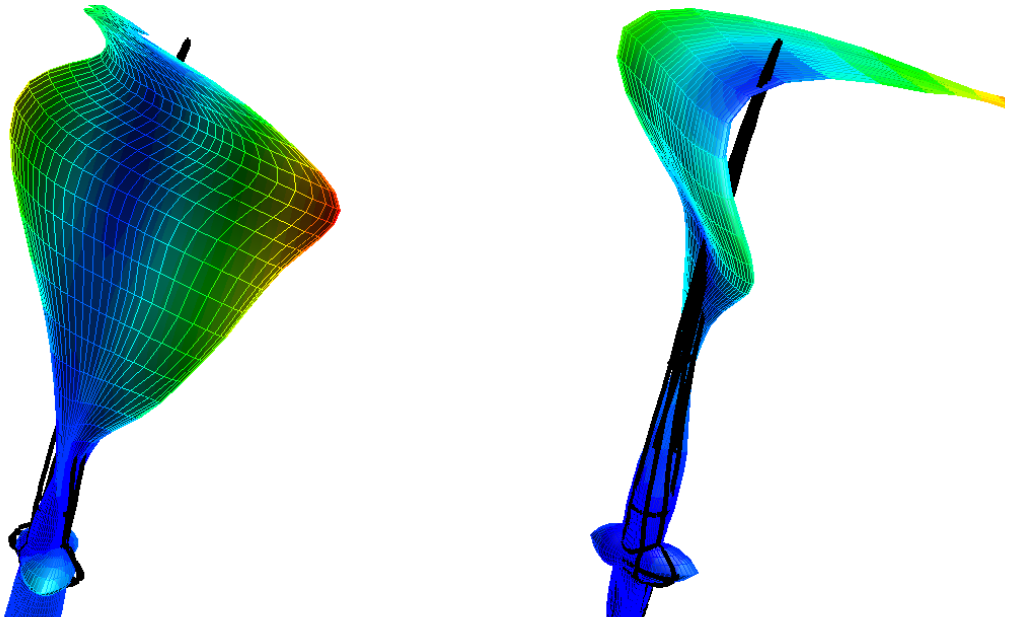

Figure 5.26: Sixth mode shape; **Left**: Φ_6^L, f = 4.175 Hz; **Right**: Φ_6^{NL}, f = 4.168 Hz

SIMULATION SET-UP

As known from the methodology, the computation of aerodynamic matrices for several reduced frequencies is necessitated in order to apply the p-k method. The reduced frequencies were selected such that they cover the eigenfrequencies of the first eight modes, while keeping the lowest reduced frequency closest to zero. The reason for that is to ensure an accurate extrapolation of the AIC's to k=0. The reduced frequencies, according to the expression used in `ENSOLV`, are k = 0.035, k = 0.070, k = 0.140, k = 0.280, k = 0.550, k = 1.100, k = 2.200 and k = 4.400. For consistency, this expression is also used in the presented results.

The choice of time step and total simulation time is based on a compromise between numerical accuracy and computational expenses. Those considerations led to a time step that agrees with 0.5 degrees rotation and a simulation time of five rotor revolutions. This entailed that, for k = 4.400. one vibration period contains 17 data points and, for k = 0.035, three vibration periods are simulated.

COMPARISON OF GRID LEVEL CONVERGENCE

As mentioned in the introduction of this section, the unsteady CFD computations were carried out on coarse grid level. In order to get a better understanding of the difference in performance of the separate grid levels, steady and unsteady CFD computations were performed on various grid levels. It must be noted that the computations were executed for the operational conditions of case 1 (i.e. U_∞11.5 m/s). Hence, the results from steady CFD are already presented at the beginning of this chapter. Table 5.6 gives an overview of the converged values of the total thrust for all grid levels. The values of the unsteady simulations were obtained by taking the average value over the last rotor revolution. The results show that the coarse grid approached the fine grid better in the unsteady computations. As concluded in the grid convergence study at the beginning of this chapter, the coarse grid was not capable of capture the unsteadiness of the flow. It can be concluded that the coarse grid would perform better in unsteady CFD analysis. However, from earlier findings it is known that appropriate grid resolution was required to predict the pressures accurately. Hence, the flutter results must be viewed critically.

Grid level	$\sum F_x$ (steady)	Difference	$\sum F_x$ (unsteady)	Difference
Fine	$2.0947{\cdot}10^6$ N	-	$2.0693{\cdot}10^6$ N	-
Medium	$1.8898{\cdot}10^6$ N	-9.78%	$1.9995{\cdot}10^6$ N	-2.95%
Coarse	$1.4740{\cdot}10^6$ N	-29.63%	$1.9423{\cdot}10^6$ N	-6.54%

Table 5.6: $\sum F_x$ evaluated at different grid levels for U_∞ = 11.5 m/s

CHECK FOR PERIODICITY

To assure an accurate solution of the flutter analysis, it was required to check if the aerodynamic responses are periodic. Transient effects, that occur after the wind turbine blade is forced into motion, need time to damp out. The periodicity of the aerodynamic responses was checked by plotting the generalized aerodynamic forces against the amplitude of the motion. Figure 5.27 and 5.28 show the plots of the following four generalized aerodynamic forces: $Q^L_{1,1}$, $Q^{NL}_{1,1}$, $Q^L_{6,6}$ and $Q^{NL}_{6,6}$. The plots contain the generalized aerodynamic forces for different values of k. Since the last period of the aerodynamic responses was used to compute the AIC's, the latter responses were plotted.

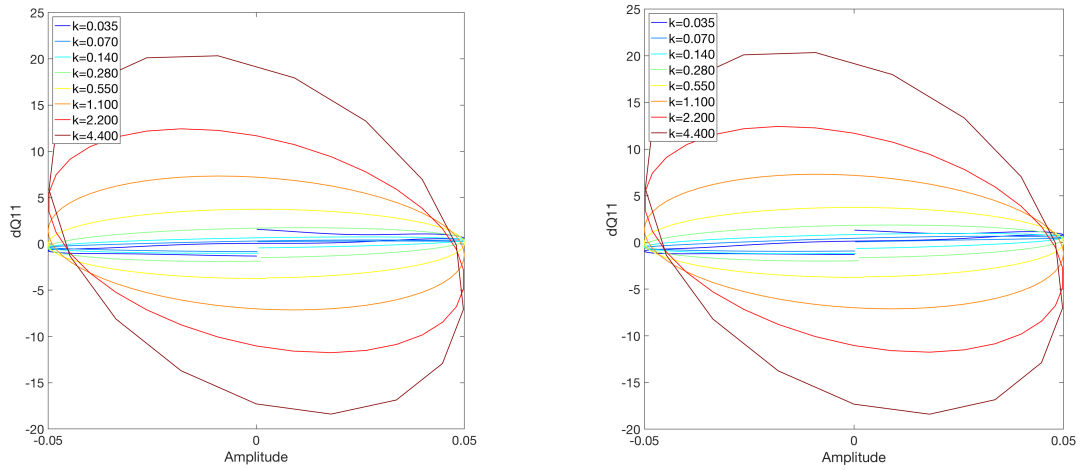

Figure 5.27: The "periodicity" plots of the generalized aerodynamic forces of the first flapwise bending mode; **Left**: Around linear structure, **Right**: Around nonlinear structure.

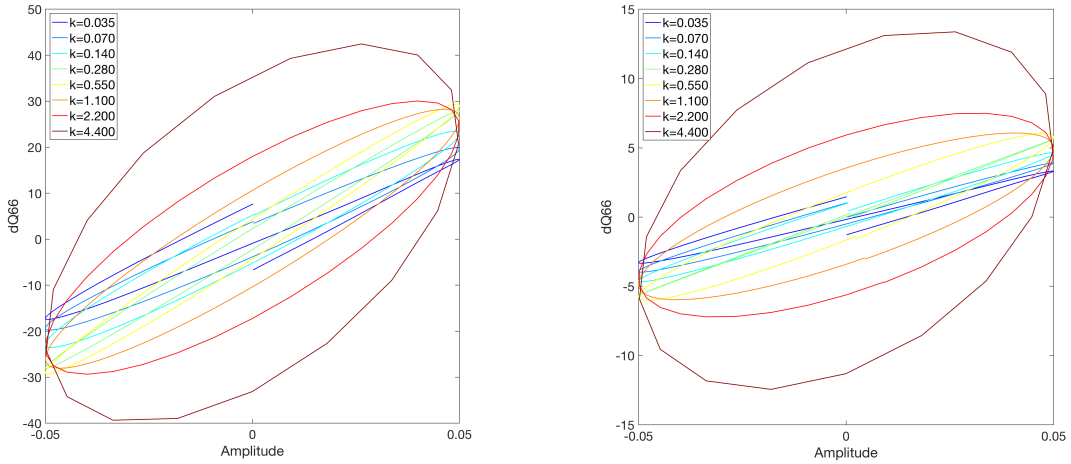

Figure 5.28: The "periodicity" plots of the generalized aerodynamic forces of the first torsion mode; **Left**: Around linear structure, **Right**: Around nonlinear structure.

The results showed that for high-frequency vibrations, the aerodynamic responses took on the form of an hysteresis. The closed shape of the aerodynamic responses indicated that the flow solution converged to a periodic response. However, for low values of k, periodicity was not reached. Due to the limited computation time, the transient effects did not have the opportunity to damp out. Since the transient effects were small, it was expected that the transient effects would not affect the aerodynamic influence coefficients considerably. To check this, a correction was proposed that should filter undesired transient effects. Apart from the periodicity check, additional conclusions can be drawn from the "periodicity" plots. In figure 5.28 it is clearly visible that the amplitude of the "nonlinear" response was substantially smaller compared to the "linear" response. Additionally, the hysteresis adopted a different shape, implying a change in shift. The sixth mode from both mode sets behaved substantially differently. A more complete overview of the "periodicity" plots can be found in appendix F.

CORRECTION MODEL

The "periodicity" plots from the previous section showed that, especially for low k values, the aerodynamic responses were not yet periodic. Therefore, a correction was applied to the aerodynamic responses, before computing the AIC's. In order to avoid an overflow of figures, only the aerodynamic responses around the "linear" structure are shown. The response plots in figure 5.30 demonstrate that the transient effects develop in a similar pattern. The correction model is based on an approximation method that can imitate the transient behavior. Two distinct approximation methods were used depending on the value of k:

a) **Conventional approximation method (high values of k)**: Transient effects were approximated by an average of two cubic Hermite splines that interpolate the local maxima and minima of the aerodynamic response (shown by the green line in figure 5.29a). For low-frequency vibrations, the conventional correction method had difficulty finding local extremes towards the end of the simulation. This led to a polynomial that does not follow the transient effect correctly as can be seen in figure 5.29a, even leading to more pronounced errors. To resolve this, an alternative approximation method is used for the lowest two k values.

b) **Alternative approximation method (lowest two values of k)**: The cubic spline function is built up using the first data point of each aerodynamic cycle. The phase between imposed motion and aerodynamic response is computed in the last vibration period, after which the phase is used to find the first data point of the aerodynamic response. 5.29b shows that this method delivers a better representation of the transient effects.

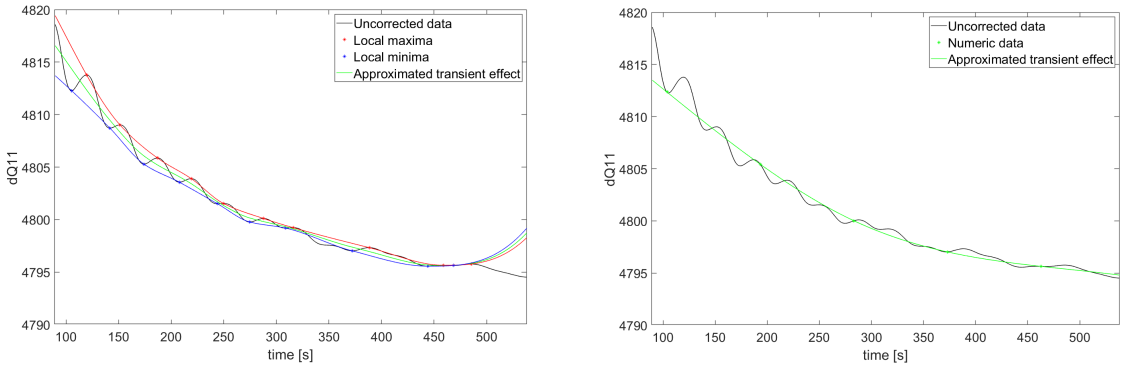

(a) Conventional approximation method

(b) Alternative approximation method

Figure 5.29: The working of both approximation methods, applied on Q_{11} for k=0.070

The approximated transient effect was subtracted from the aerodynamic responses, resulting in the modified aerodynamic responses. The dotted lines in figure 5.30 represent the approximated transient effect. After subtraction of the transient effect, the corrected aerodynamic responses were obtained. The corrected data shown in figure 5.31 displays that the response still contained higher harmonics. Since Low-frequency vibrations influenced the flow less severely, the error caused by convergence issues was more significant. However, it was expected that applied correction reduced the existing error sufficiently.

AERODYNAMIC INFLUENCE COEFFICIENTS

Determination of the AIC's was executed by computing the transfer function using FFT as explained in the methodology. Only the last period of the aerodynamic response was used in order obtain the most accurate AIC's. The same steps were executed for the analysis around the linear and nonlinear structure. Prior to comparing the results from both flutter analyses, the effect of the correction was analyzed. Only the diagonal aerodynamic influence coefficients are presented in figure 5.32 and 5.33 to avoid an overload of figures. It is evident that the modes coupled through aerodynamic forces. Moreover, flapwise bending and torsional modes incorporated a strong coupling as expected.
The dots (generally positive) represent the modal aerodynamic stiffness and the crosses (generally negative) represent the modal aerodynamic damping coefficient. It is clearly visible that the applied corrections mainly impact the aerodynamic influence coefficients for low k values as expected. The results show that outliers (especially for the fourth mode shape) disappeared, which indicates that the error induced by transient effects, was successfully reduced.

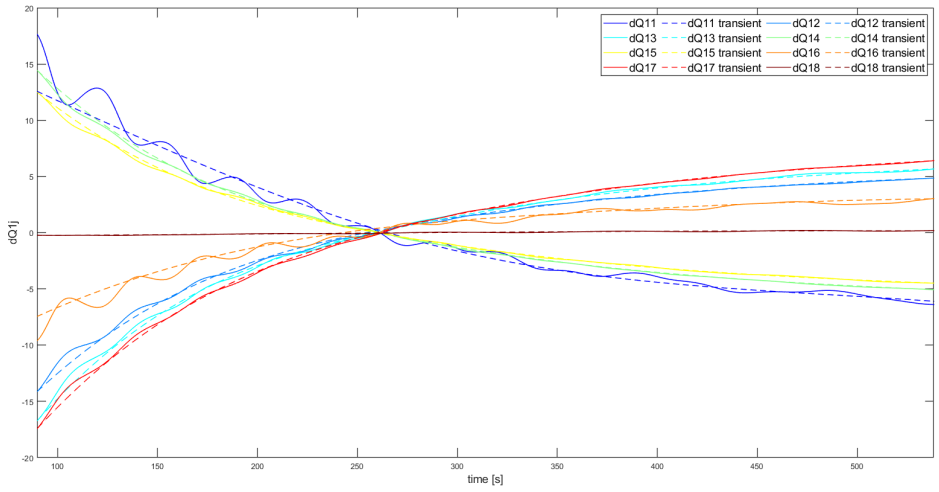

(a) k=0.070

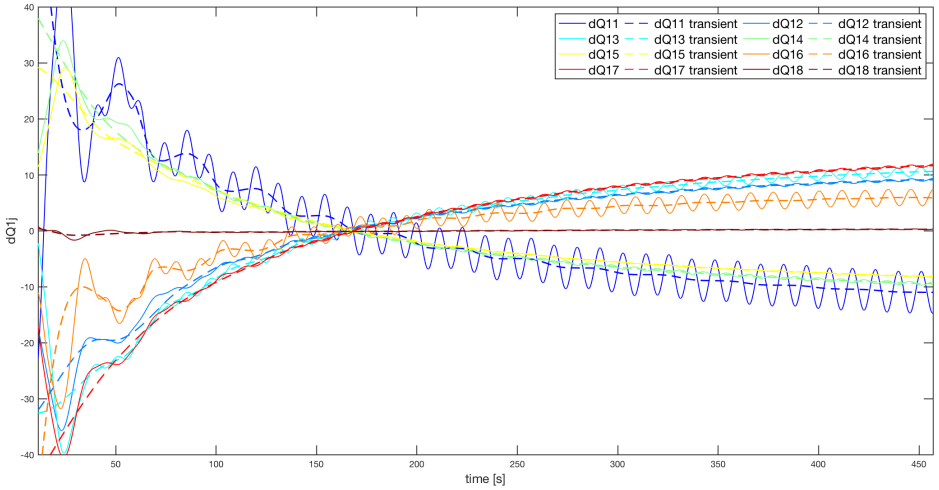

(b) k=0.550

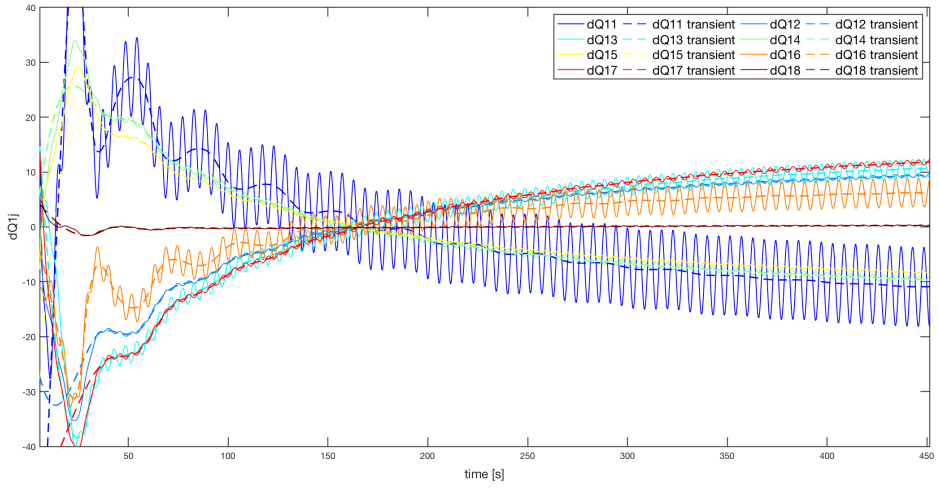

(c) k=1.100

Figure 5.30: *Line*: Aerodynamic response in time of separate mode shapes to excitation of the first mode shape; *Dotted line*: Interpolated transient part of aerodynamic response

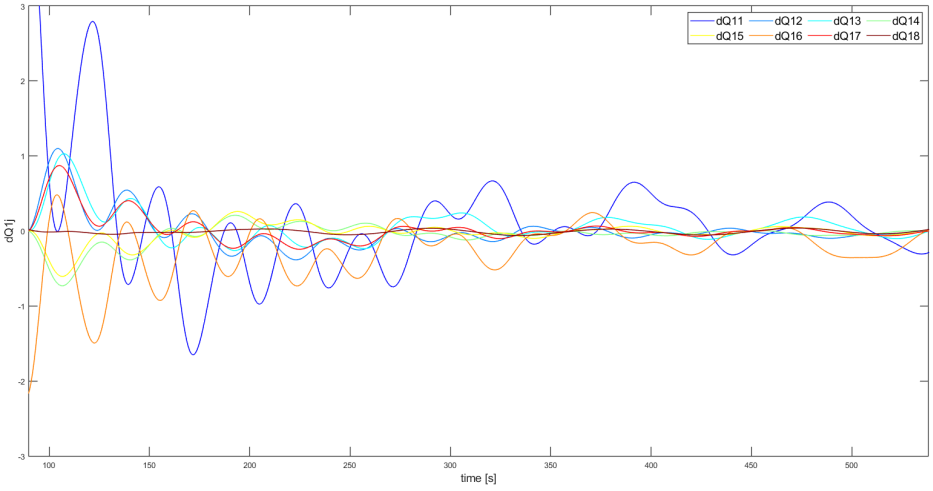

(a) k=0.070

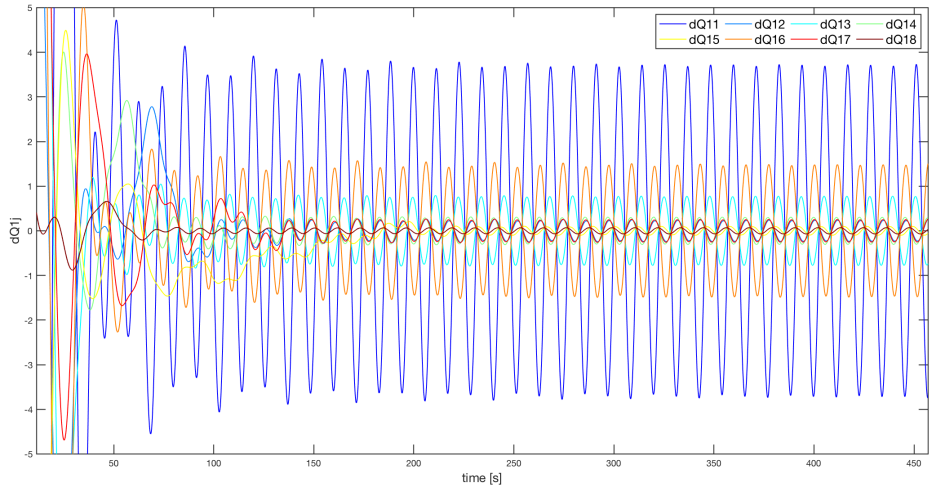

(b) k=0.550

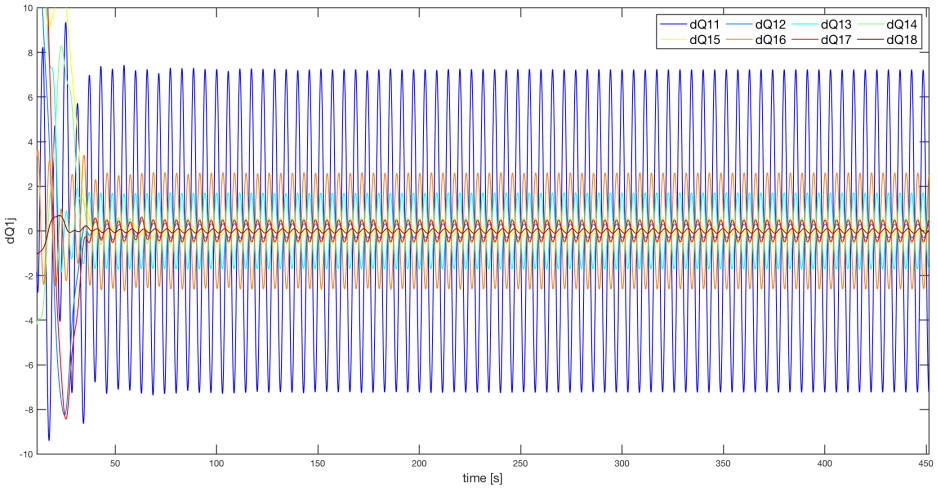

(c) k=1.100

Figure 5.31: Corrected aerodynamic response in time of separate mode shapes to excitation of the first mode shape; Last period is used in determining the aerodynamic coefficients

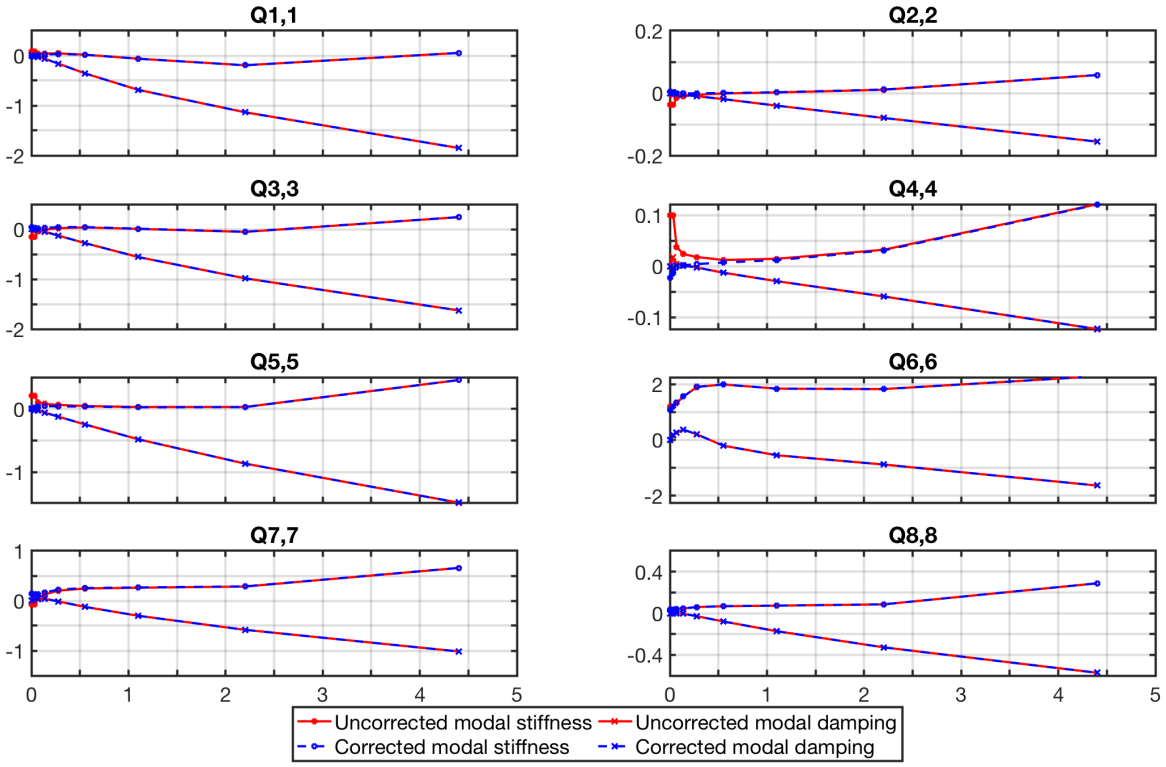

Figure 5.32: *Linear case:* Corrected vs uncorrected diagonal aerodynamic influence coefficients

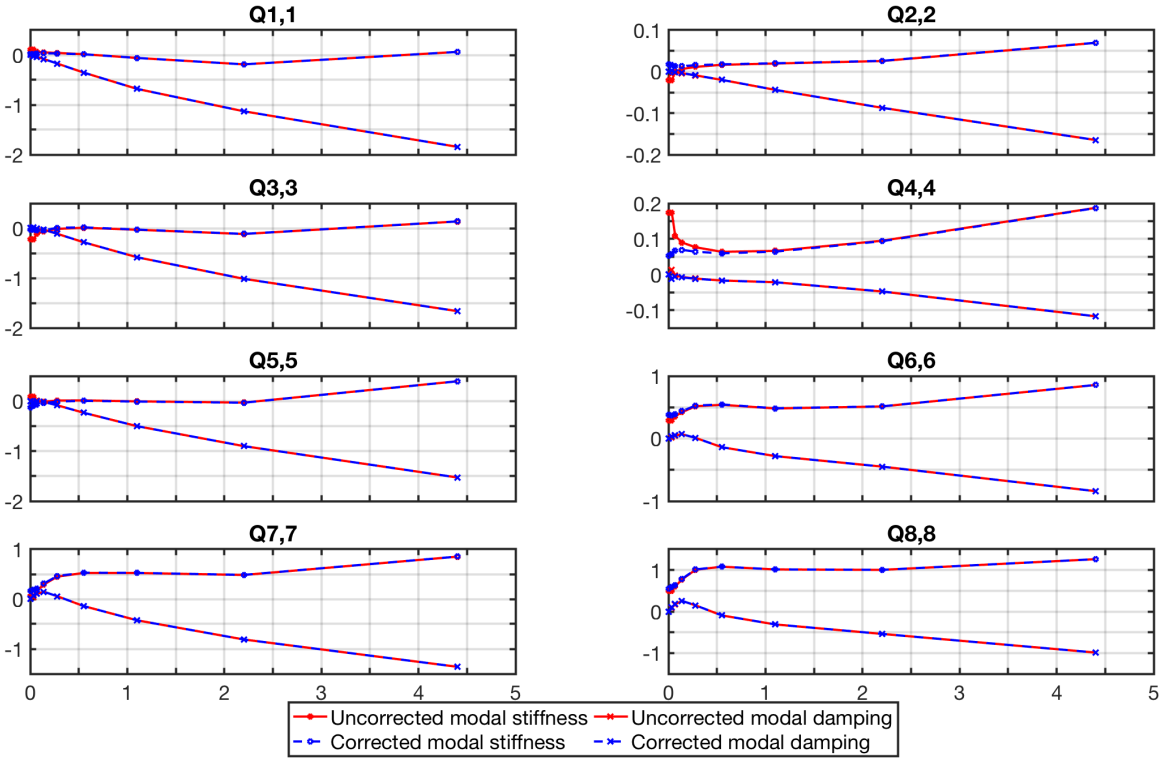

Figure 5.33: *Nonlinear case:* Corrected vs uncorrected diagonal aerodynamic influence coefficients

EFFECT OF NONLINEARITIES ON AERODYNAMIC RESPONSE

The corrected response data from both flutter analyses can be seen in figure 5.34. It shows the AIC's versus the reduced frequency. The results showed that the aerodynamic responses of the first three mode shapes are identical as expected from the modal analysis results. Furthermore, the AIC's confirmed that the first torsional mode has shifted from the sixth mode, Φ_6^L, to the eighth mode, Φ_8^{NL}. However as can be seen in appendix E, the mode ϕ_8^{NL} coupled with bending mode. Due to the change of characteristic shape, the AIC's substantially changed.

Evidently, the flow around the blade is highly sensitive to torsion as the angle of attack changes. Without prior knowledge about the mode shapes, the torsional modes could be easily identified due to their high positive values of the modal aerodynamic stiffness. Notice that for $k = 0$, the aerodynamic modal stiffness coefficients of the latter had positive values. However for $k = 0$, steady-state aerodynamics must be considered. The nonzero coefficients could lead to inaccuracies in the flutter analysis. To avoid this, it can be chosen to compute the aerodynamic matrices for more values of k. In this study however, it was not feasible to perform additional simulations. Analyzing the "nonlinear" aerodynamic influence coefficients, the increased modal aerodynamic stiffness coefficients of Φ_4^{NL}, Φ_6^{NL}, Φ_7^{NL} and Φ_8^{NL} indicated that the mode shapes consist of a torsional component. This means that the change in dynamic characteristics leads to an alteration of the aeroelastic characteristics, which may affect the stability characteristics of the blade. Note that the edgewise bending modes (Φ_2 and Φ_4) are aerodynamically worse damped, which confirms findings from literature (see section 2.1.1). Inclusion of torsional deformation may lead to diverging behavior of the respective modes.

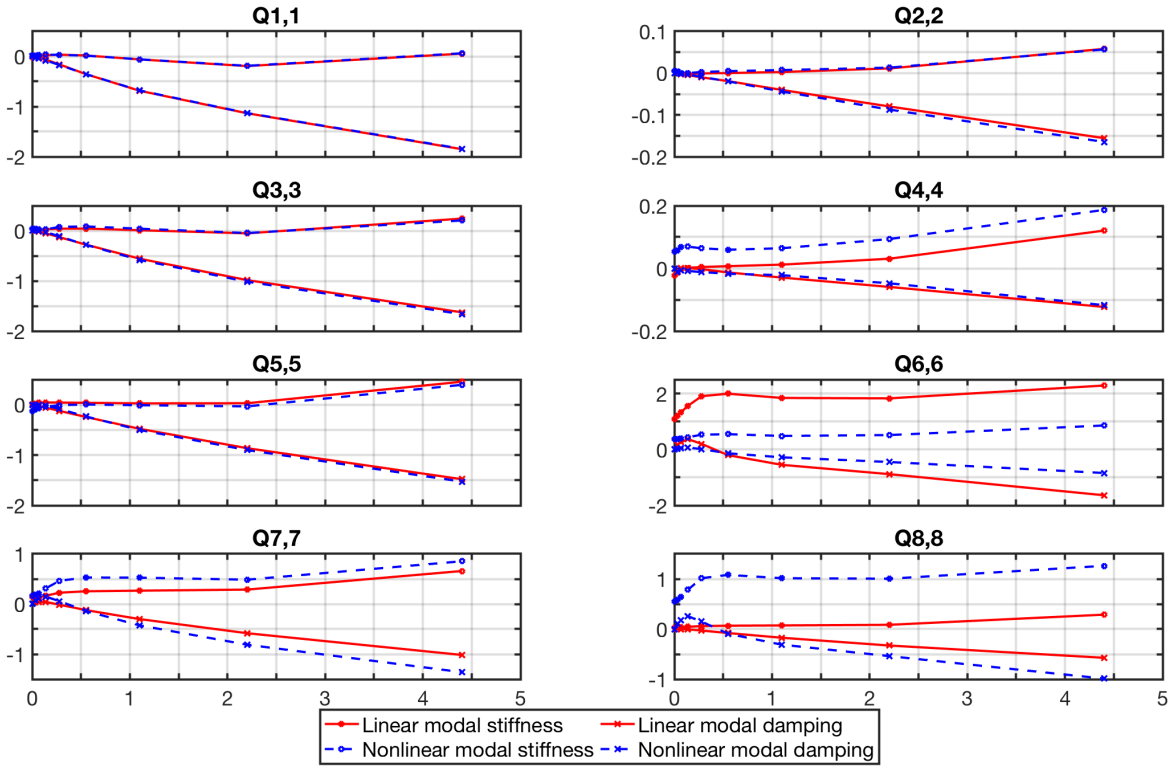

Figure 5.34: Comparison of the corrected diagonal aerodynamic influence coefficients

FREQUENCY AND DAMPING PLOTS

The frequency and damping characteristics of the blade were obtained by the p-k method as described in methodology. In this work only the solution using the corrected AIC's is shown to avoid an overload of figures. However, the "uncorrected" solutions are presented in appendix G. From those plots, it can be seen that frequency and damping plots were not significantly affected by the applied correction. On the contrary, it can be concluded that the convergence did not lead to major inaccuracies.
The frequency and damping plots obtained from the corrected AIC's are presented in figure 5.35 and 5.36. Both flutter results showed that no flutter occurred. As shown in the damping plots, the majority of the mode shapes were stable over the full solution domain. The flapwise bending modes were even strongly damped, avoiding proclivity to flutter. Additionally, both diagrams show that the frequency of the sixth mode shape changed considerably. Since the mode shapes in proximity of the sixth mode shape had considerably lower frequencies, no modes-coupling occurred. At higher flow velocities however, the torsional modes seemed to lead to diverging behavior as it can be seen that they deflect towards the flutter boundary. As a result of higher AIC's, this effect on the "linear" torsional was more pronounced. The results show that structural nonlinearities led to the loss of the pure torsional mode, resulting in more stable behavior of the latter. On the contrary, the edgewise bending modes (mode 2 and 4) became unstable due to inclusion of torsion. As known from literature review, edgewise bending modes are poorly damped and could therefore be prone to instabilities.
Given the assumptions the p-k method is founded on, the results were not a realistic representation of the actual operational conditions. Since the p-k method is based on the principle of linear aerodynamics, the flow conditions over the blade must be the same. The set of AIC's do not account for nonlinear flow effects. For wind turbines, this requirement implies that the tip speed ratio of the the wind turbine must remain the same as the local flow conditions depend on wind flow velocities and flow velocities induced by rotational motion. As shown in the design curve given in the methodology, the tip speed ratio can be assumed constant between cut-in speed, $U_\infty = 3$ m/s, and $U_\infty = 9$ m/s. Above $U_\infty = 9$ m/s, curve representing the rotor speed decreases, after which the rotor speed adopts a constant value as of $U_\infty = 12$ m/s. Additionally, the static state of the blade depends on the considered operational condition. Lastly, the dynamic properties of the blade change over the operational envelope as shown in the results of static aeroelastic analysis.

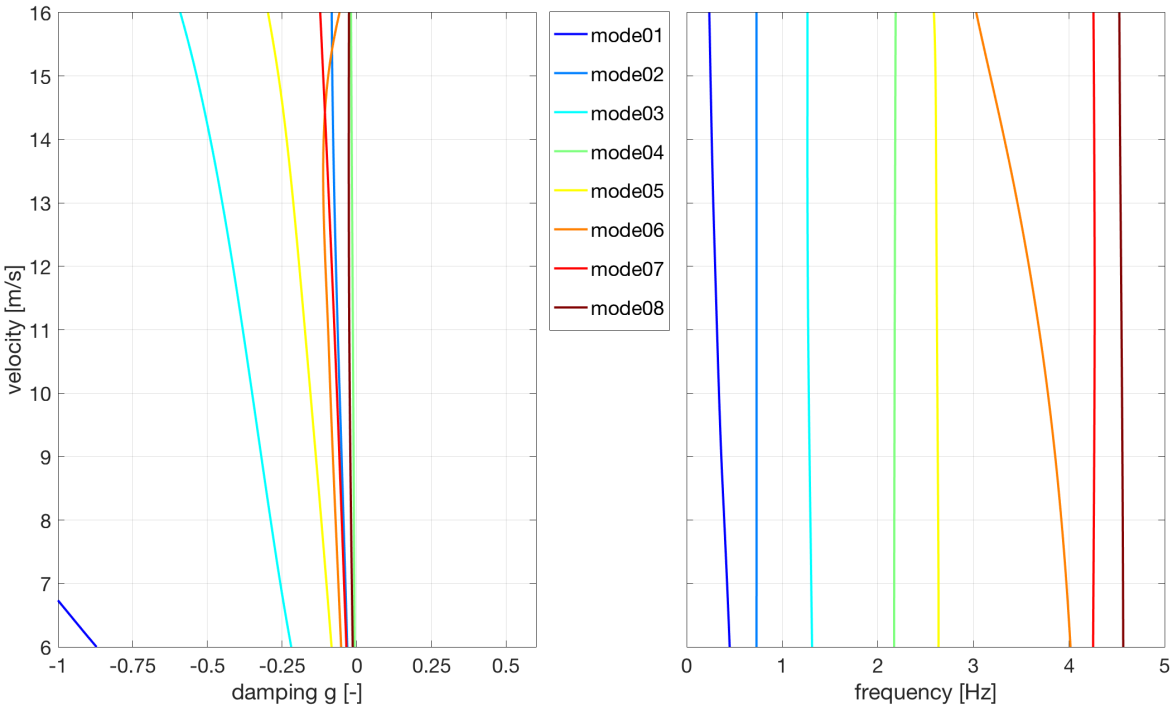

Figure 5.35: Frequency and damping plot (linearized around linear deflected blade)

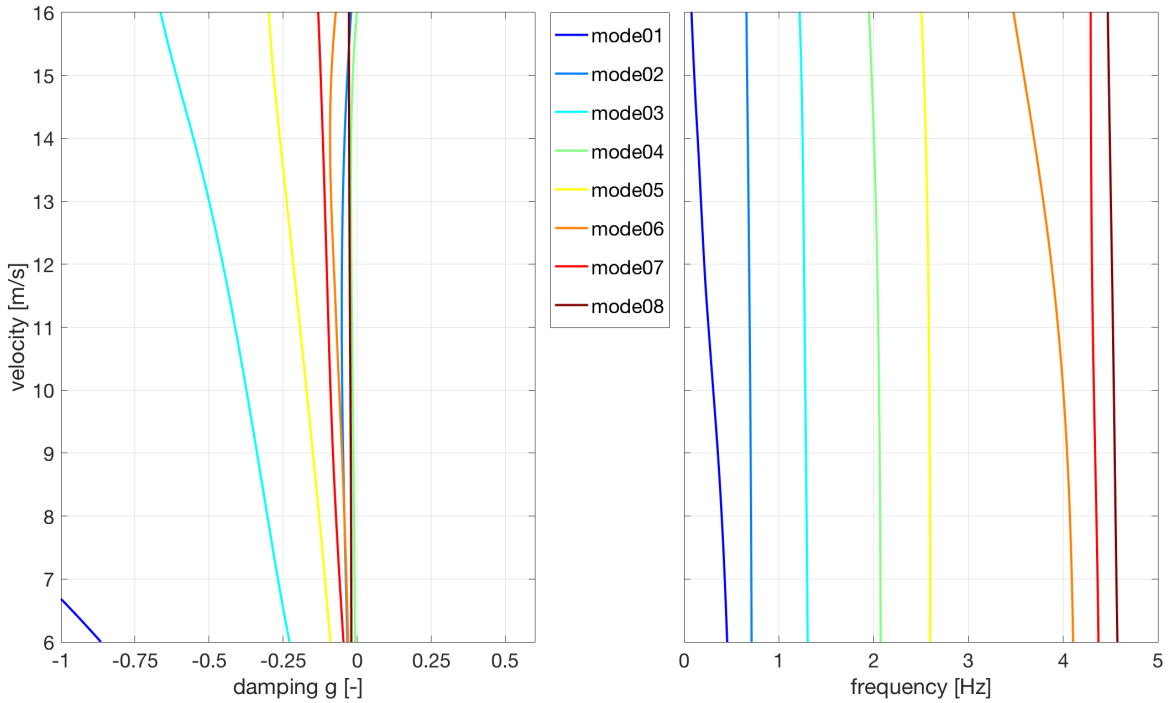

Figure 5.36: Frequency and damping plot (linearized around nonlinear deflected blade)

6

CONCLUSIONS AND RECOMMENDATIONS

In the ongoing quest for fossil fuel alternatives, an increasing interest in the research and development of more sustainable energy resources such as wind energy, has arisen. The continuous search for lower CoE is the driving factor behind the increasing size of wind turbines. This increase in size has resulted in novel wind turbine designs, for which aeroelastic effects become more prominent. In order to accurately analyze aeroelastic phenomena in extreme scale wind turbines, it is of great importance to adequately model the structural, aerodynamic and inertial aspects.
The aim of this research project is to develop a validated aeroelastic framework for the static and dynamic aeroelastic analysis of extreme scale wind turbines, with the objective of investigating the validity of linear structural modelling in the stability assessment of these machines.
In this chapter, the main conclusions drawn from this study are presented. The central research question and corresponding sub-questions that were presented in the introduction will be answered. As follows, some limitations that affect the extent of the drawn conclusions will be discussed. Additionally, recommendations on possible improvements of this work are presented and additional wind turbine related research topics of interest are proposed.

6.1. RESEARCH CONCLUSIONS

In order to realize the objective of this research, the existing aeroelastic framework of `ENSOLV` was used to perform a static aeroelastic analysis on a 108-meters long theoretic blade design provided by *We4Ce*. A modified version of the simulation framework including a nonlinear structural solver was utilized to compute the nonlinear steady-state solution. Both static solutions served as initial condition to perform flutter analyses. In flutter analysis, the structure is expressed by a set of eigenmodes that are separately forced into harmonic motion. In this manner, the effect of structural nonlinearities on the aeroelastic behavior could be investigated.
Since this study comprises a theoretical blade design, no validation data was available. As far as the realization of the objective, a comparative study was deemed adequate to draw a conclusion on the matter.

WHAT ARE THE KEY STRUCTURAL NONLINEARITIES IN THE AEROELASTIC BEHAVIOR OF AN EXTREME SCALE WIND TURBINE BLADE?

This question can be partially answered with knowledge gained from the conducted literature study. In literature, consensus exists that geometrical nonlinearities and follower-characteristics of centrifugal and aerodynamics loads are the most relevant structural nonlinearities for wind turbine blades. Geometric nonlinearities manifest themselves as displacements become larger. Follower-force effects are a consequence of structural displacements, leading to a different definition of the force vector. These effects cause a change in the stiffness of blades and the direction of forces.
A somewhat unexpected finding was that the blade is prone to local buckling effects in normal operating conditions. Buckling is a nonlinear effect, which arises if the local stiffness decreases. As shown in modal analysis, the blade was stiffened by tensile stresses induced by centrifugal forces. Compression at the suction of side of the blade caused an opposing effect, reducing the local stiffness. This effect can not be noticed when small displacements are assumed. As a result, linear analysis is not capable of assessing buckling effects. This study showed that buckling occurred in normal operating conditions. Hence, it can be concluded

that buckling is a phenomenon that can not be ignored in the analysis of extreme large wind turbines as it could lead to catastrophic failure.

WHAT EFFECTS DO STRUCTURAL NONLINEARITIES HAVE ON THE STATIC AEROELASTIC EQUILIBRIUM OF AN EXTREME SCALE WIND TURBINE BLADE?

Key finding in the performed static aeroelastic analyses is that differences in solution strategy predict a torsional deformation. Centrifugal forces belong to the class of follower-forces. When the blade deforms as a consequence of aerodynamic loads, it will substantially bend in axial direction. The direction of the centrifugal forces relative to the blade axis change resulting in an inward force component. This component creates a restoring moment leading to a reduction of the flapwise displacements. Additionally, it leads to a positive moment around the blade axis, resulting from the mass centre line lying aft the shear centre line. This moment reduces the blade's torsional deformation resulting to higher loads.
Furthermore, in linear analysis the displacements work in similar direction as the forces. As a result, aerodynamic tip loads elongate the blade. The nonlinear static analysis includes higher-order kinematic relations enabling to capture geometric and elastic coupling between bending, torsion, shear and extension. The artificial blade lengthening could lead to overestimation of loads and power, however the slight difference in blade length (below 0.5% R) does not affect the steady-state results considerably.
The results of the considered operational condition have shown that nonlinear geometric behavior and follower-force effects do not have a significant impact on static aeroelastic behavior. Most likely, these effects become more prominent in heavier inflow conditions.

COMPARED TO SEMI-LINEAR AEROELASTIC ANALYSIS, TO WHAT EXTENT DOES THE INCLUSION OF STRUCTURAL NONLINEARITIES ALTER THE DYNAMIC PROPERTIES OF THE BLADE? AND WHAT EFFECT DOES THIS HAVE ON THE AEROELASTIC RESPONSE?

From the literature review, it is known that the nonlinear stiffness matrix depends on the linear stiffness matrix, differential stiffness matrix and the follower-force stiffness matrix. Only a slight difference is observed between the eigenfrequencies computed with the linear stiffness matrix and the nonlinear stiffness matrix. However, modal analysis showed that initial stresses in the blade change the characteristic shape of various modes resulting in the inclusion of a torsional component. Evidently, the aeroelastic response of the blade is highly susceptible to torsion. As a consequence, the change in mode shapes leads to different aeroelasic behavior. The unsteady aerodynamic response of bending modes, incorporating torsional deformation due to nonlinear pre-stressing effects, was influenced most prominently. On the contrary, the first three mode shapes remained similar in comparison to the "linear" computed mode shapes. Furthermore, the behavior of the first torsional mode shape deemed to be less pronounced, when nonlinearities were included. As a result, the unsteady aerodynamic response to the enforced motion of this mode reduced in magnitude and became more sufficiently damped.

WHAT IS THE INFLUENCE OF STRUCTURAL NONLINEARITIES ON THE STABILITY ASSESSMENT OF AN EXTREME SCALE WIND TURBINE?

Aeroelastic behavior is a reciprocal relation between motion and aerodynamic forces. Due to alterations in the mode shapes of the blade, its motion changes and thus the aerodynamic response changes. Structural nonlinearities therefore have a noticeable effect on the flutter characteristics of the blade.
Damping and frequency characteristics directly result from the AIC's that are computed. As shown, a pure torsional mode lacked in the set of nonlinear modes. Instead, various modes contained a torsional component. The degree of torsion contributes to the proclivity of mode-coupling. The reduction in modal aerodynamic stiffness evidently prevents change in modal frequency over the entire computed domain.
Naturally low-damped modes, such as edgewise bending modes, can be affected negatively regarding their stability as torsion induces higher load fluctuations. Furthermore, it can be concluded that no flutter occurs, since the flapwise bending are strongly damped.

6.2. LIMITATIONS AND RECOMMENDATIONS

From the results and drawn conclusions, some recommendations can be made on potential enhancements of the current study or opportunities for research studies in a related field of work.

- The buckling problem could be resolved by increasing the thickness of the composite sandwich construction in the region of the instability. However, it was not known a priori how much effort it would

cost to adapt the structural design in order to be stable at heavy wind conditions. A parametric study can be conducted to investigate how the structural design can be optimized most efficiently, while maintaining its overall structural properties. As follows, the novel blade design could be used to assess nonlinear structural effects for higher loads.

- In the current study, the FSI iteration performed in the fully-nonlinear approach was executed manually. Since the aerodynamic loads computed for the linear and nonlinear deformed blade were similar for the considered flow condition, only one two-way FSI iteration had to be performed. However as the effect of structural nonlinearities increases for larger structural deformations, it is obvious that the steady-state solution of both approaches will increasingly deviate for more critical flow conditions. As a result, multiple iterations have to be performed to assure full convergence of the nonlinear solution. It is recommended to automate the entire process of the fully-nonlinear static aeroelastic approach in order to increase its efficiency.
  In fact, the sub models required in the fully-nonlinear approach are available in separate tools or in ENSOLV implemented algorithms. Makefile could be used to automate processes involved in the fully-nonlinear static aeroelastic framework. Makefile is a program building tool that runs on Unix or Linux, and can be used to execute separate modules automatically. It also allows definition of various solver settings that are needed in the separate modules. There already exists an automated process to perform flutter analysis, hence it can be decided to incorporate that algorithm.

- The unsteady aerodynamic simulations were performed on a coarse grid. Since it is required to run the simulations for multiple rotor revolutions in order to overcome transient effects, the simulations would require too much time if they were performed on fine or medium grid. The grid level convergence study has shown that the averaged total loads do not differ much, however it is known that the coarse grid will not capture the wake accurately. A prior study has shown that accurate prediction of the unsteady air loads in harmonic oscillatory motion is essential in the computation of the flutter boundary. Wake effects play a major role in the development of unsteady air loads and therefore the flutter analysis may not be accurate. The results should be validated using an alternative approach.

- The p-k method is valid for an operational envelope, in which the flow conditions on the blade are similar. This implies that for wind turbines the tip speed ratio and blade pitch must be kept constant. However, these parameters change for different inflow velocities. Additionally, the structural characteristics of a wind turbine blade depend on rotor velocity, while they are assumed constant in this method. The flutter analysis should be performed for multiple operational conditions to provide accurate results.
  Despite its drawbacks, the current solution methodology provided valuable insights about the importance of using an accurate expression of the structure.

- From literature review, it is known that edgewise vibrations are a relevant wind turbine instability caused by a coupling between the tower and rotor blades. Additionally, the presence of the tower causes a cyclic loading on the wind turbine rotor. In order to investigate these effects, the next step in the aeroelastic simulation of a wind turbine is to extend the wind turbine rotor with a tower and nacelle.
  The extension to a full wind turbine however, would be quite challenging, since different complex models must be integrated. First of all, the structural model must be adapted or even replaced, to incorporate coupling conditions between different wind turbine components. Secondly, at least one sliding interface must be added to the mesh, because the geometry consists of a stationary (i.e. tower) and moving part. And thirdly, multiple reference frames must be implemented in the analysis (this option is already available in ENSOLV).

- The initial objective of this research study was to perform static and dynamic aeroelastic simulations of an extreme scale wind turbine subject to atmospheric boundary layer flow. As mentioned earlier, imposing non-uniform inflow conditions requires coupling of moving- and stationary flow domains.

In order to realize the coupling, the sliding-mesh technique can be used. In this study, steady aerodynamic simulations around the rigid rotor have already been performed using the sliding-mesh technique, which gave similar results as the single-flow domain computations.
The simulations mentioned directly above could be extended by simulating atmospheric boundary layer flow or yaw inflow. The influence of unsteady air loads resulting from non-uniform inflow conditions, on the aeroelastic behavior of wind turbine could be investigated.

- In the current study, RANS is used as acting fluid model. From literature, it can be concluded that RANS is valid for wind turbine aerodynamics. However, even higher-fidelity CFD methods are increasingly used to model the flow around a wind turbine. LES-based CFD methods are superior in predicting separated flows and capturing the complex wake.
  From the verification results of the flow solver, some uncertainties arose about the flow solution around thick-trailing edge airfoils. LES-based CFD methods could be applied to obtain a better understanding of the flow physics around such profiles and give an error estimation of the method used in the current study.
  These methods can investigate the effects of turbulent wake structures on the dynamic blade loading and associated deformations.
  In ENSOLV a LES-based method (i.e. X-LES) is already implemented. In contrast to RANS, this method resolves large-scale turbulence using the aerodynamic grid as spatial filter. The aerodynamic grid may be adapted to assure capturing the wake using the full capability of this method.

REFERENCES

A. Chehouri, R. Younes, A. I. and Perron, J. (2015). Review of performance optimization techniques applied to wind turbines. *Applied Energy*, 142:361–388.

Abdulqadir, S. A., Iacovides, H., and Nasser, A. (2017). The physical modelling and aerodynamics of turbulent flows around horizontal axis wind turbines. *Energy*, 119:767 – 799.

Aerospace Engineering - Training (2016). Non linear analysis sol 106.

Ahrem, R., Beckert, A., and Wendland, H. (2001). A new multivariate interpolation method for large-scale spatial coupling problems in aeroelasticity.

Bangga, G., Lutz, T., and Krämer, E. (2017). An examination of rotational effects on large wind turbine blades.

Bazilevs, Y., Hsu, M.-C., Akkerman, I., Wright, S., Takizawa, K., Henicke, B., Spielman, T., and Tezduyar, T. (2011a). 3d simulation of wind turbine rotors at full scale. part i: Geometry modeling and aerodynamics. *International Journal for Numerical Methods in Fluids*, 65:207 – 235.

Bazilevs, Y., Hsu, M.-C., Kiendl, J., Wüchner, R., and Bletzinger, K.-U. (2011b). 3d simulation of wind turbine rotors at full scale. part ii: Fluid-structure interaction modeling with composite blades. *International Journal for Numerical Methods in Fluids*, 65:236 – 253.

Bedri, R. and Al-Nais, M. O. (2005). Prestressed modal analysis using finite element package ansys. In Li, Z., Vulkov, L., and Waśniewski, J., editors, *Numerical Analysis and Its Applications*, pages 171–178, Berlin, Heidelberg. Springer Berlin Heidelberg.

Berg, D. E. and Barone, M. (2008). Aerodynamic and aeroacoustic properties of a flatback airfoil (will it rumble or whisper?).

Bijl, H., van Zuijlen, A. H., Boer, A. D., and Rixen, D. J. (2008). Fluid-structure interaction (wb1417) - lecture notes. Technical report, Delft University of Technology.

Bir, G. and Jonkman, J. (2007). Aeroelastic instabilities of large offshore and onshore wind turbines. *Journal of Physics: Conference Series*, 75:012069.

Bisplinghoff, R., Ashley, H., and Halfman, R. (1996). *Aeroelasticity*. Addison-Wesley Publishing Company.

Boussinesq, J. (1877). *Essai sur la théorie des eaux courantes*. Imprimerie Nationale.

Carrión, M., Steijl, R., Woodgate, M., Barakos, G. N., Munduate, X., and Gomez-Iradi, S. (2014). Aeroelastic analysis of wind turbines using a tightly coupled cfd–csd method. *Journal of Fluids and Structures*, 50:392 – 415.

CFD Online (2011). Law of the wall.

Chortis, D., Chrysochoidis, N., and Saravanos, D. (2007). Damped structural dynamics models of large wind-turbine blades including material and structural damping. *Journal of Physics: Conference Series*, 75:012076.

Clark, R., Cox, D., Curtiss, H. C. j., Dowell, E. H., Edwards, J. W., Hall, K. C., Peters, D. A., Scanlan, R., Simiu, E., Sisto, F., and Strganac, T. W. (2012). *A modern course in aeroelasticity*. Kluwer Academic Publishers.

Corson, D. A., Griffith, D. T., Ashwill, T. D., and Shakib, F. (2012). Investigating aeroelastic performance of multi-megawatt wind turbine rotor using cfd. In *Structures, Structural Dynamics and Materials Conference*.

De Boer, A. D. (2008). *Computational fluid-structure interaction: Spatial coupling, coupling shell and mesh deformation*. PhD thesis.

De Boer, A. D., Van Zuijlen, A. H., and Bijl, H. (2008). Comparison of conservative and consistent approaches for the coupling of non-matching meshes. *Computer Methods in Applied Mechanics and Engineering*, 197(49):4284 – 4297.

De Cock, K. M. J., Kok, J. C., van der Ven, H., Soemarwoto, B. I., Boelens, O. J., and Oskam, B. (2004). Extra-large eddy simulation for delta wings and space launchers. In *24th INTERNATIONAL CONGRESS OF THE AERONAUTICAL SCIENCES*.

EDGE (2010). Theoretical formulation, technical report 03-2870. Technical report, Edge.

Enercon GmbH (2016). Enercon energy for the world.

Favre, A. (1965). Equations des gaz turbulents compressibles. *Journal de mécanique*, 4(3):361–421.

Fedorov, V. and Berggreen, C. (2014). Bend-twist coupling potential of wind turbine blades. *Journal of Physics: Conference Series*, 524:012035.

Flanigan, C. C. (1998). Model reduction using guyan, irs, and dynamic methods. 1.

Froude, R. (1889). On the part played in propulsion by difference in pressure. *Transactions of the Institution of Naval Architects*, pages 390–423.

Glauert, H. (1935). *Airplane Propellers*, pages 169–360. Springer Berlin Heidelberg, Berlin, Heidelberg.

Griffith, D. T. and Ashwill, T. D. (2011). The sandia 100-m all-glas baseline wind turbine blade: Snl 100-00. Technical report, Sandia National Laboratories.

Gritskevich, M. S., Garbaruk, A. V., Schütze, J., and Menter, F. R. (2012). Development of ddes and iddes formulations for the k-ω shear stress transport model. *Flow, Turbulence and Combustion*, 88(3):431–449.

Gu, Y. and Yang, Z. (2012). Modified p-k method for flutter solution with damping iteration. *AIAA Journal*, 50:507–510.

Guo, T., Lu, Z., Tang, D., Wang, T., and Dong, L. (2013). A cfd/csd model for aeroelastic calculations of large-scale wind turbines. *Science China: Technological sciences*, 56(1):205–211.

Hansen, A. C. and Laino, D. J. (1997). Validation study for aerodyn and yawdyn using phase iii combined experiment data.

Hansen, M. (2007). Aeroelastic instability problems for wind turbines. *Wind Energy*, 10:551 – 577.

Hansen, M., Gaunaa, M., and Madsen, H. (2004). A beddoes-leishman type dynamic stall model in state-space and indicial formulations.

Hansen, M. O. L., Sørensen, J. N., Voutsinas, S., Sørensen, N., and Madsen, H. A. (2006). State of the art in wind turbine aerodynamics and aeroelasticity. *Progress in Aerospace Sciences*, 42(4):285 – 330.

Hassig, H. J. (1971). An approximate true damping solution of the flutter equation by determinant iteration. *Journal of Aircraft - J AIRCRAFT*, 8:885–889.

Heeg, J. (2000). Dynamic investigation of static divergence: Analysis and testing.

Hellsten, A. (2019). New two-equation turbulence model for aerodynamics applications. *951-22-6933-3*.

Herráez, I., Stoevesandt, B., and Peinke, J. (2014). Insight into rotational effects on a wind turbine blade using navier–stokes computations. *Energies*, 7.

Hibbit, H. D. (1979). Some follower forces and load stiffness. *International Journal for Numerical Methods in Engineering*, 14(6):937–941.

Hodges, D. (2003). Geometrically exact, intrinsic theory for dynamics of curved and twisted anisotropic beams. *AIAA Journal*, 41:1131–1137.

Holierhoek, J. G. (2013). An overview of possible aeroelastic instabilities for wind turbine blades. *Wind Engineering*, 37:421–440.

Hounjet, M. and Meijer, J. J. (1995). Evaluation of elastomechanical and aerodynamic data transfer methods for non-planar configurations in computational aeroelastic analysis. pages 11.1–11.24.

Hsu, M.-C. and Bazilevs, Y. (2012). Fluid-structure interaction modeling of wind turbines: Simulating the full machine. *Computational Mechanics*, 50:821–833.

Jameson, A. (2012). *Time dependent calculations using multigrid, with applications to unsteady flows past airfoils and wings*.

Jelenić, G. and Crisfield, M. (1999). Geometrically exact 3d beam theory: Implementation of a strain-invariant finite element for statics and dynamics. *Computer Methods in Applied Mechanics and Engineering*, 171:141–171.

Jonkman, J., Butterfield, S., Musial, W., and Scott, G. (2009). Defintiion of a 5-mw reference wind turbine for offshore system development. Technical report, National Renewable Energy Labratory.

Jonkman, J. M. and Buhl, M. L. (2005). Fast user's guide. Technical report, National Renewable Energy Laboratory.

Kaw, A. K. (2006). Mechanics of composite materials / a.k. kaw.

Kenway, G. and Martins, J. (2008). Aerostructural shape optimization of wind turbine blades considering site-specific winds. *Proceedings of the 12th AIAA/ISSMO Multidisciplinary Analysis and Optimization Conference. Victoria, BC*.

Kok, J. C. (2000). Resolving the dependence on freestream values for the k- turbulence model. *AIAA Journal*, 38(7):1292–1295.

Kok, J. C. (2019). User guide of ensolv version 7.71: A flow solver for aerodynamic, aeroelastic, and aeroacoustic applications using 3d multi-block structured grids.

Larsen, T. and Hansen, M. A. (2004). Aeroelastic effects of large blade deflections for wind turbines.

Launder, B. and Spalding, D. B. (1972). *Lectures in Mathematical Model of Turbulence*.

Lavaroni, L., Watson, S. J., Cook, M. J., and Dubal, M. R. (2014). A comparison of actuator disc and BEM models in CFD simulations for the prediction of offshore wake losses. *Journal of Physics: Conference Series*, 524:012148.

Lindenburg, C. (2003). Investigation into rotor blade aerodynamics, Analysis of the stationary measurements on the UAE phase-VI rotor in the NASA-Ames wind tunnel. Technical report, ECN. ECN-C–03-025.

Lobitz, D. W. (2004). Aeroelastic stability predictions for a mw-sized blade. *Wind Energy*, 7:211 – 224.

Madsen, H. A. and Rasmussen, F. (1998). Prediction of dynamic loads and induced vibrations in stall - stallvib. Science Panel meeting no. 1, National Wind Energy Technology Center (NWTC) ; Conference date: 05-10-1998 Through 06-10-1998.

Menter, F. R. (1992). Influence of freestream values on k-ω turbulence model predictions. 30.

Mertes, C., Singh, M., Strike, J., Hind, M., Babbitt, A., Baker, J., Naughton, J., and Sitaraman, J. (2011). A study of flatback airfoils in dynamic motion.

Michaelson, P. M. (2015). *A Fluid-Structure Interaction tool for application in rotating machinery*. PhD thesis, Karlsruher Institut fur Technologie.

Moshfeghi, M., Song, Y. J., and Xie, Y. H. (2012). Effects of near-wall grid spacing on sst-k-ω model using nrel phase vi horizontal axis wind turbine. *Journal of Wind Engineering and Industrial Aerodynamics*, 107-108:94 – 105.

MSC Software Corporation (2017). Nx nastran's user guide. Technical report.

Mughal, B. (2005). A calculation method for the three-dimensional boundary-layer equations in integral form.

Ounis, H. and Balehouane, A. (2016). Buckling behavior of wind turbine blade. *Revue des Energies Renouvelables*, 19:509–516.

Pavel, M. D. and Schoones, M. M. J. (1999). Literature survey on aeromechanical instabilities for helicopters and wind turbines. Technical report, Faculty of Aerospace Engineering TU Delft.

Platt, A. D. and Buhl, M. (2012). Wtperf user guide for version 3.05.00. Technical report, National Renewable Energy Laboratory.

Prananta, B. (1999). Physical and numerical aspects of aeroelastic simulations.

Prananta, B. B., Kok, J. C. and. Spekreijse, S. P., Hounjet, M. H. L., and Tjatra, I. W. (2000). Aeroelastic simulation method for military aircraft configurations: Predesign of fluid/structure coupling method in aesim-mil project. Technical report, Netherlands Aerospace Centre.

Prandtl, L. (1926). Ueber die ausgebildete turbulenz. In *Proceedings 2nd International Congress Applied Mechanics, Zurich*, page 62.

Ramanujam, G. and Ozdemir, H. (2017). Improving airfoil lift prediction.

Rankine, W. J. M. (1865). On the mechanical principles of the action of propellers. *Transactions of the Institution of Naval Architects*, 13:13–30.

Resor, B., Wilson, D., Berg, D., Berg, J., Barlas, T., Wingerden, J. W., and Kuik, G. (2010). Impact of higher fidelity models on simulation of active aerodynamic load control for fatigue damage reduction.

Riziotis, V. A. and Voutsinas, S. G. (1997). Gast: A general aerodynamic and structural prediction tool for wind turbines. In *Proceedings of the EWEC'97*.

Rodden, W. P. and Johnson, E. H. (1994). *MSC/NASTRAN Aeroelastic Analysis User's Guide, Ver. 68*. MacNeal-Schwendler.

Sale, D., Aliseda, A., Motley, M., and li, y. (2013). Structural optimization of composite blades for wind and hydrokinetic turbines.

Schepers, J. G., Boorsma, K., Cho, T., Gomez-Iradi, S., Schaffarczyk, P., Jeromin, A., Shen, W. Z., Lutz, T., Meister, K., Stoevesandt, B., Schreck, S., Micallef, D., Pereira, R., Sant, T., Aagaard Madsen, H., and Sørensen, N. (2012). Analysis of mexico wind tunnel measurements: Final report of iea task 29, mexnext (phase 1). Technical report.

Schepers, J. G. and Snel, H. (1995). Dynamic inflow: yawed conditions and partial span pitch control. Technical report, ECN. ECN-C-95-056.

Schlichting, H. and Gersten, K. (2001). *Boundary-Layer Theory*, volume 20.

Snel, H. and Schepers, J. G. (1995). Joint investigation of dynamic inflow effects and implementation of an engineering method. Technical report, ECN. ECN-C–94-107.

Sørensen, J., Larsen, P., Pedersen, B., and Jensen, J. (1986). *Three-Level, Viscous-Inviscid Interaction Technique for the Prediction of Separated Flow Past Rotating Wing*. PhD thesis.

Spalart, P., Jou, W.-H., Strelets, M., and Allmaras, S. (1997). Comments on the feasibility of les for winds, and on a hybrid rans/les approach. 1:4–8.

Spalart, P. R. (2000). Strategies for turbulence modelling and simulations. *International Journal of Heat and Fluid Flow*, 21(3):252 – 263.

Spalart, P. R., Deck, S., Shur, M. L., Squires, K. D., Strelets, M. K., and Travin, A. (2006). A new version of detached-eddy simulation, resistant to ambiguous grid densities. *Theoretical and Computational Fluid Dynamics*, 20(3):181.

Spera, D. A. (1994). *Wind Turbine Technology: Fundamental Concepts in Wind Turbine Engineering*, chapter Structural Dynamic Behavior of Wind Turbines. ASME Press, New York.

Stuurman, M. (2016). Simulating flutter of a 100-m wind turbine blade. Master's thesis, Delft University of Technology.

Sørensen, N., Michelsen, J., and Schreck, S. (2002). Navier–stokes predictions of the nrel phase vi rotor in the nasa ames 80 ft × 120 ft wind tunnel. *Wind Energy*, 5(2-3):151–169.

Tatomir, N. (2019). Efficacy of linearized aerodynamic cfd modeling for flutter computation. Master's thesis, Delft University of Technology.

Ten Pas, S. (2016). Cfd simulations of the mexico wind turbine: Validating ensolv for wind turbine flows. Master's thesis, University of Twente.

Turkel, E., Vatsa, V. N., and Radespiel, R. (1996). Preconditioning methods for low-speed flow.

Tweedt, D. L., Chima, R. V., and Turkel, E. (1997). Preconditioning for numerical simulation of low mach number three-dimensional viscous turbomachinery flows.

UNFCCC (2015). Adoption of the paris agreement.

Van Garrel, A. (2016). *Multilevel Panel Method for Wind Turbine Rotor Flow Simulations*. PhD thesis.

van Garrel, A., Pas, S., Venner, C., and Muijden, J. (2018). Wind turbine aerodynamics from an aerospace perspective.

Van Zuijlen, A. H. (2014). Fluid-structure interaction ae4117 - lecture slides. Technical report, Delft University of Technology.

Wallin, S. and Johansson, A. V. (2002). Modelling streamline curvature effects in explicit algebraic reynolds stress turbulence models. *International Journal of Heat and Fluid Flow*, 23(5):721 – 730.

Wilcox, D. C. (1988). Reassessment of the scale-determining equation for advanced turbulence models. 26:1299–1310.

Wilcox, D. C. (2006). Turbulence modeling for cfd. *Turbulence Modeling for CFD*, 2.

Yu, D. O. and Kwon, O. J. (2013). A coupled cfd-csd method for predicting hawt rotor blade performance.

Zienkiewicz, O. C. and Taylor, R. (2005). *The Finite Element Method*, volume I.

A

INPUT PARAMETERS FOR CFD SIMULATIONS

This appendix provides a summary comprising the settings of ENSOLV for the executed CFD simulations. Table A.1 contains the settings of the steady aerodynamic solves including load case 1 of the undeformed blade and load case 2 of the nonlinear deformed blade. Note that no aeroelastic coupling is present in these simulations. Additionally, table A.2 summarize the input parameters of the static aeroelastic analyses performed in ENSOLV. And lastly, table A.3 gives an overview of the parameters defined for the flutter analysis. The parameters involving the time-step, reduced frequency and simulation time are omitted from the table as they are discussed in chapter 5.

Parameters	Meaning	Settings	
-	-	Load case 1	Load case 2
Mach	Mach number	0.0338	0.0206
Reyn	Reynolds number	$7.83{\cdot}10^5$	$4.76{\cdot}10^5$
NasMod	Fluid model	Full RANS	Full RANS
Rlen	Reference length	1	1
UnsMod	Solution mode	-1	-1
AEMod	Aeroelastic mode	0	0
TurMod	Turbulence model	k-ω SST	k-ω SST
AngVel	$\frac{\omega L}{U_\infty}$	0.0792	0.0942
MaxML	FAS multi-grid levels	2	2
Npre	Pre-relaxations in multi-grid	20	20
Npost	Post-relaxations in multi-grid	20	20
CFL	Courant number	3	3
TurPdl	Limiter of k production	10	10

Table A.1: Settings for steady solves

Parameters	Meaning	Settings	
-	-	Load case 1	Load case 2
Mach	Mach number	0.0338	0.0206
Reyn	Reynolds number	$7.83{\cdot}10^5$	$4.76{\cdot}10^5$
NasMod	Fluid model	Full RANS	Full RANS
Rlen	Reference length	1	1
UnsMod	Solution mode	-1	-1
AEMod	Aeroelastic mode	2	2
TurMod	Turbulence model	k-ω SST	k-ω SST
AngVel	$\frac{\omega L}{U_\infty}$	0.0792	0.0942
MaxML	FAS multi-grid levels	2	2
Npre	Pre-relaxations in multi-grid	20	20
Npost	Post-relaxations in multi-grid	20	20
CFL	Courant number	3	3
TurPdl	Limiter of k production	10	10
DefNit	Grid-folding smoothing iterations	5	5
DefUnd	Under-relaxation for grid smoothing	0.6	0.6
VindX	Speed index	12.728	7.748
AerLen	Reference length structural model	1	1
UndrX	Under-relaxation of EOM	0.5	0.5

Table A.2: Settings for static aeroelastic solves

Parameters	Meaning	Settings
Mach	Mach number	0.0206
Reyn	Reynolds number	$4.76{\cdot}10^5$
NasMod	Fluid model	Full RANS
Rlen	Reference length	1
UnsMod	Solution mode	3
AEMod	Aeroelastic mode	0
TurMod	Turbulence model	k-ω SST
AngVel	$\frac{\omega L}{U_\infty}$	0.0942
MaxML	FAS multi-grid levels	2
Npre	Pre-relaxations in multi-grid	20
Npost	Post-relaxations in multi-grid	20
CFL	Courant number	3
TurPdl	Limiter of k production	10
DefNit	Grid-folding smoothing iterations	5
DefUnd	Under-relaxation for grid smoothing	0.6
NmodRq	Requeste number of modes	8
AmplM	Amplitude of imposed motion	0.005

Table A.3: Settings for flutter analysis

B

COMPUTATION OF LOCAL AERODYNAMIC FORCE COEFFICIENTS

The pressure distribution of a blade element can be integrated, which will lead to the force on the blade element. The forces per section can be used to determine the aerodynamic force coefficient, like lift and drag coefficient. It is chosen to output the pressures in the cell vertices, $L_i(x_i, y_i)$. The integrated forces are considered in the centre of the cell edge, $\overline{F_i}(F_{x,i}, F_{y,i})$ at the blade segment ds: $[L_i, L_{i+1}]$. The pressure over a segment is assumed to be linear.

To integrate the pressure, the following expression is used:

$$||\overline{F_i}|| = \int_{x_i}^{x_{i+1}} (p - p_\infty) ds \tag{B.1}$$

In case of a closed shaped, the atmospheric pressure can be ommitted.

$$p(x) = p_i + \frac{p_{i+1} - p_i}{x_{i+1} - x_i}(x - x_i) \tag{B.2}$$

$$ds = \sqrt{1 + \left(\frac{y_{i+1} - y_i}{x_{i+1} - x_i}\right)^2}\, dx \tag{B.3}$$

Substituting B.2 and B.3 in equation B.1 gives:

$$||\overline{F_i}|| = \int_{x_i}^{x_{i+1}} \left(p_i + \frac{p_{i+1} - p_i}{x_{i+1} - x_i}(x - x_i)\right) \sqrt{1 + \left(\frac{y_{i+1} - y_i}{x_{i+1} - x_i}\right)^2}\, dx \tag{B.4}$$

$$||\overline{F_i}|| = \sqrt{1 + \left(\frac{y_{i+1} - y_i}{x_{i+1} - x_i}\right)^2}\, \frac{p_{i+1} + p_i}{2} |x_{i+1} - x_i| \tag{B.5}$$

In order to compute the force components, the angle the horizontal axis and the segment must be known:

$$|cos\beta_i| = \sqrt{\frac{1}{1 + \left(\frac{y_{i+1} - y_i}{x_{i+1} - x_i}\right)^2}} \tag{B.6}$$

$$|sin\beta_i| = \sqrt{\frac{1}{1 + \left(\frac{x_{i+1} - x_i}{y_{i+1} - y_i}\right)^2}} \tag{B.7}$$

$$F_{x,i} = ||\overline{F_i}|| |sin\beta_i| \frac{y_i - y_{i+1}}{|y_i - y_{i+1}|} \tag{B.8}$$

$$F_{y,i} = ||\overline{F_i}|| |cos\beta_i| \frac{x_{i+1} - x_i}{|x_{i+1} - x_i|} \tag{B.9}$$

Summing all forces gives the sectional forces in x- and y-direction:

$$F_x = \sum_{i=1}^{N+1} F_{x,i} \tag{B.10}$$

$$F_y = \sum_{i=1}^{N+1} F_{y,i} \tag{B.11}$$

The forces are non-dimensionalized into force coefficients in the following way:

$$C_x = \frac{F_x}{\frac{1}{2}\rho[{U_\infty}^2 + (\omega r)^2}] \tag{B.12}$$

$$C_y = \frac{F_y}{\frac{1}{2}\rho[{U_\infty}^2 + (\omega r)^2}] \tag{B.13}$$

Where ρ is the fluid density, c is the chord length, U_∞ is the freestream velocity, ω is the angular velocity and r is the radial distance of the blade section. The lift-and drag coefficients can be computed from the expressions of the force coefficients, when the flow incidence angle on the rotor plane is known.

The incidence angle is approximated as follows:

$$\beta = \arctan\frac{U_\infty}{\omega r} \tag{B.14}$$

$$C_L = C_x \cos\beta + C_y \sin\beta \tag{B.15}$$

$$C_D = C_x \sin\beta - C_y \cos\beta \tag{B.16}$$

C

PRESSURE AND VELOCITY PLOTS FROM STEADY AERODYNAMIC SIMULATION

In this appendix a more comprehensive overview is given of the velocity and pressure plots at several spanwise locations of the wind turbine blade. All velocity and pressure plots that are shown are from the steady aerodynamic simulation of case 1 (V = 11.5 m/s. The velocities in y-direction show that the flows was separated at the inboard section. Furthermore, it is observed that the blunt trailing-edge profiles produced a thick wake leading to three-dimensional flow. Separated air is driven outwards by centrifugal forces leading to cross-flow. It is known that cross-flow could lead to lift enhancement of radial outward blade segments due to re-energizing the boundary layer. Additionally, radial flow could result in stall-delay. In conditions involving heavy flow separation, these effects will be most prominent. However for the load cases considered in this study, these effects do not occur.

VELOCITY PLOTS

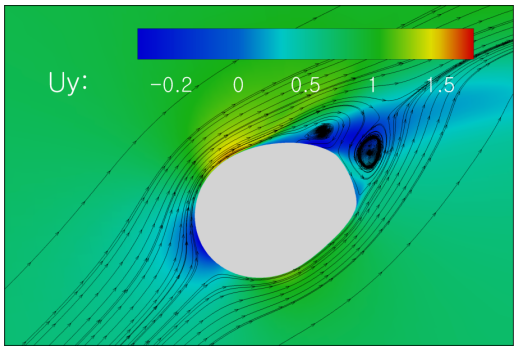

(a) $z/R = 0.12$

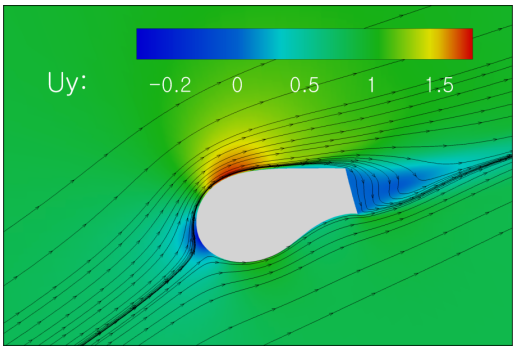

(b) $z/R = 0.17$

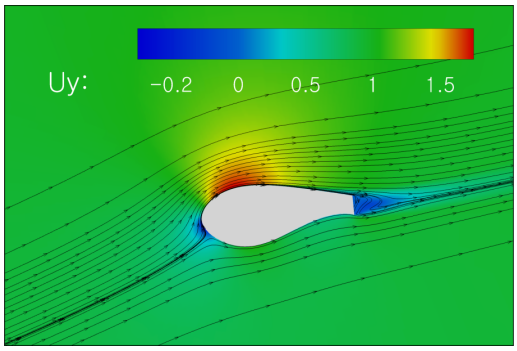

(c) $z/R = 0.26$

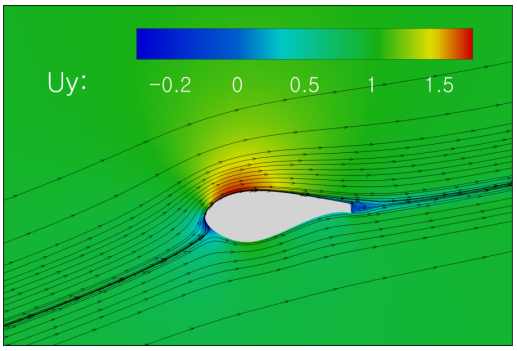

(d) $z/R = 0.31$

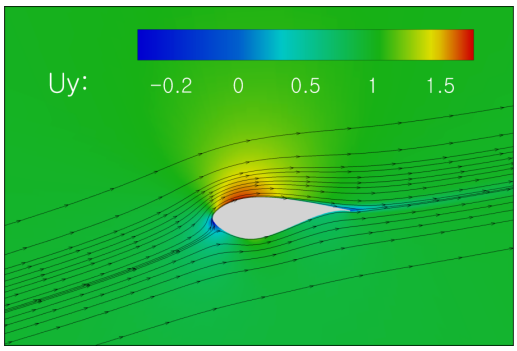

(e) $z/R = 0.37$

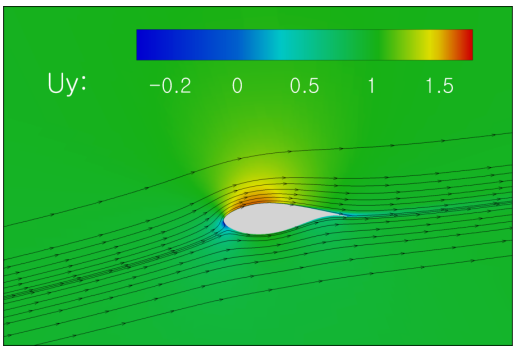

(f) $z/R = 0.48$

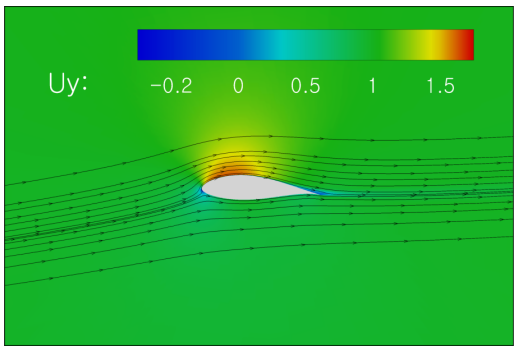

(g) $z/R = 0.90$

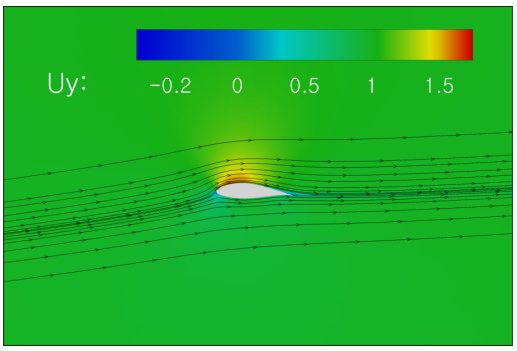

(h) $z/R = 0.99$

Figure C.1: Velocity plots at several spanwise locations of the blade

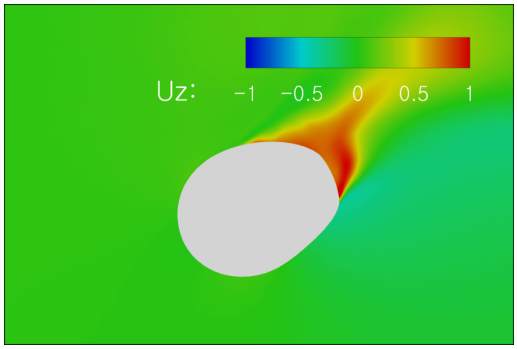

(a) $z/R = 0.12$

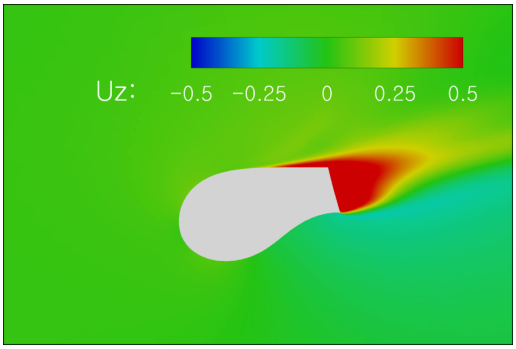

(b) $z/R = 0.17$

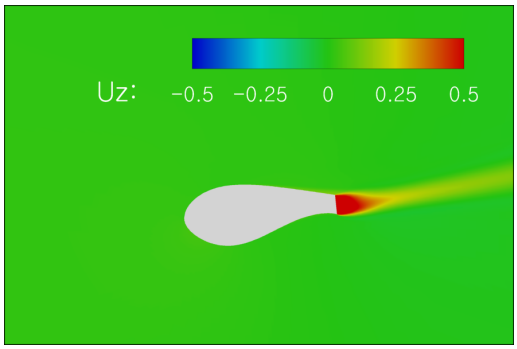

(c) $z/R = 0.26$

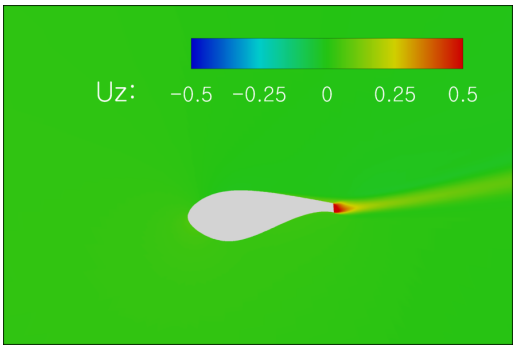

(d) $z/R = 0.31$

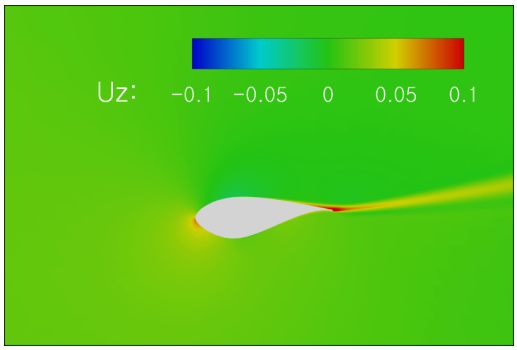

(e) $z/R = 0.37$

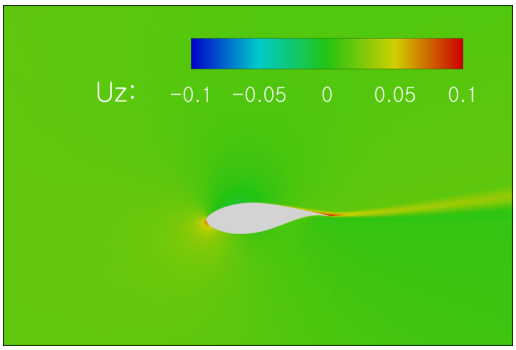

(f) $z/R = 0.48$

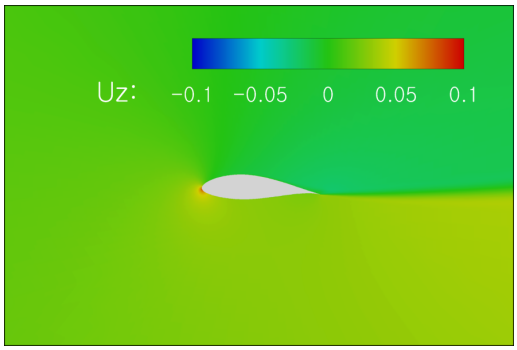

(g) $z/R = 0.90$

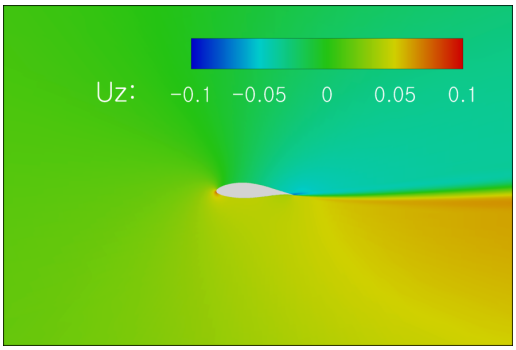

(h) $z/R = 0.99$

Figure C.2: spanwise velocity plots at several spanwise locations of the blade

PRESSURE PLOTS

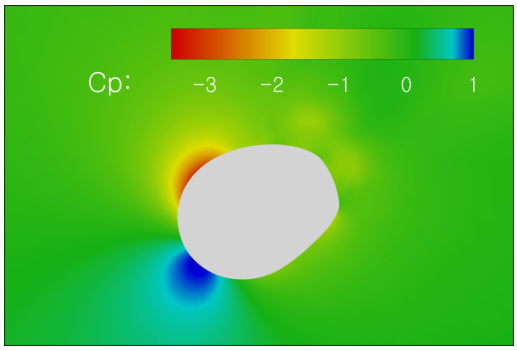

(a) $z/R = 0.12$

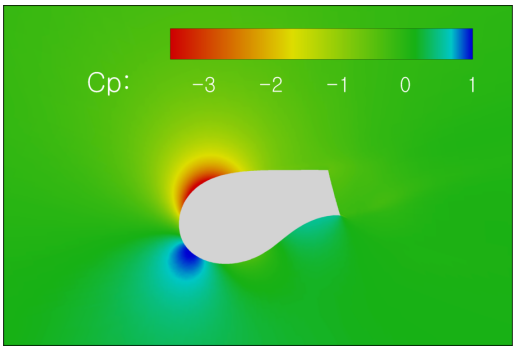

(b) $z/R = 0.17$

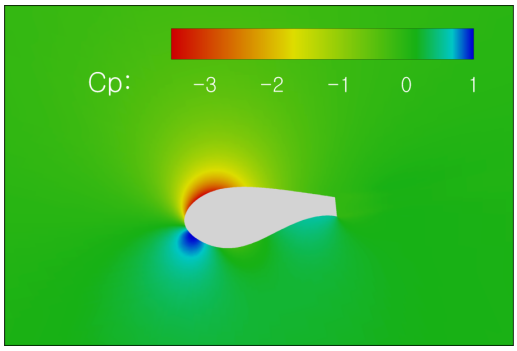

(c) $z/R = 0.26$

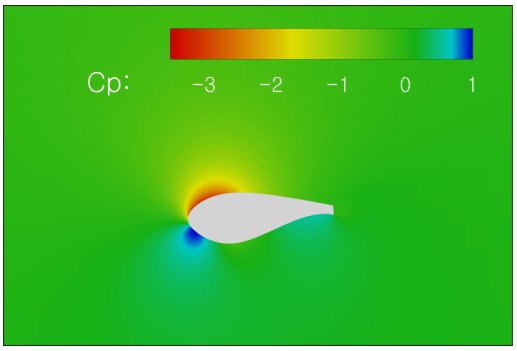

(d) $z/R = 0.31$

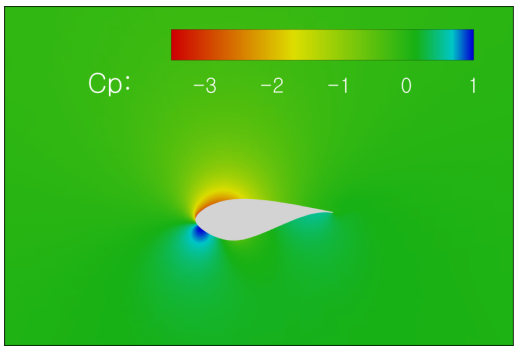

(e) $z/R = 0.37$

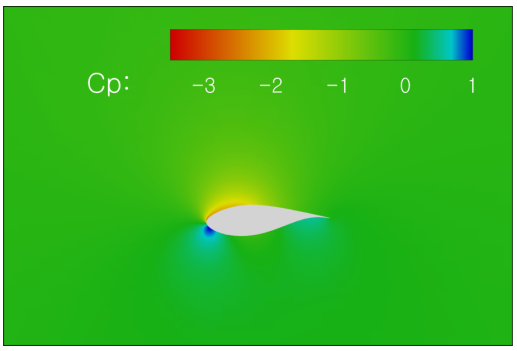

(f) $z/R = 0.48$

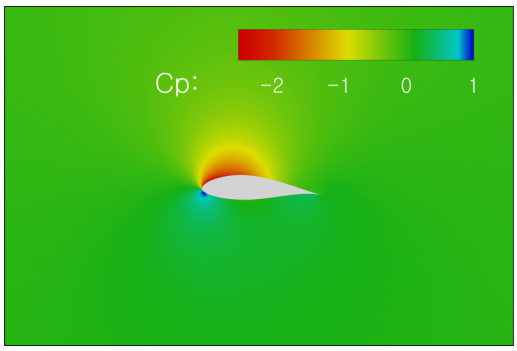

(g) $z/R = 0.90$

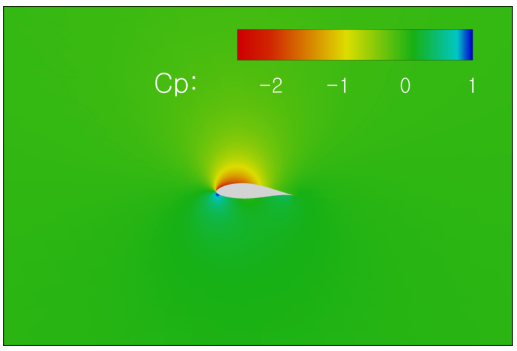

(h) $z/R = 0.99$

Figure C.3: Pressure plots at several spanwise locations of the blade

D

PRESSURE AND VELOCITY PLOTS FROM STATIC AEROELASTIC SIMULATION

In this appendix a more comprehensive overview is given of the velocity and pressure plots at several spanwise locations of the wind turbine blade. All velocity and pressure plots shown are obtained from static aeroelastic analysis of load case 1 (V = 11.5 m/s). The velocity and pressure plots of case 2 are not shown. The effects shown in the rigid case, can also be observed in these results. The flow conditions do not substantially change, although the change in angle of attack decreases the pressures over the blade, especially for the outboard segments

VELOCITY PLOTS

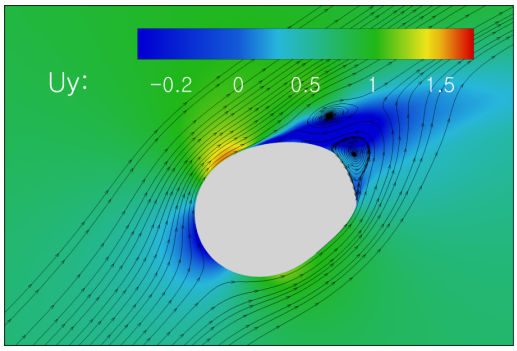

(a) $z/R = 0.12$

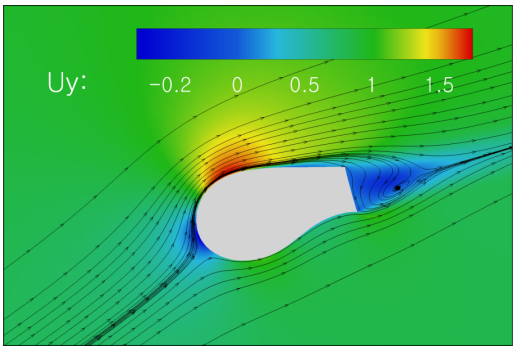

(b) $z/R = 0.17$

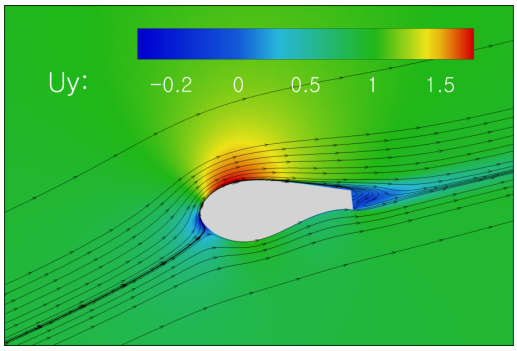

(c) $z/R = 0.26$

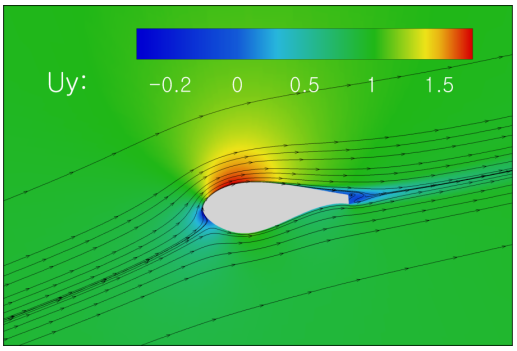

(d) $z/R = 0.31$

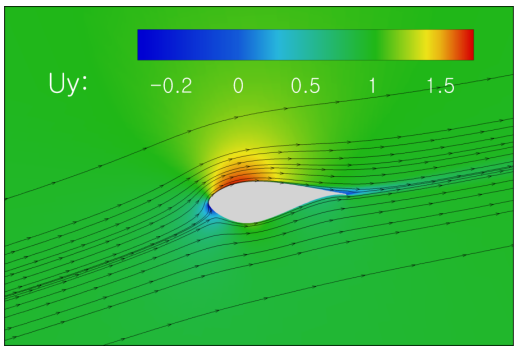

(e) $z/R = 0.37$

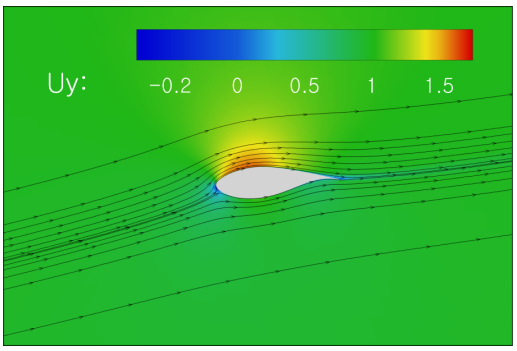

(f) $z/R = 0.48$

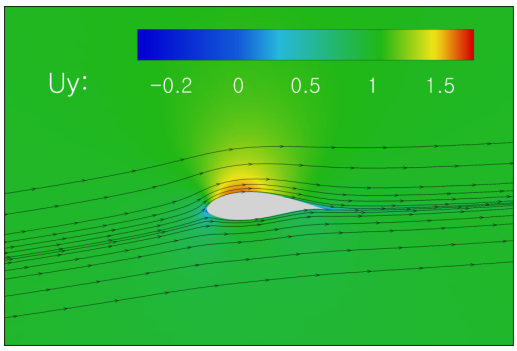

(g) $z/R = 0.90$

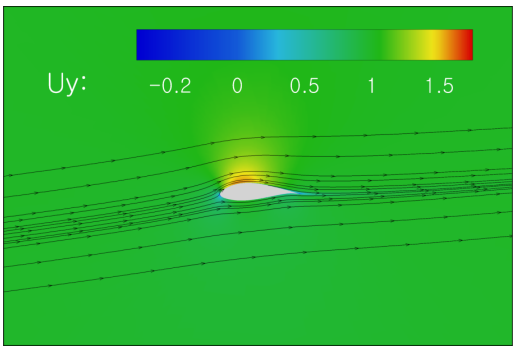

(h) $z/R = 0.99$

Figure D.1: Velocity plots at several spanwise locations of the blade

PRESSURE PLOTS

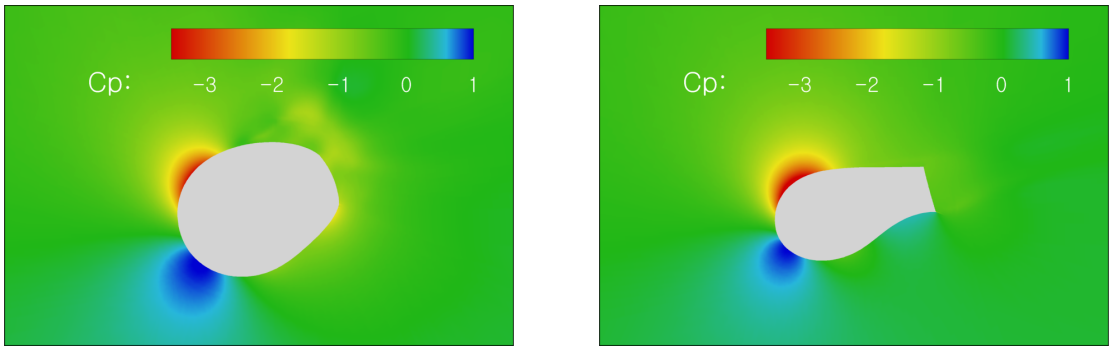

(a) $z/R = 0.12$

(b) $z/R = 0.17$

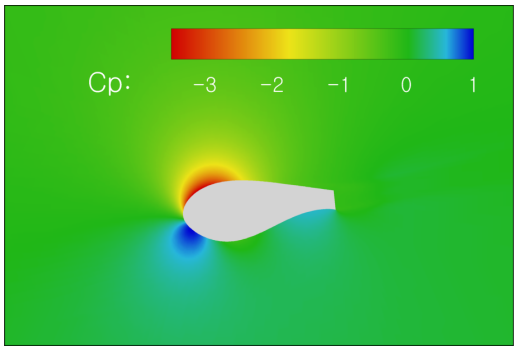

(c) $z/R = 0.26$

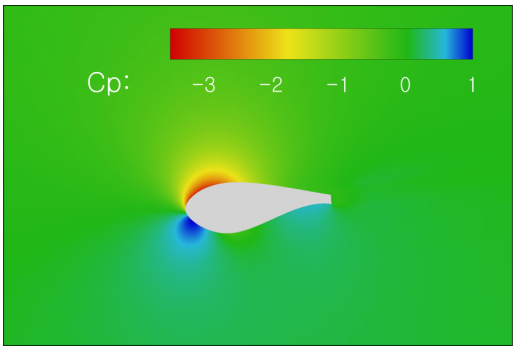

(d) $z/R = 0.31$

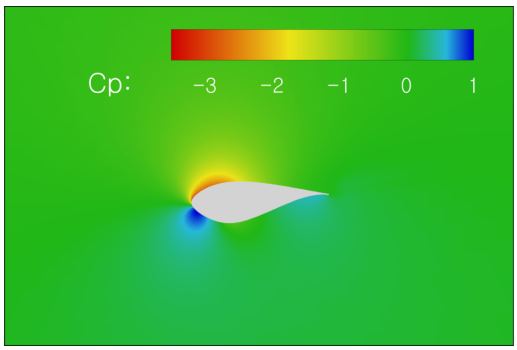

(e) $z/R = 0.37$

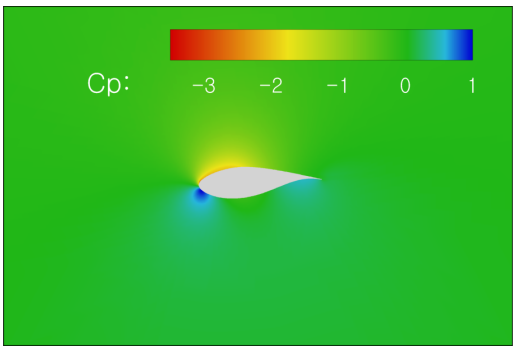

(f) $z/R = 0.48$

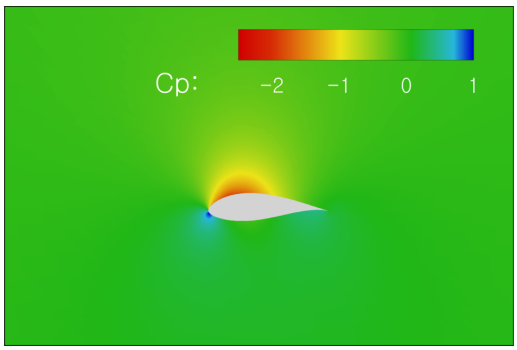

(g) $z/R = 0.90$

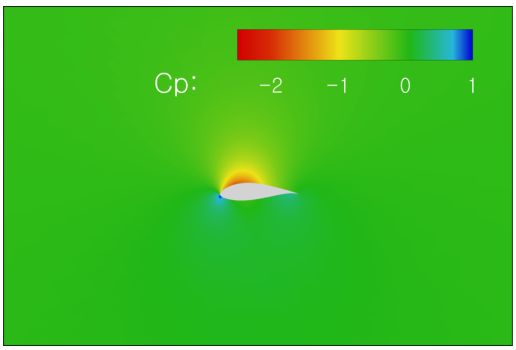

(h) $z/R = 0.99$

Figure D.2: Pressure plots at several spanwise locations of the blade

E

MODE SHAPES AROUND LINEAR AND NONLINEAR DEFLECTED BLADE

In this appendix the "linear" and "nonlinear mode shapes are presented that are used in the flutter analyses. The modes are computed from pre-stressed load conditions, determined by static aeroelastic analysis of load case 2 (U_∞ = 7 m/s). By analysis of the shape of the modes, it can be concluded that initial stresses due to structural nonlinearities mainly led to a change in torsional behavior. Therefore it is important to consider "nonlinear" mode shapes in dynamic aeroelastic analysis as aerodynamic loads are very sensitive to blade torsion.

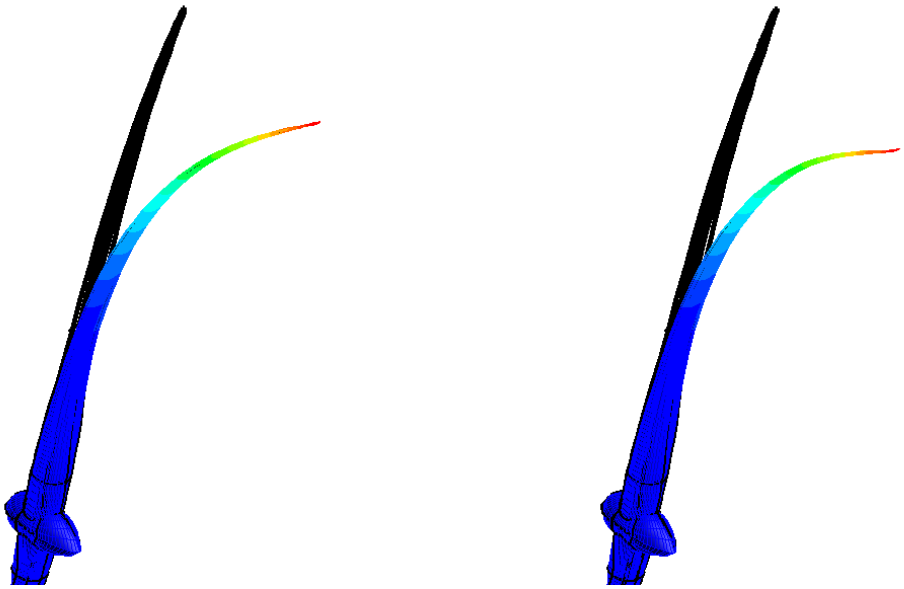

Figure E.1: First mode shape; **Left**: Φ_1^L, f = 0.510 Hz; **Right**: Φ_1^{NL}, f = 0.508 Hz

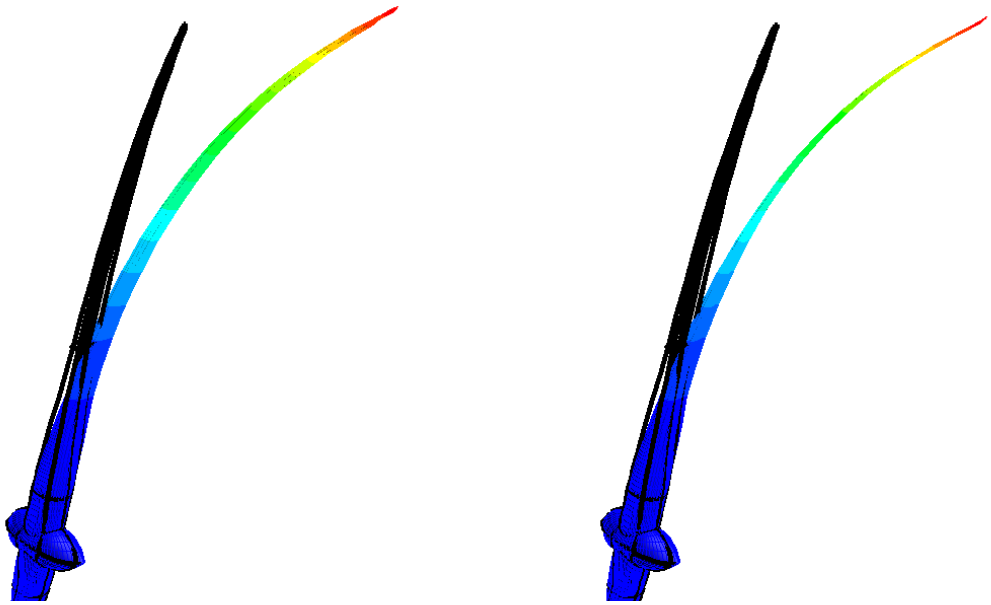

Figure E.2: Second mode shape; **Left**: Φ_2^L, f = 0.729 Hz; **Right**: Φ_2^{NL}, f = 0.718 Hz

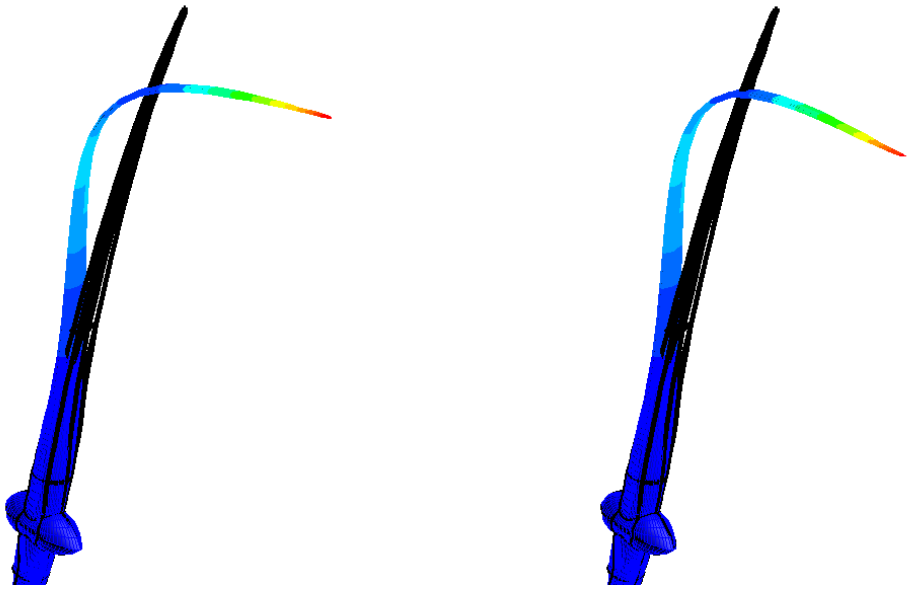

Figure E.3: Third mode shape; **Left**: Φ_3^L, f = 1.329 Hz; **Right**: Φ_3^{NL}, f = 1.307 Hz

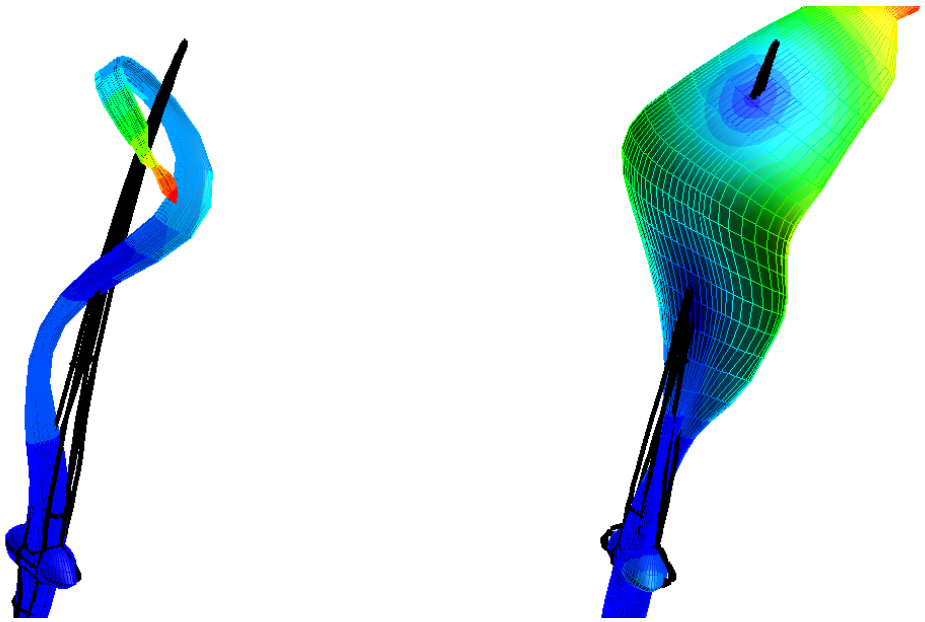

Figure E.8: Eighth mode shape; **Left**: Φ_8^L, f = 4.594 Hz; **Right**: Φ_8^{NL}, f = 4.673 Hz

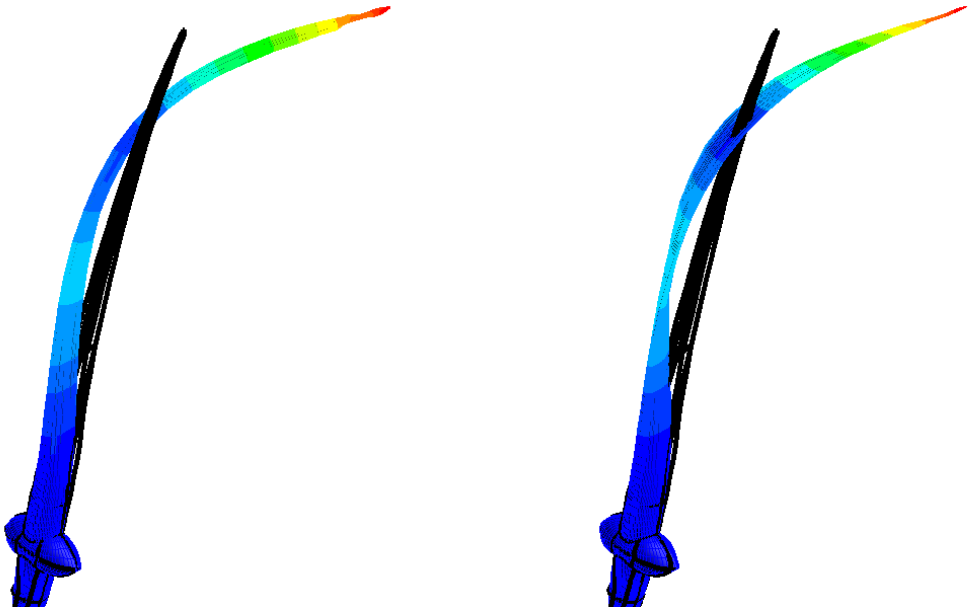

Figure E.4: fourth mode shape; **Left**: Φ_4^L, f = 2.173 Hz; **Right**: Φ_4^{NL}, f = 2.075 Hz

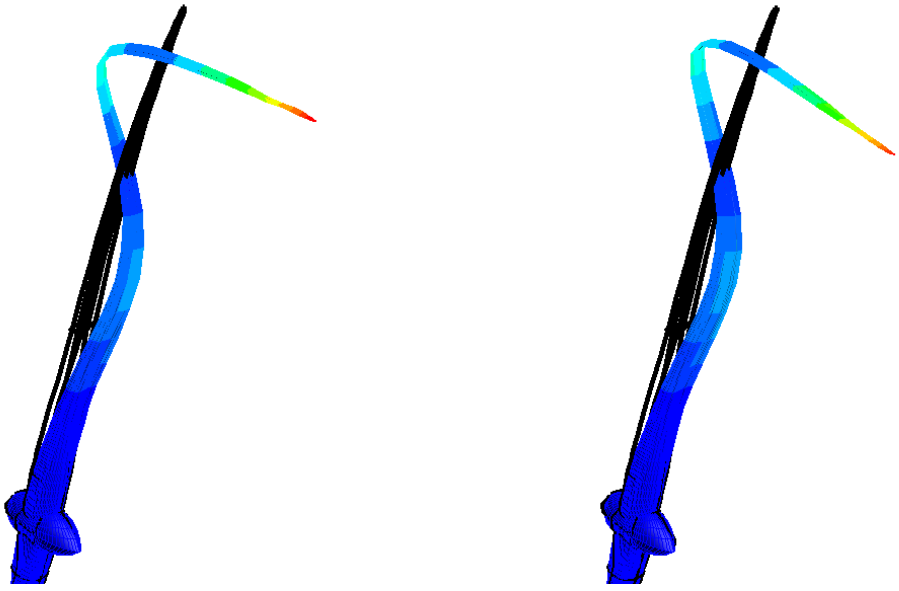

Figure E.5: Fifth mode shape; **Left**: Φ_5^L, f = 2.651 Hz; **Right**: Φ_5^{NL}, f = 2.596 Hz

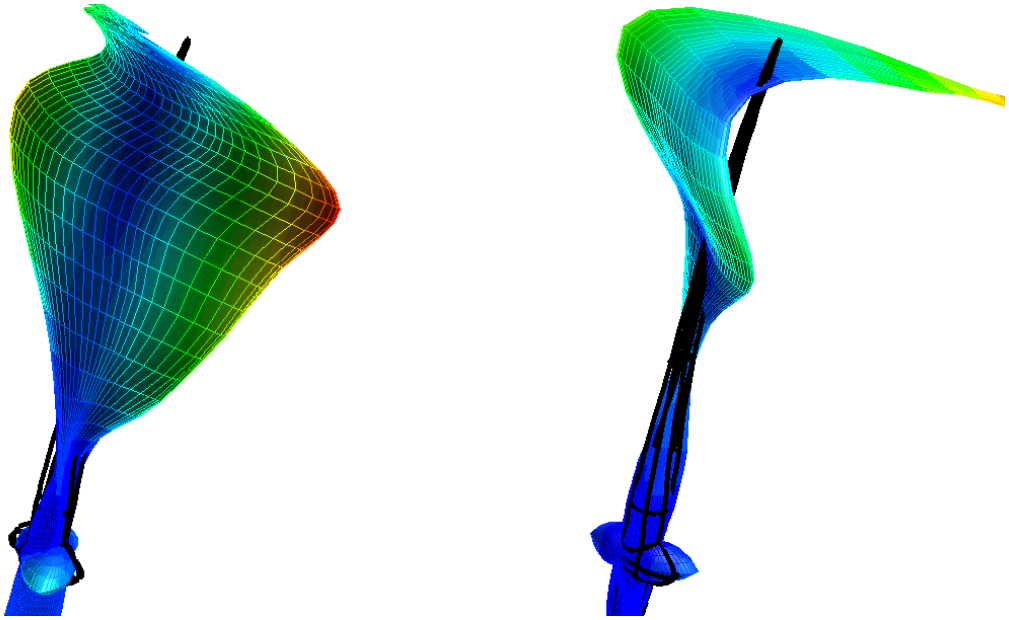

Figure E.6: Sixth mode shape; **Left**: Φ_6^L, f = 4.175 Hz; **Right**: Φ_6^{NL}, f = 4.168 Hz

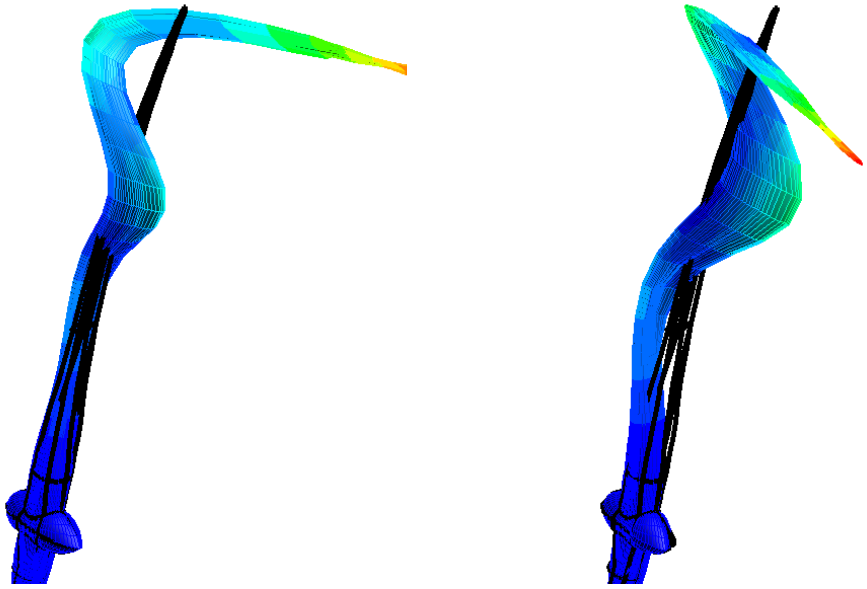

Figure E.7: Seventh mode shape; **Left**: Φ_7^L, f = 4.290 Hz; **Right**: Φ_7^{NL}, f = 4.439 Hz

F

PERIODICITY OF GAF'S

In this appendix the periodicity plots are shown. Only the diagonal generalized aerodynamic forces are considered to avoid an overload of figures. It can be observed that the high-frequency aerodynamic responses converged qualitatively as the hysteresis are closed. Low-frequency vibration barely influenced the flow, causing the transient effects to become dominant. The generalized aerodynamic forces were corrected to avoid errors in the computation of the AIC's due to convergence issues.

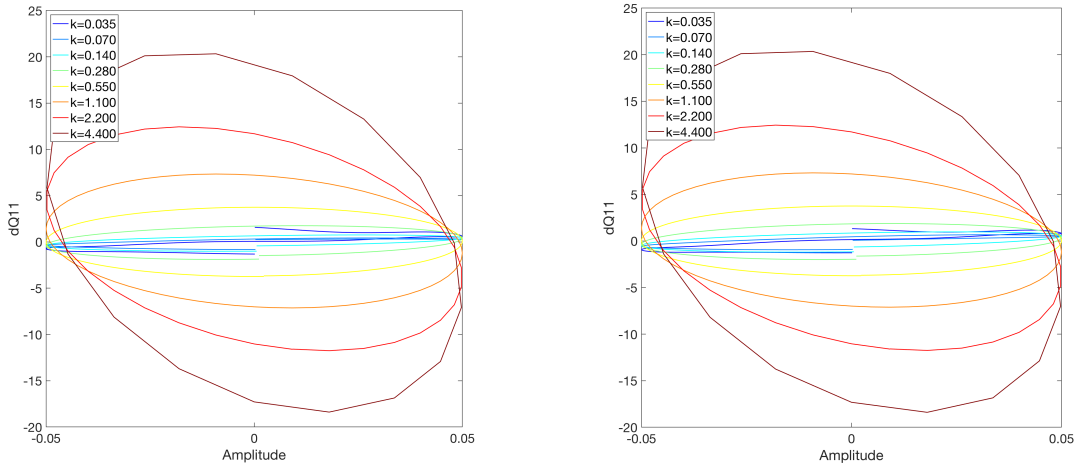

Figure F.1: The phase plots of the generalized aerodynamic forces of the first flapwise bending mode; **Left**: Around linear structure, **Right**: Around nonlinear structure.

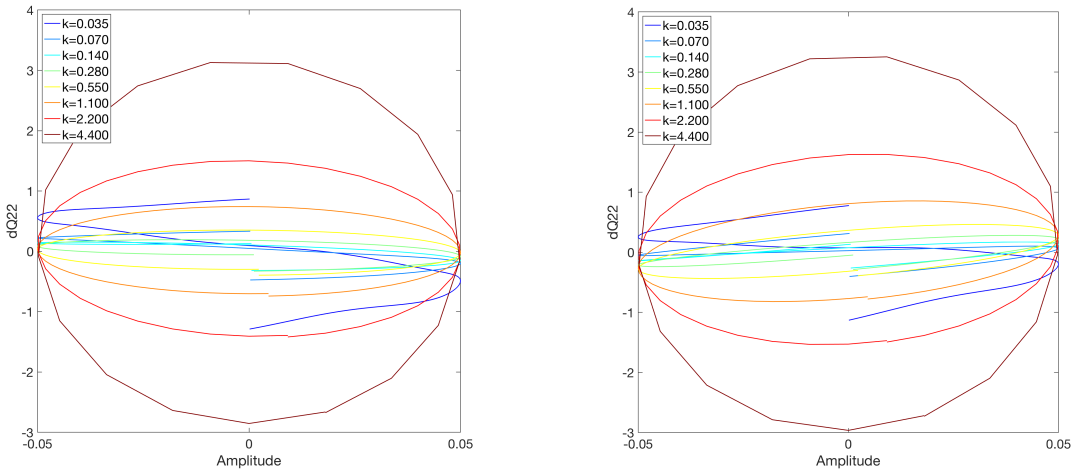

Figure F.2: The phase plots of the generalized aerodynamic forces of the first edgewise bending mode; **Left**: Around linear structure, **Right**: Around nonlinear structure.

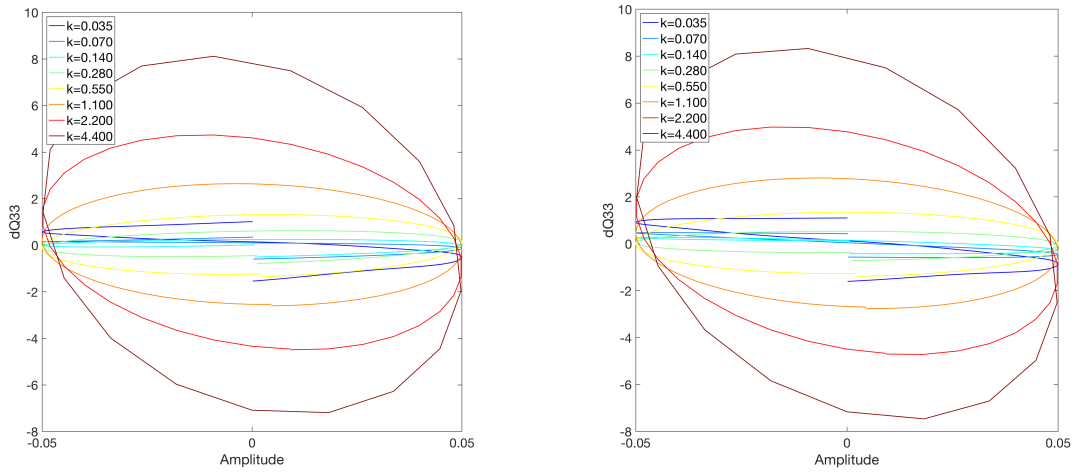

Figure F.3: The phase plots of the generalized aerodynamic forces of the second flapwise bending mode; **Left**: Around linear structure, **Right**: Around nonlinear structure.

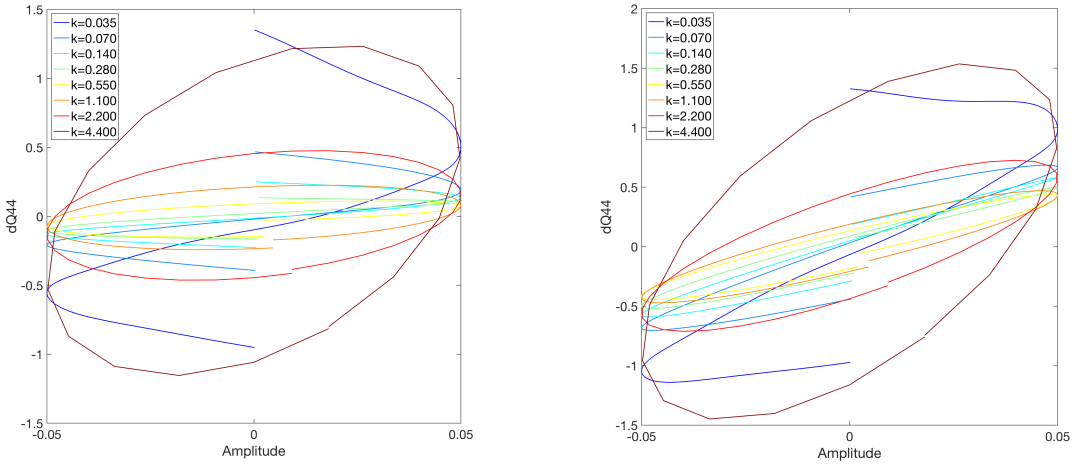

Figure F.4: The phase plots of the generalized aerodynamic forces of the second edgewise bending mode; **Left**: Around linear structure, **Right**: Around nonlinear structure.

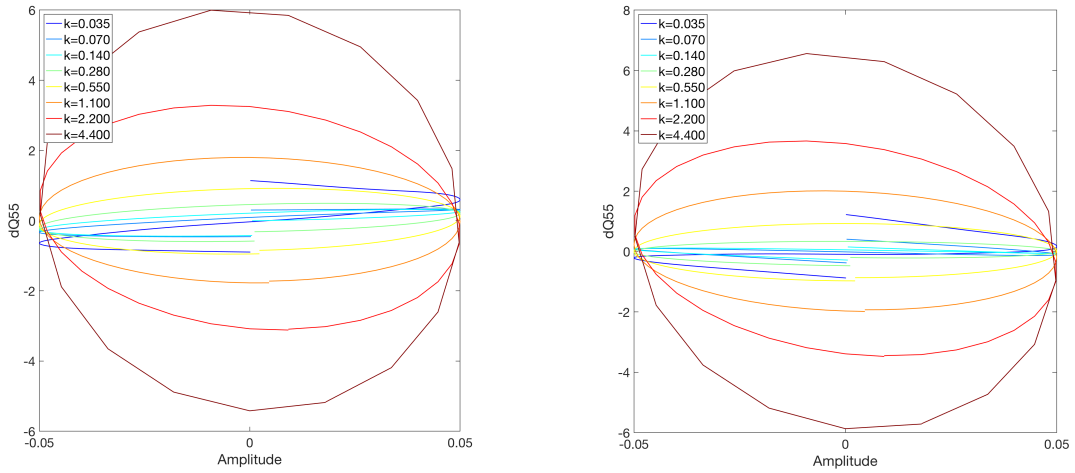

Figure F.5: The phase plots of the generalized aerodynamic forces of the first mixed bending mode; **Left**: Around linear structure, **Right**: Around nonlinear structure.

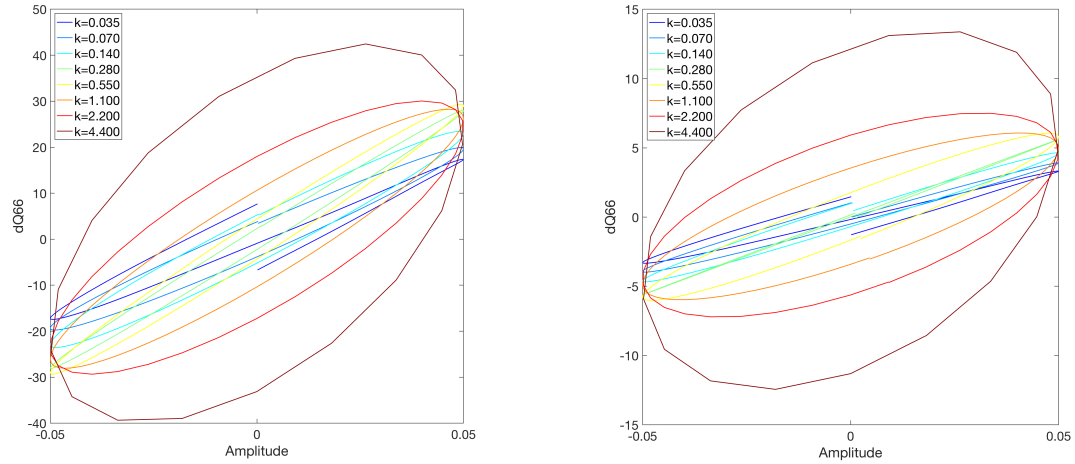

Figure F.6: The phase plots of the generalized aerodynamic forces of the first torsion mode; **Left**: Around linear structure, **Right**: Around nonlinear structure.

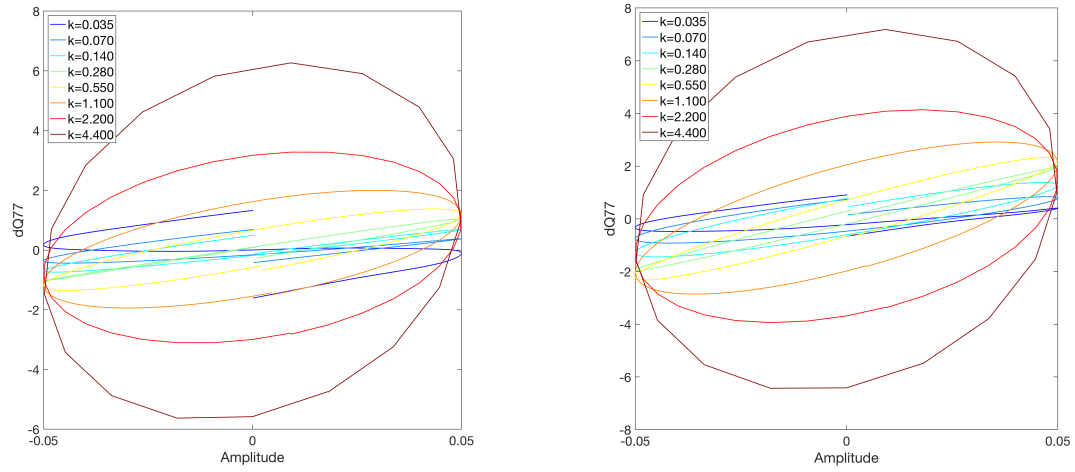

Figure F.7: The phase plots of the generalized aerodynamic forces of the second mixed bending mode; **Left**: Around linear structure, **Right**: Around nonlinear structure.

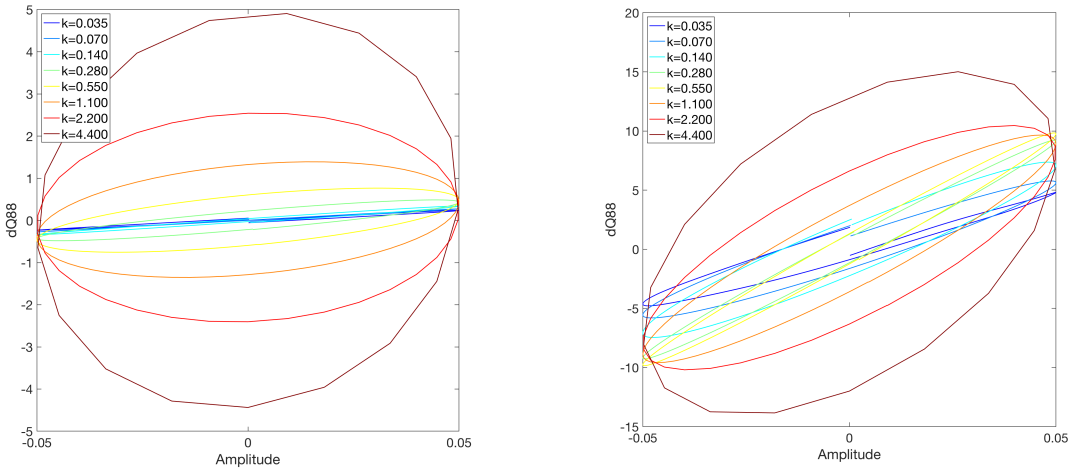

Figure F.8: The phase plots of the generalized aerodynamic forces of the third mixed bending mode; **Left**: Around linear structure, **Right**: Around nonlinear structure.

G

FREQUENCY AND DAMPING PLOTS FROM THE PERFORMED FLUTTER ANALYSES

This appendix gives an overview of the frequency and damping plots for the different conducted flutter analyses (linear/nonlinear and corrected/uncorrected). From the frequency and damping plots it can be observed that the flutter results were reasonable similar for the corrected and uncorrected AIC's. Since low-frequency motions did not significantly contribute to changing flow conditions, the results remained similar.

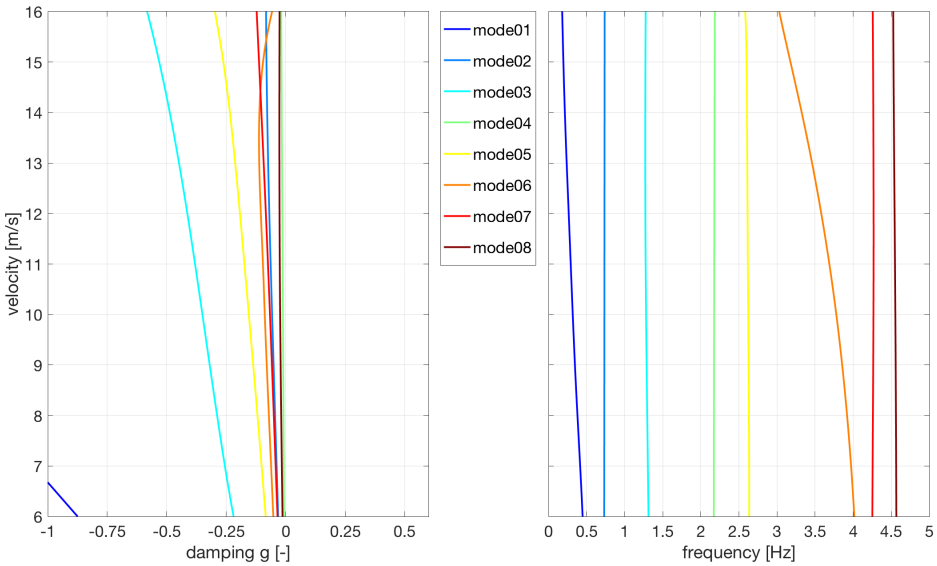

Figure G.1: Frequency and damping plot for the uncorected aerodynamic influence coefficients (linearized around linear deflected blade)

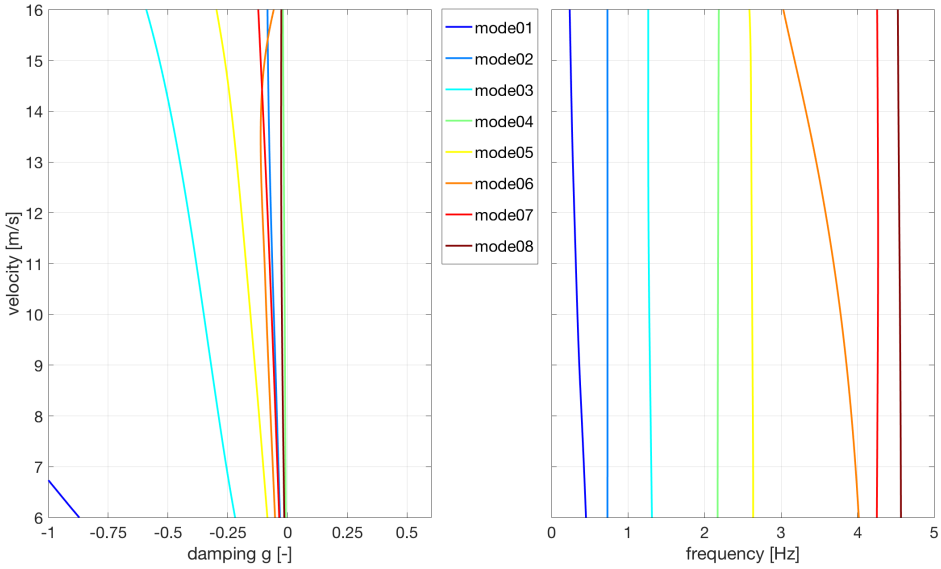

Figure G.2: Frequency and damping plot for the corrected aerodynamic influence coefficients (linearized around linear deflected blade)

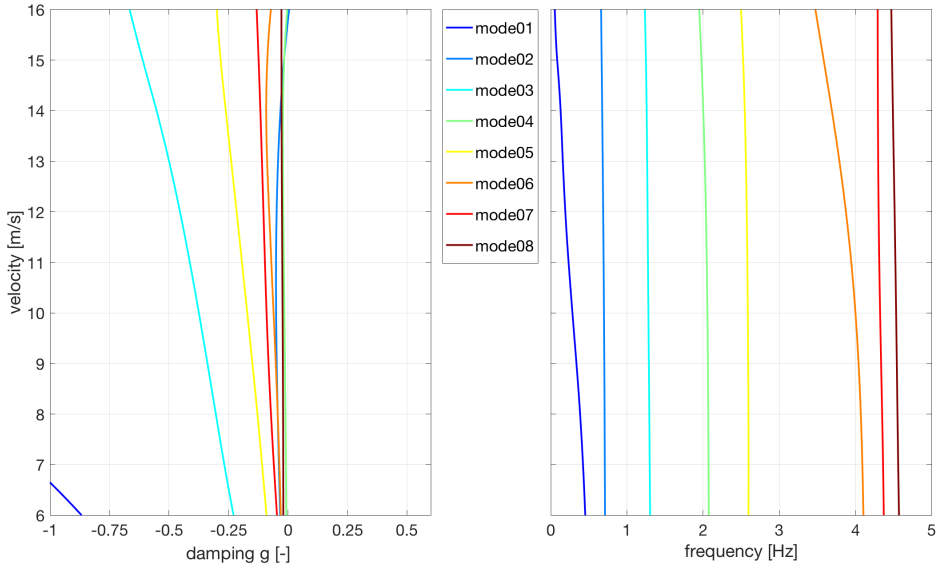

Figure G.3: Frequency and damping plot for the uncorrected aerodynamic influence coefficients (linearized around nonlinear deflected blade)

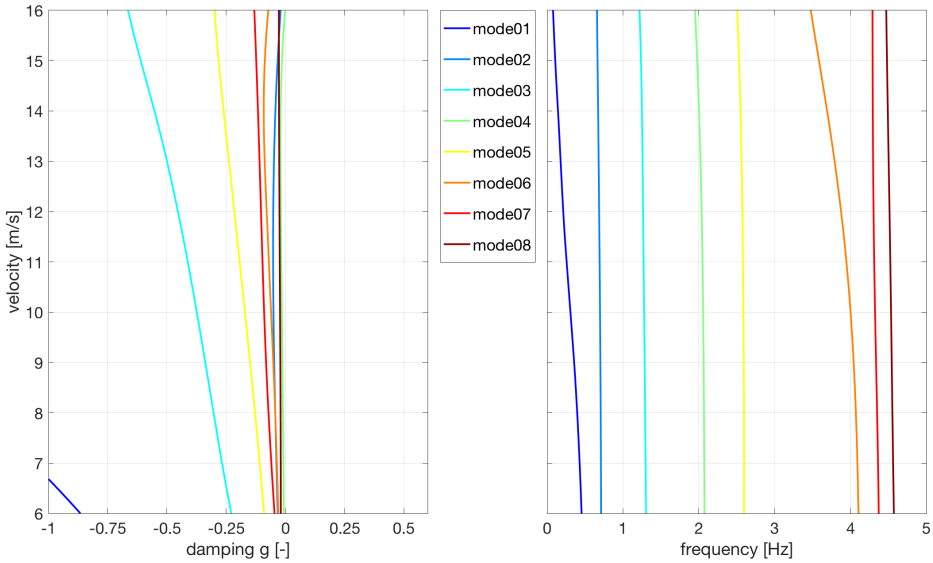

Figure G.4: Frequency and damping plot for the corrected aerodynamic influence coefficients (linearized around nonlinear deflected blade)